METALLIC COATINGS AS PERIPHERAL BARRIERS TO DIMINISH THE ADVERSE EFFECTS OF CATHODIC PROTECTION ON PRESTRESSING MEMBERS

A Dissertation

by

ARASH ROCKEY

Submitted to the Graduate and Professional School of
Texas A&M University
in partial fulfillment of the requirements for the degree of

DOCTOR OF PHILOSOPHY

Chair of Committee,	Stefan Hurlebaus
Committee Members,	Joseph Bracci
	Matthew Yarnold
	Homero Castaneda
Head of Department,	Zachary Grasley

May 2022

Major Subject: Civil Engineering

ABSTRACT

The likelihood that a prestressed system fails as a result of corrosion attacks is significantly greater than that of conventional reinforced concrete systems. Steel strands used in prestressed concrete are continuously subjected to large tensile forces despite their small cross sections, and they are also made of a higher fraction of carbon compared with mild steel to raise the strength level of the steel strands. Therefore, the American Concrete Institute limits the chloride content in prestressed systems to 0.06 % by weight of cement, yet this threshold is often exceeded in marine structures and aggressive environments. A permanent solution to avoid degradation of the steel wires in concrete is cathodic protection that reduces the rate of redox reactions and prevents the initiation of corrosion pits. But, the use of an impressed current system can cause hydrogen evolution at extreme negative potentials leading to brittle cracks in high-strength steel wires.

Herein is documented a history of the utilization of cathodic protection in reinforced and prestressed concrete. The adverse effects of the impressed current that may cause the failure of those systems are addressed. A brief review on the imperfection of the current protection systems, the mechanisms that lead to corrosion in concrete, and those that cause the brittle failures of steel wires are discussed in detail. The past failures of non-building prestressed systems are also tabulated.

In this work, it is suggested that prestressing wires are coated with metallic alloys in order to prevent diffusion of hydrogen atoms in steel embedded in concrete. Zinc-nickel has been already applied to the pipelines used to transport oil and gas to reduce risks associated with hydrogen embrittlement, and nickel-cobalt coating has been proven to protect steel from aggressive environments in aerospace applications. However, the efficacy of these coatings to protect ASTM A 416 steel wires from corrosion and brittle failures in the concrete environment has not been studied in-depth yet. To this end, ASTM A 416 steel wires were coated with zinc-nickel and nickel-cobalt alloys; then, the corrosion properties of plated wires were identified

with the performance of cyclic potentiodynamic polarization and electrochemical impedance spectroscopy. A galvanostatic chloride acceleration test was also performed to determine the efficacy of impressed current to protect steel wires in an aggressive environment. All coated specimens were exposed to atomic hydrogen during the embrittlement test to assess the durability of coatings in response to hydrogen diffusion. Finally, the wear resistance of the coated films was examined, and the results were subsequently reported.

Based on the findings from the experimental evaluations, it was concluded that the corrosion properties of nickel-cobalt alloy plated on steel were similar to the kinetic behavior of the zinc-phosphate layer, the current coating system. However, the nickel-cobalt film limited the diffusion of atomic hydrogen in the metal substrate. Zinc-nickel also acted as a hydrogen barrier, yet the electrodeposition of the alloy on high-strength steel wires is not recommended since the corrosion rate of the alloy was found relatively high in alkaline environments. That said, a multilayer coat of nickel prior to applying the current coating system on steel wires is also suggested as an alternative approach to nickel-cobalt coating. It was found that the wear rate of all the coatings studied in this work were higher when they were examined in the abrasive test with a metallic bar instead of a plastic sheet, while the nickel-cobalt coating showed a slightly greater wear resistance.

DEDICATION

To my loving parents and charming sister.

ACKNOWLEDGEMENTS

I would like to express my appreciation for my advisor, Dr. Stefan Hurlebaus, for mentoring me during my Ph.D. and for his support and encouragement to pursue the outcome of this research study. He gave me freedom to follow my own research interests; meanwhile, his patience and insightful hints aided me to overcome the obstacles I confronted. I would also like to thank my committee members Dr. Joseph Bracci, Dr. Matthew Yarnold, and Dr. Homero Castaneda for their advice and thoughtful comments to improve the results of this work.

I am also grateful to Dr. Robin Autenrieth and Dr. Zachary Grasley for their support and the opportunity that they provided for me to develop my academic skills during my studies at Zachry Department of Civil and Environmental Engineering.

In addition, I would like to thank my friends, Isabel Mlo and Mikhail Lanier, for the time and effort they made to revise and proofread this work.

Finally, I want to extend my gratitude to my friend, Ryan Hanslmaier, who encouraged me to follow my career as a researcher at Texas A&M University and to my family who believed in me and assisted me in various ways.

ACRONYMS AND NOMENCLATURE

LIST OF ABBREVIATIONS

ACI	American Concrete Institute
ASR	Alkali–Silica Reaction
ASTM	American Society for Testing and Materials
BCC	Body-Centered Cubic, Crystal Structure
CE	Counter Electrode
CFC	Corrosion Fatigue Cracking
CPP	Cyclic Potentiodynamic Polarization
CSV	Comma-separated values
DIBt	Deutsches Institut für Bautechnik
EIS	Electrochemical Impedance Spectroscopy
FCC	Face-Centered Cubic, Crystal Structure
FFT	Fast Fourier Transform
FIP	International Federation for Structural Concrete
GCA	Galvanostatic Chloride Acceleration
GPIB	General Purpose Interface Bus
H_v	Vickers Hardness Number

HCP	Hexagonal Close-Packed, Crystal Structure
HE	Hydrogen Embrittlement
HER	Hydrogen Evolution Reaction
ICCP	Impressed Current Cathodic Protection
IEEE-488	Standard Digital Interface for Programmable Instrumentation
PDV	Portable Digital Vibrometer
pH	Reciprocal Logarithm of the Hydrogen Ion Activity
ppm	Parts per million
RE	Reference Electrode
RPM	Revolutions per minute
SCC	Stress Corrosion Cracking
SCE	Saturated Calomel Electrode
SEM	Scanning Electron Microscopy
SLDI	Scanning Laser Doppler Interferometry
temp.	Temperature
UHPC	Ultra-High Performance Concrete
WE	Working Electrode

LIST OF MATHEMATICAL PARAMETERS

δ	Slip	mm
$\dot{x}$	Wave Velocity	m/s
$\hat{I}$	Intensity	cd
λ	Wavelength	nm
ω	Angular Frequency	rad/s
ϕ	Time Phase Shift	degrees
σ	Applied Stress	N/m^2
τ_b	Bond Stress	MPa
C_{dl}	Double Layer Capacitance	μF
f	Frequency	Hz
h	Wear Displacement	m
i, log i	Current Density	A/cm^2
$i(t)$	Alternating Current	A, mA, μA
i_{corr}	Corrosion Current Density	$\mu A/cm^2$
k	Wear Rate Coefficient	mm^3/Nm
Q	Admittance	s/Ω
r	Optical Path	m
R_p	Polarization Resistance	kΩ

R_s	Solution Resistance	Ω
R_Ω	Ohmic Resistance	kΩ
S	Sliding Distance	m
T	Period	s
t, τ	Time	s
t_i	Time to Failure	s
$v(t)$	Alternating Voltage	V, mV, μV
V_{corr}	Corrosion Potential	V vs. SCE
x	Wave Displacement	m
z, $\hat{z}$	Impedance	Ω
Z_o	Impedance in Constant Phase Element	Ω
CR	Corrosion Rate	mm/y
EI	Embrittlement Index	
n	Constant Phase Element Parameter	

LIST OF CHEMICAL COMPOUNDS

C-S-H	Calcium Silicate Hydrate
$Ca(OH)_2$	Calcium Hydroxide
$CaCO_3$	Calcium Carbonate
$CaSO_2.2H_2O$	Calcium Sulfate (Gypsum)
Cl	Chloride
$Co(OH)_2$	Cobalt(II) Hydroxide
$Co(OH)_3$	Cobalt(III) Hydroxide
$CoCL_2.6H_2O$	Cobalt(II) Chloride Hexahydrate
Co	Cobalt
Co^{2+}	Cobalt Cation
Co^{3+}	Cobaltic Cation
Co_3O_4	Cobalt Oxide
$Fe(OH)_2$	Ferrous Hydroxide
$Fe(OH)_3$	Ferric Hydroxide
$FeCl_2$	Iron (II) Chloride (Ferrous Chloride)
FeO_4	Ferrate (VI)
Fe	Iron
Fe^{2+}	Ferrous Cation

Fe^{3+}	Ferric Cation
Fe_2O_3	Ferric Oxide
$Fe_2O_3.H_2O$	Hydrated Ferric Oxide
Fe_3C	Iron Carbide (Cementite)
Fe_3O_4	Ferrous Ferric Oxide
HCL	Hydrochloric Acid
$HCoO^{2-}$	Cobalt Hydroxide Oxide
$HFeO_2$	Iron(III) Oxide-Hydroxide (Ferric Oxyhydroxide)
$HNiO^{2-}$	Hydroxy(oxo)nickel
H_2CO_3	Carbonic Acid
H_2O	Water
H_3BO_3	Boric Acid
KCl	Potassium Chloride
KOH	Potassium Hydroxide
KSCN	Potassium Thiocyanate
K_2SO_4	Potassium Sulfate
NaCl	Sodium Chloride
NaCN	Sodium Cyanide
NaOH	Sodium Hydroxide
NH_4SCN	Ammonium Thiocyanate

$Ni(OH)_2$	Nickel(II) Hydroxide
Ni/Co	Nickel–Cobalt
$NiCL_2.6H_2O$	Nickel(II) Chloride
NiO_2	Nickel Dioxide
$NiSo_4.7H_2O$	Nickel(II) Sulfate Heptahydrate
Ni	Nickel
Ni^{2+}	Nickel Cation
Ni_2O_3	Nickel(III) Oxide
Ni_3O_4	Nickel(II) Oxide
OH	Hydroxide
O_2	Oxygen
Ph	Phosphate
$Zn(OH)_2$	Zinc Hydroxide
Zn/Ni	Zinc–Nickel
Zn/Ph	Zinc–Phosphate
ZnO^{2-}	Zinc Oxide
ZnO_2	Zinc Peroxide
$ZnSo_4.7H_2O$	Zinc Sulfate Heptahydrate
Zn	Zinc
Zn^{2+}	Zinc Cation

TABLE OF CONTENTS

Page

LIST OF FIGURES

FIGURE Page

LIST OF TABLES

TABLE Page

1. INTRODUCTION

1.1 Problem Statement

Concrete, by its nature, is brittle and exhibits relatively small plastic deformation; hence, it has to be reinforced by carbon steel to compensate for its low tensile strength and ductility. However, in the case of non-building structures—such as long-span bridges, parking garages, quay walls, and pressure vessels—that are designed to withstand heavy loads and routine vibrations, flexural cracks still develop at locations where the tensile stress is relatively high. In order to enhance the shear and torsional capacity of those systems and reduce the tensile stress in critical sections, members can be longitudinally confined from the pressure exerted by tensioning reinforcement steel (prestressing). Reinforcement in prestressed concrete has to not only balance the internal force resulting from the initial tensile stress under the concrete's self-weight, but also resist additional stresses due to concrete creep and shrinkage, steel relaxation, friction, live loading, etc. (Nawy, 1996). Today, this is achieved with bundled strands of seven stress-relieved cold-drawn steel wires conforming to ASTM A 416 (ACI cmte. 222, 2014).

Since high-strength steel strands significantly contribute to sustaining heavy loads in long spans, and the stability of prestressed concrete structures directly relies on the durability of these elements, it is essential to protect these members from corrosive environments. Note that risks associated with the failure of prestressing members due to corrosion is generally more than conventional reinforced concrete because a low-relaxation strand is generally made of a relatively small size (ACI cmte. 222, 2014). In addition, a high-strength steel wire is under constant tension within an average of 60% of its ultimate tensile strength over the course of its service life (Treadaway, 1971). If material loss or injurious defects of the section occurs for any reason (like corrosion pits), the extreme tensile stress will cause reduction in size that results in increasing the overall net stress. The material loss finally leads to a brittle

failure of wires when the corrosive agents come in contact with the metal at these regions. Beyond that, the percentage of carbon content in cold-drawn steel wire is larger compared to conventional reinforcement that leads to growing pearlite layers in high strength-steel strands. These layers are strong inhibitors for hydrogen atoms produced during the metallurgical work and later during electrochemical reactions prevalent in corrosive environments. Diffusion of hydrogen atoms in spaces between ferrite and cementite will embrittle the wire over time causing the formation of brittle cracks such as stress corrosion cracking and hydrogen embrittlement in ASTM A 416 steel wires.

Corrosion in concrete mainly arises from chloride ions which come into contact with the concrete from a variety of sources. For example, the volume of salt used on roads for deicing in the United States is about 10 million tons per year. As a low-priced agent, deicing salt enables the ice and snow to melt quickly, but sodium chloride dissolved in water produces a solution that contains a significant quantity of alkalis and chloride ions. The chloride laden water carries aggressive ions through voids and microcracks in the concrete. The chloride transportation creates a corrosive environment if the offensive ions and other diffusion mechanisms come near steel reinforcement. Several reasons can be given for the chloride penetration in concrete. If the water to cementitious materials ratio is greater than 0.42, then it should be expected that the growth of capillary pores in cement gel results in a relatively high permeability in concrete (Mindess et al., 2003). Poor grouting in post-tensioned concrete and stay cables causes voids in cement gel (ACI cmte. 222, 2014). These voids store pollutants that eventually result in pitting corrosion of low-relaxation steel wire. Even if the permeability rate of concrete is relatively low, existing microvoids still provide a mechanism for contaminated solutions to cause corrosion. For example, the accumulation of the chloride laden water close to prestressing members can be a result of water leakage because of duct defects due to maintenance and construction, drainage problems and water blockage, drifting and spalling because of flooding or collision, gaps and expansion joints, or thin concrete cover.

Other common cases of chloride induced corrosion include reinforcement steel in marine

structures, such as flood barriers or bridge piers, which is endlessly drenched by seawater and subjected the many cycles of wetting and drying. Prestressed wires embedded in saline soil to support dams and tunnels are also exposed to chloride ions.

Application of impressed current cathodic protection (ICCP) to prevent corrosion of carbon steel has been approved in reinforced concrete (Pedeferri, 1996). Conversely, its successful utilization to protect prestressed concrete from deterioration has to be treated with caution due to the risks associated with the initiation of corrosion cracking in metals. If pitting corrosion occurs on strands, net stress will increase promptly beyond the pit section, and the metal will consequently crack with little signs of warning. However, an additional cause of failure stems from overprotection where high-strength steel strands are embrittled as a result of the hydrogen evolution reaction (HER) at a certain extent of potential. Additionally, a uniform distribution of a desirable electric potential is difficult to achieve in cathodic protection. For instance, either polyethylene plastic or galvanized corrugated ducts are used to encase tendons in post-tensioning systems. The plastic duct is not electrically conductive and may limit the current required to protect the steel. In contrast, the metallic duct gains current and shields tendons from receiving the designed current (ACI cmte. 222, 2014).

Metallic coatings of high-strength steel wires reduce the destructive effect of hydrogen embrittlement in prestressed concrete; therefore, it provides an additional assistant to ICCP that protects prestressing members without causing any deterioration in metal where the potential of steel drops less than -900 mV vs. SCE. This is a potential at which the high-strength steel is neither attacked by pitting corrosion, nor stress corrosion cracking, nor embrittled by hydrogen. A coating layer works as a supplement to ICCP so that prestressing members are always protected from corrosion attack. Bhadeshia (2016) suggested metallic coatings as a solution to prevent hydrogen embrittlement in steel. According to the author, the transition of hydrogen atoms between plated layers occurs at a much lower rate compared to the underlying substance. In addition, coated layers protect steel substrate by reducing the rate of subsurface crack initiation and mitigate surface damages by decreasing the destructive

effects of contaminants (Bhadeshia, 2016).

Coated layers of cadmium, zinc-nickel alloy, or nickel-cobalt alloy are highly efficient at limiting the transition of hydrogen atoms in substrate (Bhadeshia, 2016; Hillier & Robinson, 2004; Matzdorf et al., 2017; Rashmi et al., 2017; Golodnitsky et al., 2002; Wykpis et al., 2011; Durairajan et al., 2000; Rosas et al., 2018). It was common in the past to use cadmium as a sacrificial coating on metals to protect the substrate from a severe corrosive environment. Bird and Strauss (1967) successfully used cadmium-plated steel to lessen the corrosion rate in reinforced concrete (Moore et al., 1970). However, the application of cadmium coating has been plummeting for more than two decades because it is carcinogenic. In addition, cadmium coating to steel strands reduces the friction and wear between the reinforcement and cementitious materials; hence, the coating system should be avoided in prestressing structures.

Zinc, akin to cadmium, grows whiskers which results in a strong bond to a substrate but does little to prevent the penetration of hydrogen atoms. On the contrary, zinc alloyed with nickel makes a great diffusion barrier. Nickel works as a hydrogen-absorbing interlayer since it deposits in steel prior to zinc in the process of the electroplating. Then, the plated layer imprisons the agitated atoms in its powerful hydrogen-traps and almost blocks hydrogen absorption in steel (Bhadeshia, 2016). Note that the electroplating process of zinc-nickel alloy may initiate hydrogen evolution in plated metal. Therefore, heat treatment in the range of 190°C to 230°C for 8-24 hours is required to provide atmospheric escape of hydrogen atoms immediately after plating (Dini, 1993; Bhadeshia, 2016). As an alternative, hydrogen is not produced during the deposition of nickel-cobalt alloy that reduces the amount of hydrogen atoms encapsulated between coating layers. The alloy is not a sacrificial coating similar to cadmium or zinc, yet it exhibits corrosion resistance superior to the two other metals. Nickel-cobalt alloy as a barrier to protect the substrate from brittle failures is already employed in the aerospace and subsea industries (Rosas et al., 2018).

1.2 Significance

ICCP is a well-founded approach to reduce the corrosion rate in reinforced concrete, but its application to prestressing steel increases the risk of brittle fracture for low-relaxation strands. This study intends to find a solution so that ICCP safely protects prestressing steel wires from corrosive environments. Therefore, two metallic coatings of zinc-nickel and nickel-cobalt alloys are proposed to decrease the permeation of atomic hydrogen produced during cathodic protection of the substrate. The coatings have successfully protected steel sections used in aerospace and oil and gas industries from hydrogen embrittlement, but their application to ASTM A 416 steel used in prestressed concrete has not yet been validated.

The significance of this research is to reduce the repair and maintenance cost as well as extend the service life of civil structures. Today, the most common corrosion protection techniques for prestressing members are concrete cover and grouted ducts. However, the existence of cracks and voids in these systems leads to pitting corrosion in high-strength steel and may end with a costly structural failure. The presence of salt in onshore concrete structures is also inevitable because a mixture of ocean water and groundwater eventually diffuses through concrete pores in some concrete mixes. Furthermore, since freshwater and river sand resources are being consumed at such a quickening pace, it seems that the use of salt water in concrete is inevitable in the near future. Therefore, arriving at a solution to build concrete structures invulnerable to the attack on a corrosive environment is necessary. While cathodic protection appears to be the most viable solution of protecting reinforcement in an aggressive environment resulting from chloride ions, it is critical that its application does not also cause brittle failure of high-strength steel strands.

1.3 Organization of the Dissertation

This research study aims to improve corrosion resistance of prestressed systems and proposes solutions to reduce the brittle failure of high-strength steel strands. In attaining the goal of this study, the current dissertation represents the following nine chapters:

- Chapter 1 describes the problem statement and provides possible solutions in addition to the motivation and significance of the research.
- Chapter 2 reviews the relevant technical literature and gives a brief description of mechanisms resulting in degradation of high-strength ASTM A 416 steel. A brief review of the risks associated with the current corrosion protection techniques in concrete is also reported in this chapter.
- Chapter 3 discusses the process of steel wire fabrication and the steps required for electroplating of high-carbon, low-alloy steel.
- Chapter 4 and Chapter 5 represent techniques performed in the laboratory to evaluate the severity of localized corrosion on ASTM A 416 wires with and without coatings.
- Chapter 6 presents an examination of ASTM A 416 wires with different coating systems to investigate the corrosion properties of the metal and impressed current efficacy to protect the steel wires against corrosive environment.
- Chapter 7 represents a study to determine the resistance of as-received specimens and plated wires with zinc-nickel and nickel-cobalt alloys to hydrogen embrittlement.
- Chapter 8 discusses adhesion and durability of coating systems in galvanized and plastic ducts. An analysis is also reported to assess wear resistance of plated layers.
- Chapter 9 identifies benefits and risks of proposed metallic coatings to prestressing members. It provides a summary, conclusions, and a list of recommendations to reduce the risks of brittle failure in steel wires.
- Appendix A documents the prestressed systems that have failed in the past as a result of corrosion. A review of the bond mechanisms in prestressed systems is given in the Appendix. Python scripts developed for the purpose of this study are also given at the end.

2. BACKGROUND AND LITERATURE REVIEW

2.1 Prestressed Systems

It was common in the early 20th Century that prestressed concrete was only used to build storage tanks and pressure pipes. However, despite a great number of prestressed viaducts built in Europe after World War II (Nawy, 1996), the first U.S. prestressed bridge was officially completed in Tennessee as late as 1950. ACI Committee 222 (2014) reported this bridge in addition to the Walnut Lane Bridge in Pennsylvania that was accessible to the general public a few months later in 1951.

Nawy (1996) reviewed more than 100 years of development of prestressed systems in engineering structures (Figure 2.1). According to the author, a Californian engineer, P.H. Jackson was the pioneer of utilizing prestressing elements in beams and arches in 1872. Later, a German engineer, C.W. Doehring, introduced the prestressing concept for concrete slabs in 1888. However, this novel method was rarely implemented in structures because the applied initial stress was reduced overtime. Several attempts had been made by European and American engineers to improve the prestressing system, yet their models did not solve the problem related to the loss in prestress until R.E. Dill developed the idea of using an unbonded post-tensioning system to overcome the stress loss due to concrete creep and shrinkage (Nawy, 1996). Ultimately, among the pioneers, a French engineer, Eugene Freyssinet, drew engineers' attention to an advanced linear prestressing system in 1928 (Nawy, 1996). The Freyssinet's model consisted of a set number of high-strength steel wires that were properly restricted in a cylindrical anchor at the beam-end. When the steel wires were fixed on their positions, a jack pulled the cables out until they were taut and an adequate level of prestressing was achieved.

Post-tensioned concrete is a common choice in the bridge industry because it raises the general capacity of the system and makes it possible to build long span girders (Hurlebaus et

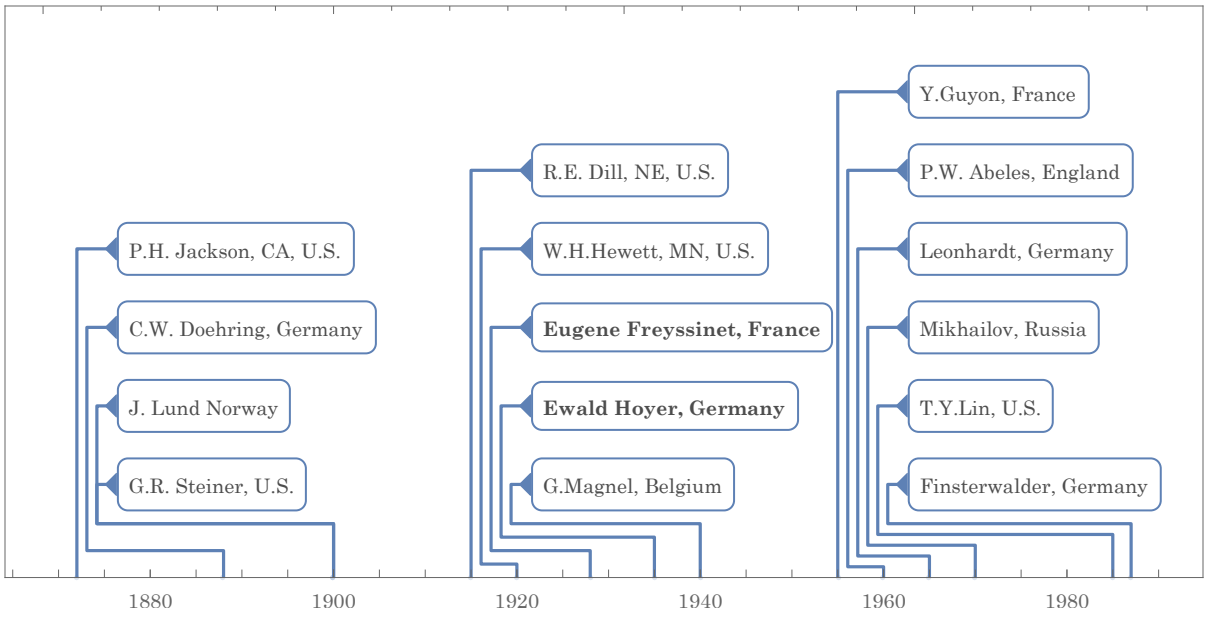

Figure 2.1: Historical development of prestressed systems, adapted from (Nawy, 1996).

al., 2016). In addition, post-tensioning systems substantially minimize the construction cost of sub- and superstructures by reducing the transportation cost (Castrodale & White, 2004). In contrast, instability of the high-quality steel strands due to a corrosive environment should be considered as a potential drawback of a post-tensioning system. Cables embedded in ducts are not coated by concrete, so they are more susceptible to corrosion in an aggressive environment, such as coastal regions. Therefore, high-quality cement grout is recommended to use in U.S. post-tensioned bridges to protect steel wires from corrosive agents. However, no voids should form in grouted ducts because moisture, salt-laden water, and other types of contaminants can readily penetrate through porous sections, which eventually cause deterioration of steel strands. Micro-flaws in the concrete are also expected to form as a result of the negative effects associated with time-dependent losses, anchorage seating loss, and relaxation loss that occur during the structure's service life.

In 1935, German engineer, Ewald Hoyer, designed a low weight concrete whose steel strands were prestressed before casting (Briere et al., 2013). Cables in pretensioned systems are not protected by cement grout, but they are directly in contact with the concrete. If no cracks appear on the concrete surface, or if the permeability of the concrete is low enough, then

it can be expected that the corrosion rate of the steel strands is low in alkaline environments. However, it is difficult to guarantee the condition that the pH level near the reinforcement remains consistently high because cracks formed by service load, time dependent strains, steel relaxation loss, etc. increase the probability of corrosive solution coming into contact with prestressing strands.

Concrete cover is a primary barrier to protect steel strands from corrosion in prestressed concrete. Hence, as discussed above, the quality of concrete has to be at the level that moisture is not present near the reinforcement. Therefore, Ultra-High Performance Concrete (UHPC) is an option for use in prestressed structures; if not, the water to cementitious materials ratio has to be kept low during mixing concrete. Ryan et al. (2012) listed paint and water repellent sealers as two classes of surface coatings that reduce permeability of the concrete. Among these protection techniques, the application of epoxy paint and urethanes have received the most attention in the U.S., yet sealers such as methyl methacrylate, silane, and silicone are also applied in sub- and superstructures of U.S. bridges. The secondary barrier used in post-tensioning systems is a combination of cement grout and a plastic or galvanized duct, although studying the efficiency of plastic or galvanized ducts is beyond the scope of this study. An epoxy coating of steel strands also shows a relatively good corrosion resistance in addition to the above mentioned barriers, but the bond reduction between the epoxy coated steel and concrete has to be taken into consideration. ACI 222.2R-01 recommends the epoxy coating of strands for unbonded post tensioning systems, although the use of a grit-impregnated coating in bonded prestressed concrete is not excluded. Ryan et al. (2012) cautioned against using epoxy coatings in cable-stayed systems that may be exposed to elevated ambient temperature, which have a tendency to melt the epoxy coating and cause loss of surface cohesion.

Another widely prestressed structure used in bridge industries is cable-stayed systems. Just as with prestressed concrete, failure of cables holding a concrete deck causes the catastrophic collapse of the whole system. Corrosion protection for cable-stayed bridges employ much

of the same techniques which are available for post-tensioned and pretensioned concrete. Ryan et al. (2012) reported a number of systems that are applicable for cable-stayed and suspension bridges. The most common practice is the use of a neoprene elastomeric cable wrap system. However, Ryan et al. (2012) reported that elastomeric cable wraps sometimes moisturize cables and intensify the corrosion process. Another option is an epoxy coating of cables embedded in cement-grout-filled tubes, but corrosion can still threaten epoxy-coated strands at wedge locations. The modern corrosion protection for this type of viaduct involves forced-air dehumidification that is capable of keeping the metal components continually dry. The effectiveness of this technique is questionable if the relative humidity of the tubes is not sufficiently low. Ryan et al. (2012) noted at least two bridges, the Kobe Bridge in Japan and the Ben Franklin Bridge in Pennsylvania, in which a forced-air dehumidification system has successfully been utilized.

2.2 Case Studies

Concrete bridges are generally expected to exhibit better corrosion resistance than steel viaducts because the alkaline conditions of cementitious material hold carbon steel in its passive state. This is not the case when corroding agents, such as chloride, sulfide, sulfate, or carbon dioxide come into contact with steel strands, since offensive ions break the passive layer and reduce the ambient pH that cause initiation of corrosion on wires. If corrosion related problems do not directly cause the failure of a system, studying the previous collapses of non-building structures shows that even minor corrosion formation is dangerously additive with other destructive risks, such as hydraulic loads, collisions, overload, design errors, settlement, and environmental factors (like earthquake, storm, etc.). Figure 2.2 shows the previous failures of non-building structures in North America, Europe, and the rest of the world. Further examples of the prestressed systems that were failed as a result of corrosion in concrete have been addressed in Appendix A, Table A.1. Herein represents the following examples of corrosion-related safety concerns forcing prestressed systems to close to the public.

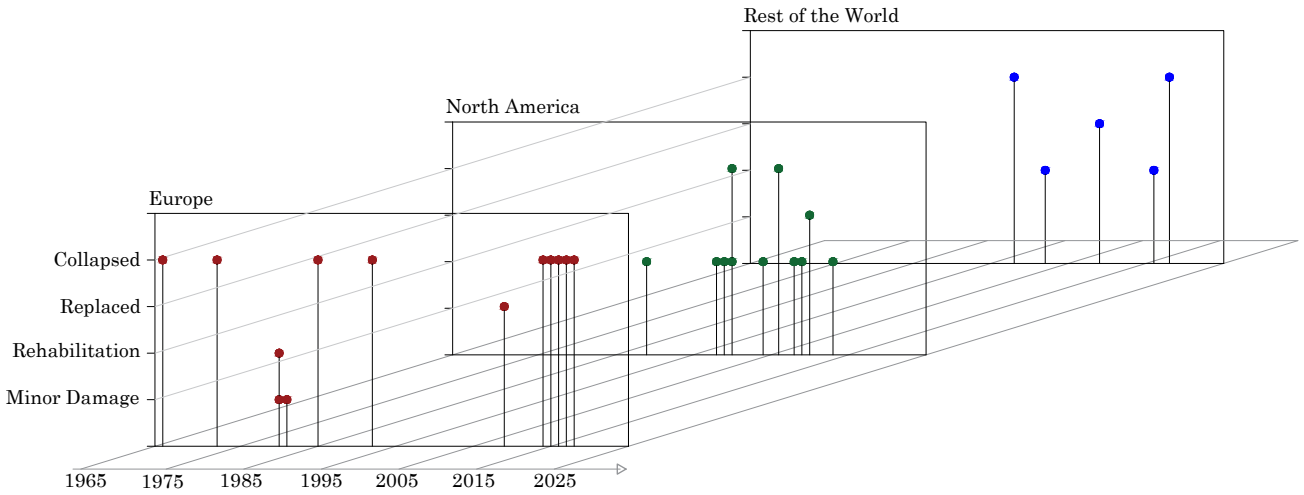

Figure 2.2: Previous failures of non-building prestressed structures, see Appendix A for detail.

2.2.1 Polcevera Viaduct, Italy

Genoa, Italy, experienced a deadly tragedy in August 2018 when a well-known cable-stayed bridge over the Polcevera River collapsed after 51 years in service (Figure 2.3). Substructures, including piers and pylons, were constructed of prestressed concrete, while steel cables linked a prestressed concrete deck to the main towers and stabilized the whole system. According to Bazzucchi et al. (2018), the design miscalculations were most likely the reason that the bridge collapsed. However, the authors addressed a series of attempted rehabilitation techniques in 1993 due to the detection of severely corroded steel strands in tower 11. It was concluded that injurious defects in metals had resulted from the presence of voids and cavities in the concrete deck. Meanwhile, similar deterioration of steel components was observed in tower 9, the site of the collapse in 2018. In addition, Bazzucchi et al. (2018) noted that the prestressed tendons and stay cables were scheduled to be replaced before the catastrophic event occurred.

2.2.2 Lake View Drive Bridge, Pennsylvania

The shoulder of a 55-year-old post-tensioned box-beam on the Lake View Drive Bridge collapsed under its own load in 2005 (Figure 2.4). After conducting a comprehensive investigation, Naito et al. (2010) concluded that the quality of concrete was acceptable

Figure 2.3: Collapse of the Polcevera Viaduct, reprinted from (Bazzucchi et al., 2018) with permission.

even after the failure of the system. However, seepage of surface water into girder boxes could not be ruled out due to the existence of the holes on the top flange. In addition, the forensic investigation concluded that the average concrete cover had reduced to 40% less than what it was supposed to be in the primary design. According to the report published by structure management authorities, the presence of chloride laden moisture in the concrete deck increased the level of chloride content and caused the deterioration of prestressing members (Naito et al., 2010).

2.2.3 Bryant Patton Bridge, Florida

In 2004, the Florida Department of Transportation decided to replace the 40-year prestressed St. George Island concrete bridge crossing Apalachicola Bay with the new Bryant Patton Bridge because some piers of the old viaduct had lost up to 70% of their flexural capacity, as depicted in (Figure 2.5). After examining corrosion damage in 12 piers, two of which had been protected with a cathodic protection since 1994, Cannon et al. (2006) concluded that cathodically protected steel wires had been embrittled by hydrogen in 10 years, but the loss of flexural capacity in piers protected with ICCP was generally less than

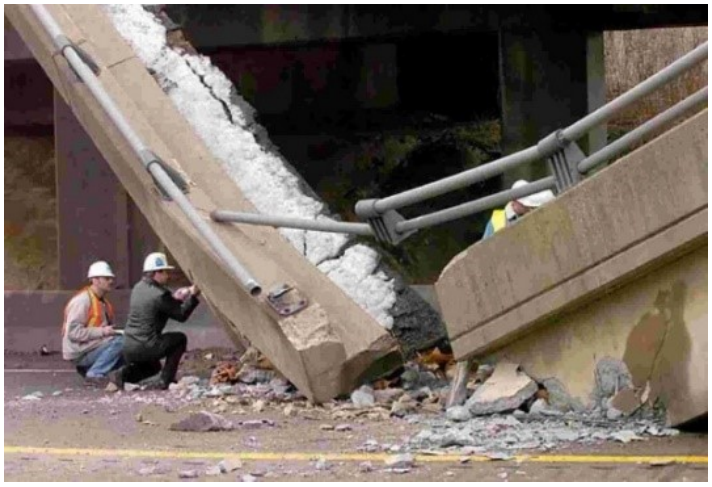

Figure 2.4: Failure of the Lake View Drive Bridge, reprinted from (Donaldson, 2005) with permission.

Figure 2.5: Corroded high-strength steel from the pile of the St. George Island Bridge, reprinted from (Cannon et al., 2006) with permission.

most other piers. The investigation showed the average hydrogen content dissolved in the prestressing steel was 2.0 ppm and 1.4 ppm for exterior and interior wires respectively. That said, it was 0.92 ppm for those cables which had not been protected with ICCP.

2.3 Imperfection of Existing Protection Systems

Preceding failures due to the presence of corroded components vividly indicates that the protection systems mentioned in Section 2.1 would not comprehensively preserve prestressing members from corrosion in concrete structures. As discussed previously, various protection

layers are expected to save reinforcement from an aggressive environment in cast-in-place and precast structures, yet both concrete-cover and grouted duct are the most effective protection systems against corrosive agents, particularly in the area with no construction joints. However, several cases of structural failures can be addressed (see Table A.1) for which the aforementioned techniques did not necessarily stop the ingress of contaminated solutions. For example, concrete spalling and reduction of concrete-cover still occurs as a result of environmental impacts, such as collision between debris and piers, or initiation of micro cracks along the reinforcement. Another example is box girder bridges that are built with both internal and external strands. Unless recesses around edges of segments and expansion joints in the box girder are properly sealed, chloride laden water may still gain access to prestressing members by leaking into the interior of the hollow box.

Both FHWA-NHI-13-026 (2013) and ACI 222.2R-01 (2014) highlight parameters that lead to corrosion failure of grouting systems protecting high-strength steel strands. Insufficient filling of ducts, bleeding and water seepage, segregation of grout, and an excessive amount of entrapped air in grout are the primary conditions which compromise the ability of grouting to protect from corrosion. FHWA-NHI-13-026 (2013) reports that contaminated run-off water easily penetrates voids within the grouted ducts through fitting and transverse joints, seams, and splices, which are not excellently watertight. An imperfect seal of inlet and outlet pipes after finishing the grouting process would also ease transportation of free surface water in post-tensioning ducts (Corven & Moreton, 2013).

Furthermore, durability of non-building structures directly depends on systems protecting anchorages and intermediate joints against contaminant solutions. Any defects in those regions readily allows water to leak into cavities between broken grout pieces in ducts and causes corrosion formations in steel strands. If a prestressed anchor is attacked by corrosive agents, cracks will then form in the surrounding concrete, leading to even more water ingress and transportation of contaminants to anchorage zones (ACI cmte. 222, 2014). Figure 2.6 demonstrates the typical protection levels of an anchor head in a post-tensioning system.

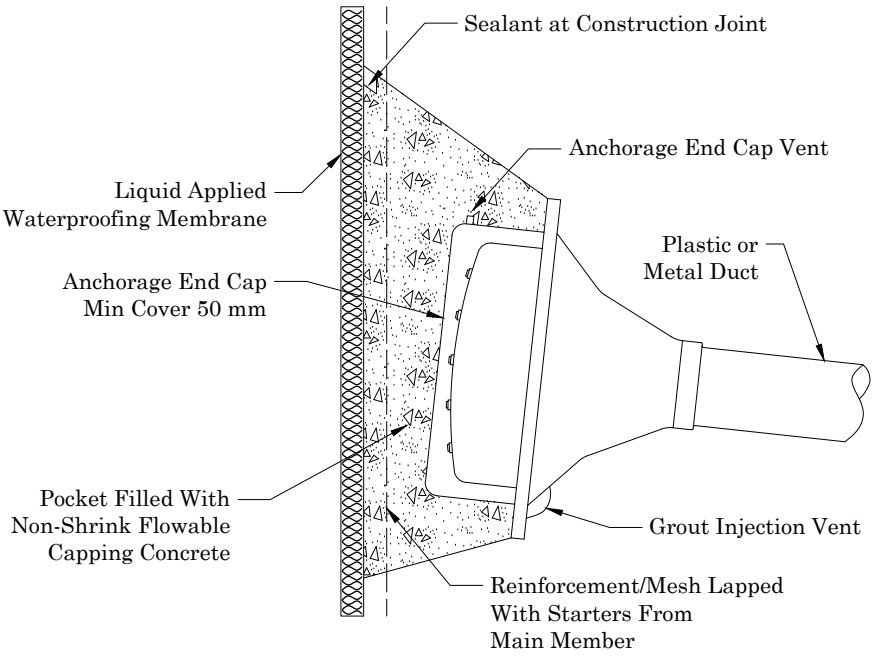

Figure 2.6: Anchor head protected with different layers in prestressed concrete slabs adapted from ACI 222.2R-01 (2014) with permission.

The protection system of anchorages includes filling the anchor area with grout, covering the anchor head with a plastic grout cap, encasing the grout cap with concrete pour-back, and using approved sealant to waterproof the anchor pour-back (Corven & Moreton, 2013).

Corrosion formations often occur during construction when steel wires are placed in ducts prior to grouting. Thus, it is essential to prevent runoff water mixed with site-debris and chemical pollutants from entering ducts. Similarly, improper drainage systems block water from draining away and leads to an accumulation of stagnant water close to prestressing cables, which causes oxidation of steel wires. Finally, inspection techniques used to check the condition of existing tendons can be destructive and subsequently result in pit initiation in steel wires (Corven & Moreton, 2013; ACI cmte. 222, 2014).

2.4 Corrosion Mechanisms in Concrete

Corrosion is a process in which a purified metal returns to its natural state where the ambient conditions (such as pH, relative humidity, temperature, oxygen, atomic hydrogen, etc.) favor the electrochemical process. Corrosion-related problems in the bridge industry

have been known for years. They lead to the degradation of reinforcement (refined metals) that has to be avoided since it decreases the structural capacity of elements in civil structures. Although an adequate thickness of the concrete cover is the most viable solution to preserve reinforcement from degradation in sub- and super structures, the feasibility of the protection system is dependent on factors making it impermeable, which is difficult to achieve in practice.

Concrete generally provides an alkaline environment with a pH between 12 and 13; yet, penetration of anions through the bulk and lower the pH to such a degree that a corrosive environment in concrete forms. These ions also break down the passive layer in metal and react with the ferrous and the ferric ions.

Corrosion in concrete is a self-accelerating process. As dense oxide layers form with a thickness greater than 100 μm (Broomfield, 2003), the swelling steel results in extensive tensile stresses on adjacent concrete, which causes deep-vertical cracks. This becomes worse overtime because the flaws make it easy for agents such as chloride ions to penetrate the concrete, resulting in a higher percentage of corrosion products. Other factors (such as thermal expansion, or creep and shrinkage) also cause these vertical cracks in concrete (Broomfield, 2003). If the crack was created as a result of a dense oxide layer, the aforementioned factors may cause horizontal cracks in addition to the existing vertical flaws. The horizontal cracks lead to concrete cover reduction and spalling as cleavage propagation occurs across the reinforcements.

The corrosion process is an inorganic spontaneous reaction that involves the movement of electrons between atoms. Figure 2.7 shows the corrosion process taking place based on the following reduction-oxidation electrochemical reactions (redox reactions),

$$\text{Reduction (cathodic reaction): } \frac{1}{2}\mathrm{O_2} + \mathrm{H_2O} + 2e^- \rightarrow 2(\mathrm{OH})^- \ , \tag{2.1}$$

$$\text{Oxidation (anodic reaction): } \mathrm{Fe} \rightarrow \mathrm{Fe}^{2+} + 2e^- \ . \tag{2.2}$$

where the oxidation term indicates that the iron atoms have a weaker pull on the electrons

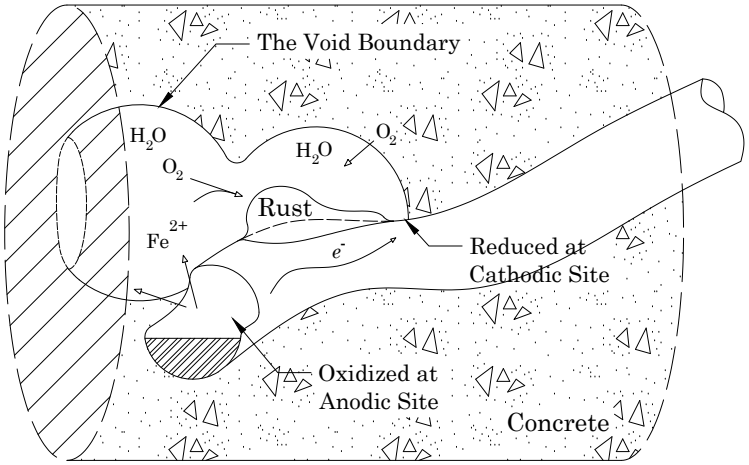

Figure 2.7: Electrochemical process leading to corrosion in concrete.

and consequently tend to lose them. The process is, of course, the opposite of what happens on the reduction side. Here, Pourbaix diagrams of iron, zinc, nickel, and cobalt are given in Figure 2.8 to illustrate the corrosion process occurring in iron and the metallic coatings suggested in this study.

The Pourbaix diagram describes a set number of chemical and thermodynamic relationships that are possible at a specified electrical potential and pH. Note that without the formation of metallic ions, the redox reactions in Eq. (2.1) and Eq. (2.2) cannot occur because there are not sufficient substances to participate in the process. Ferrous ions that are released in an acidic environment react with oxygen or hydroxides until the rate of the reactions reduces as a result of low concentration of cations, after which there is very little chemical activity. The electrochemical process begins once more as the environmental conditions change in favor of the redox reactions. A permanent solution to stop the destructive effect of the metallic degradation is to manually reduce the electrical potential of the metal so that the concentration of ferrous ions falls below some critical threshold. Therefore, corrosion does not occur regardless of any changes in the ambient conditions since the concentration of ferrous ions is so low that the redox reactions cannot proceed.

Broomfield (2003) outlined some thresholds to reduce the risk of corrosion failure in concrete structures. These restrictions stem from the fact that oxygen and water contents

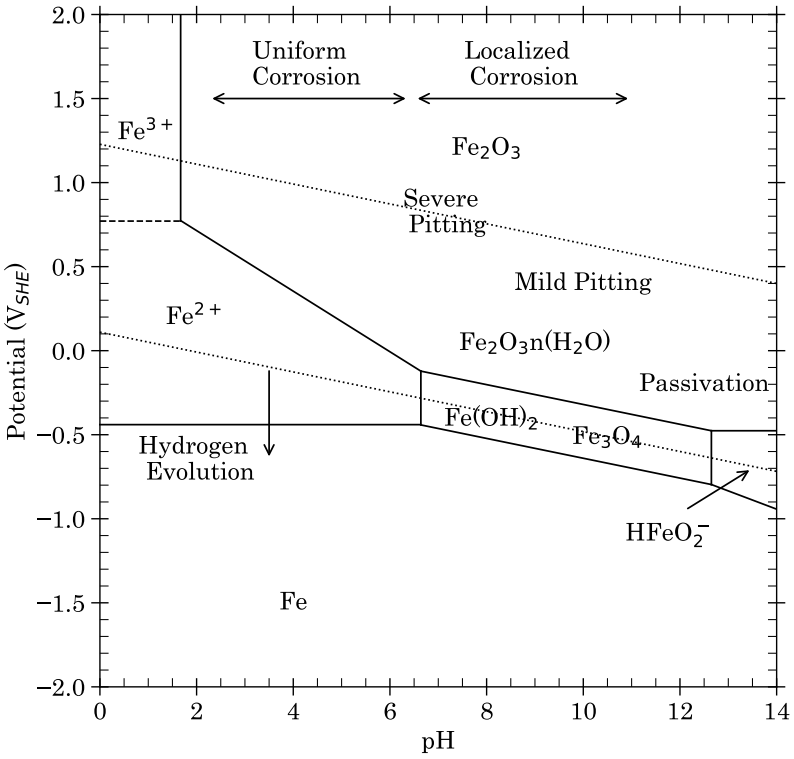

(a) Iron reprinted from (Roberge, 2012) with permission.

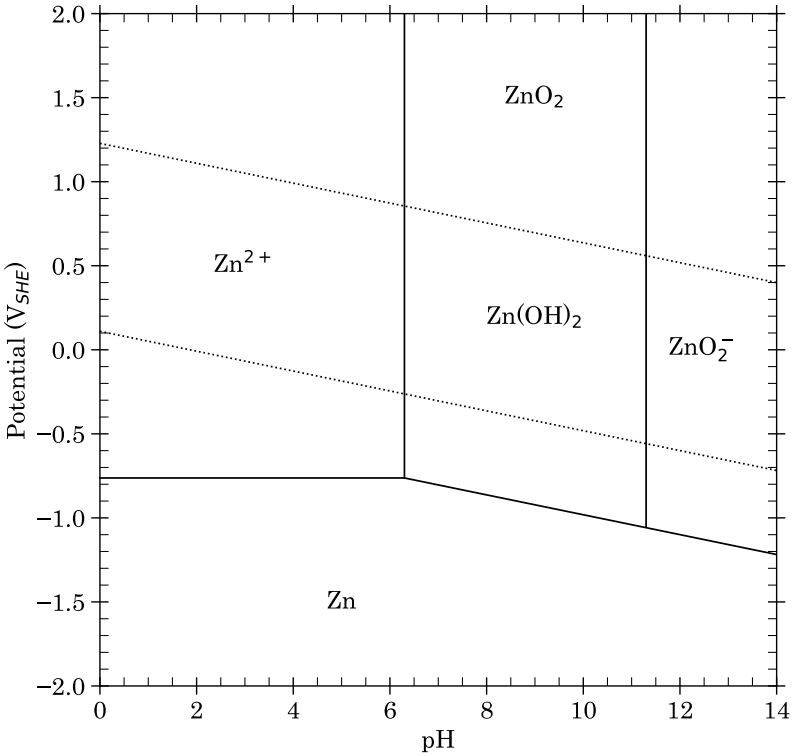

(b) Zinc reprinted from (Roberge, 2012) with permission.

Figure 2.8: Pourbaix diagrams at 25°C.

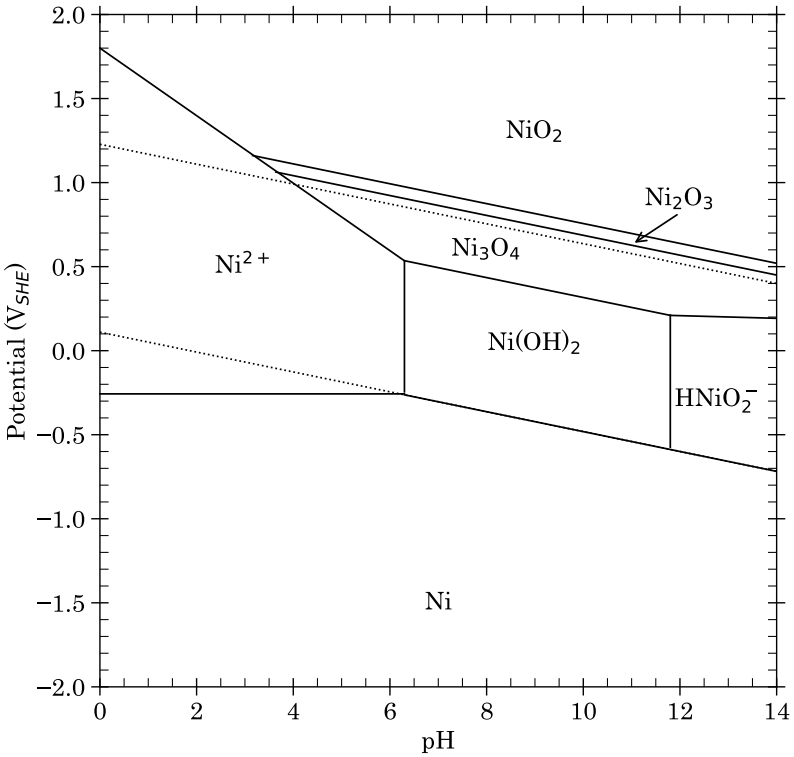

(c) Nickel reprinted from (Roberge, 2012) with permission.

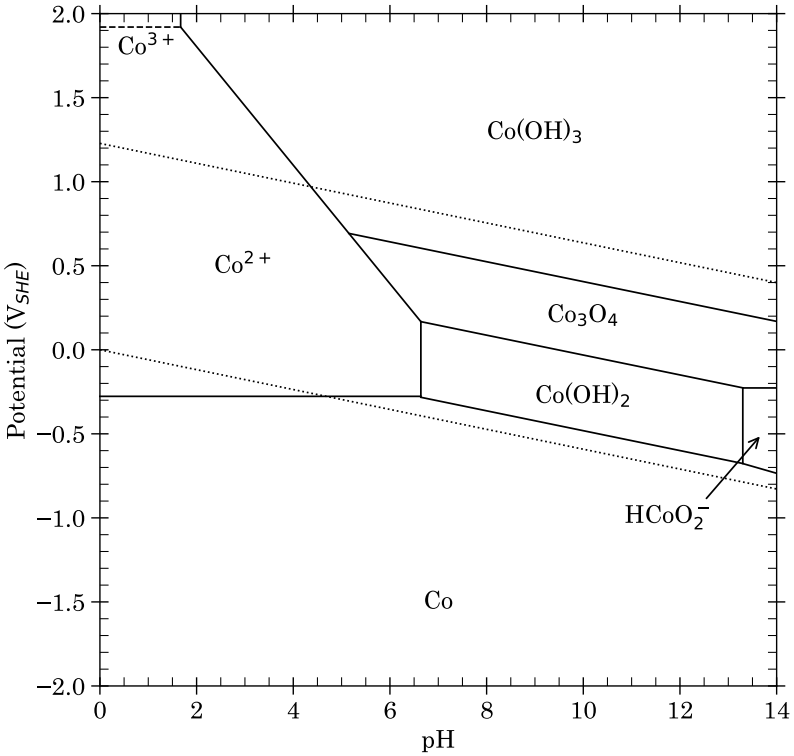

(d) Cobalt reprinted from (Zeng et al., 2015) with permission.

Figure 2.8: Pourbaix diagrams at 25°C, continued.

have to be limited in concrete so that the weight of offensive ions is minimized. Broomfield (2003) recommended that more than 1% chloride by weight of cement should not be allowed in concrete; even so, this threshold can be raised to 2% as stated in other literature (Mohammed et al., 2004; Roberts, 1962).

Today, chloride attack is a main cause of corrosion initiation in U.S. concrete structures. Studying the nature of this destructive attack, Broomfield (2003) suggested two separate phases: the primary phase where salt is added to a concrete mixture prior to casting, and the secondary phase where salt-laden water diffuses in the bulk. The former happens because the chloride content in cement gel crosses the defined threshold when seawater, sea sand, or chloride accelerators are used in concrete mixed design. The latter occurs where saline water penetrates the concrete. Several sources are responsible for the chloride diffusion in concrete bulk: deicing salt to melt ice on bridge decks, storing chemicals and salt-based products in concrete storage tanks, or marine structures where concrete is exposed to seawater.

Another cause of corrosion in concrete is carbonation that occurs when carbon dioxide ions transport through the concrete bulk and reach the surface of the reinforcement. As a result of gas penetration and the presence of moisture in concrete, carbonic acid will be formed in the pores and will eventually react with hydration products, more specifically with calcium hydroxide, and produce calcium carbonate. If the acid content rises over a set time scale, the corrosion product will form a greater volume; and consequently, the pH will drop and cause the degradation of steel components. Broomfield (2003) suggested increasing the thickness of the concrete cover, reducing the water to cementitious materials ratio, and maintaining an appropriate curing process to diminish the negative effects of carbonation in concrete. Carbonation is not a serious threat to U.S. bridges according to ACI 222.2R-01. In addition to this document, the investigation report of a recent prestressed bridge failure in Pennsylvania confirmed that carbonation had not occurred prior to the collapse of the bridge (Naito et al., 2010). That said, Puls (2013) reported carbonation related problems in seven historic bridges in Fort Worth, TX, that officials eventually decided to replace with new ones.

2.4.1 Porosity in Concrete

Concrete is not highly porous, but the volume fraction of microvoids in concrete influences the corrosion resistance of the system. If the water to cementitious materials ratio is kept relatively high, the void fraction of cement gel is expected to be significant. Conversely, reducing the ratio decreases the porosity in concrete, yet the presence of voids in gel should not be neglected. Cement gel is typically formed in a laminar layer with an average thickness of 3 nm, (Z. P. Bažant, 1975), while pores are distributed between hydrated particles with an average size from 100 nm to 1 μm. Interlayer pores are generally capable of encapsulating the adsorbed water. Bažant (1975) suggested that the size for macropores in cement gel should be limited to 2.6 nm, while voids smaller than this size should be considered as micropores. The average size of micropores in laminar gel can be assumed to be 1.5 nm. These low-volume voids are filled up with excessive amounts of so-called chemical water, which are produced in cement hydration reactions (Z. P. Bažant et al., 1997). A portion of this hindered adsorbed water again participates in a hydration process, but the rest can eventually diffuse through solid planes and feed the macropores as a result of the pressure gradient generated between voids (Claisse, 2014).

Figure 2.9a demonstrates a schematic representation of a typical void in cement gel, while a scanning electron microscopy (SEM) image of a microstructure of cement paste is portrayed in Figure 2.9b. As shown in this figure, capillary and gel pores can be found in hardened cement particularly at the interface between cement paste and aggregates.

Since pores are a great source of water, they can provide necessary conditions for redox reactions given in Eq. (2.1) and Eq. (2.2). As the steel surface meets pore water, ferrous hydroxide forms. This reacts with water and oxygen to produce ferric hydroxide, and later will be hydrated for extended periods of time to form the hydrated ferric oxide, or red rust. The final component is a well-known corrosion product, which is perfectly dense with a reddish-brown oxide layer. Eq. (2.3) to Eq. (2.5) represent chemical reactions that take place

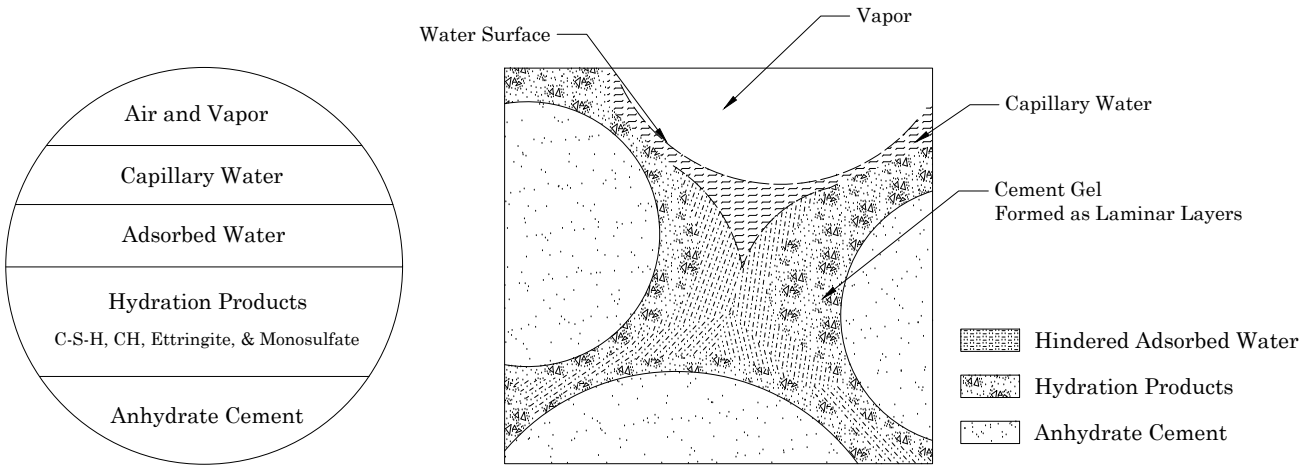

(a) Schematic representation of cement gel, adapted from Bažant (1972) with permission.

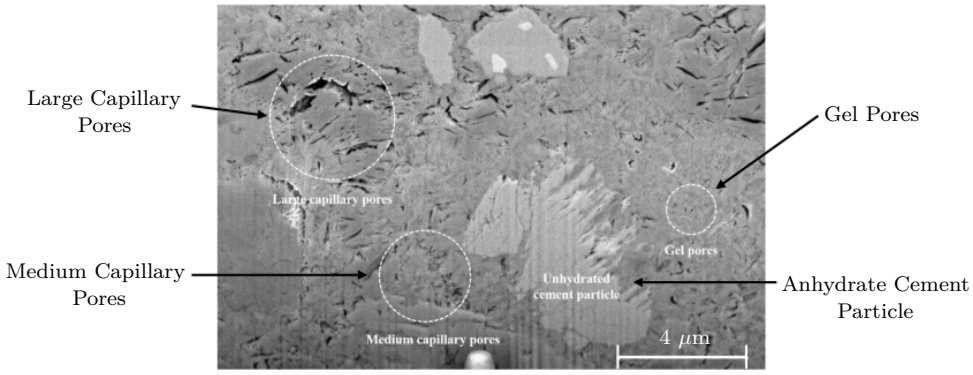

(b) Dual beam scanning electron microscopy of cement paste, reprinted from Lim et al. (2018) with permission.

Figure 2.9: Structure of cement paste.

to form the oxide layer on a steel surface.

$$\text{Ferrous hydroxide: } Fe^{2+} + 2OH^- \rightarrow Fe(OH)_2 \ , \tag{2.3}$$

$$\text{Ferric hydroxide: } 4Fe(OH)_2 + O_2 + 2H_2O \rightarrow 4Fe(OH)_3 \ , \tag{2.4}$$

$$\text{Hydrated ferric oxide: } 2Fe(OH)_3 \rightarrow Fe_2O_3.H_2O + 2H_2O \ . \tag{2.5}$$

Another product which can be formed in an electrochemical process is black rust. This is a blackish oxide layer that is produced when an insufficient amount of oxygen ions participate in the reactions. Note that the black rust film is not a dense layer that can cause cracks on the concrete surface. Therefore, it is extremely difficult to visually detect the degradation of

steel components (Broomfield, 2003).

Mechanisms of corrosion in prestressed systems are more complicated than the conventional reinforced concrete because tendons in prestressed concrete are under constant tension within an average of 60% of its ultimate tensile strength (Treadaway, 1971). Therefore, brittle failures in addition to localized and uniform corrosion are possible in prestressing strands. Furthermore, a failure of prestressed tendons due to other types of corrosion occurs faster than conventional reinforcement because high carbon steel strands are typically built with smaller diameters (ACI cmte. 222, 2014). Hence, any solution to prevent corrosion in prestressed concrete not only has to protect steel from typical corrosion processes (such as uniform and pitting corrosion), but should also provide protection from brittle failure of steel due to corrosion cracking and hydrogen embrittlement.

2.4.2 Pitting Corrosion

Pitting corrosion occurs in both acidic and alkaline environments. If a pit forms on the surface metal, it leads to the degradation of low-relaxation strands at a fast rate. This is a form of localized attack and is very destructive. A pit is a small cavity with a relatively deep penetration depth (Popov, 2015). Although this is a small-size defect, propagation of a pit reduces the cross-sectional area and essentially results in the failure of the steel component. A pit may initiate as a result of chemical attacks or because of injurious defects and holidays. In addition to these mechanical flaws, pitting corrosion more often begins because of inclusions, which have been introduced in steel during the metallurgical process (Mondal, 2014).

Figure 2.10 demonstrates the mechanism of a pit formation in a steel wire embedded in concrete. When salt-laden water is stored in voids adjacent to the metal surface, chloride ions penetrate through the oxide film and react with the iron ions resulting in ferrous chloride. Then, the inorganic product interacts with water stored in pores and produces ferrous hydroxide. Hydrochloric acid is another component that forms during electrochemical reactions. The acid essentially brings the ambient pH down causing degradation of the passive layer and further redox reactions. The activities eventually adjust the metal potential to

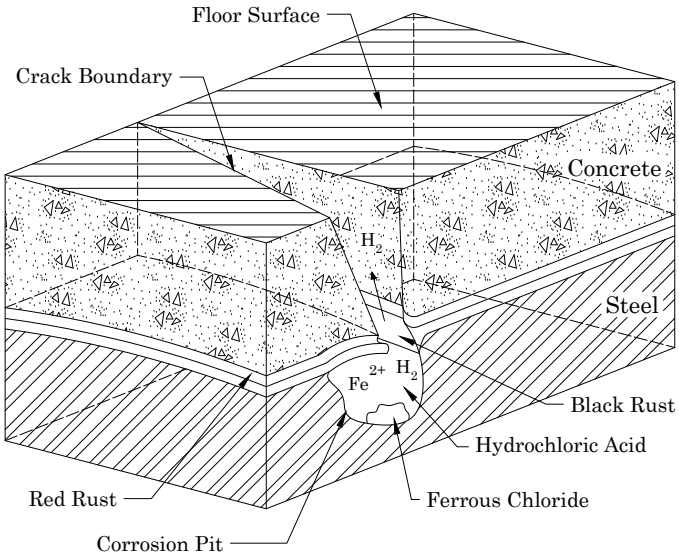

Figure 2.10: Formation of a pit in a steel wire.

the level that pitting corrosion occurs (Popov, 2015). The oxygen concentration inside the anodic side is relatively low compared to the cathodic side, thus a corrosion cell develops as a result of this inequality that leads to deposition of ferrous hydroxide on the solid surface and the release of hydrogen atoms in the small cavity (Mondal, 2014). The mechanism of initiation and propagation of a pit can be summarized in following reactions

$$FeCl_2 + 2H_2O \rightarrow Fe(OH)_2 + 2HCL \ , \tag{2.6}$$

$$Fe^{2+} + 2H_2O \rightarrow Fe(OH)_2 + 2H^+ \ . \tag{2.7}$$

A formation of a pit in high-strength steel wires intensifies the risks associated with other types of corrosion, such as corrosion cracking and atmospheric corrosion. Figure 2.11 shows a typical example of corrosion pits in high-strength steel coated with nickel-cobalt alloy.

2.4.3 Brittle Failure

Brittle fractures often occur in metallic components that are placed in a corrosive environment and experience continued tensile stresses. The failure of these elements normally happens with minor elongation and without evident visual sign (ACI cmte. 222, 2014).

Figure 2.11: Pitting corrosion. Corrosive agents attacked ASTM A 416 steel coated with nickel-cobalt alloy and caused the formation of corrosion pits.

Regarding non-building structures, prestressed wires are highly susceptible to corrosion cracking because they experience tensions of 60%, or higher, of their ultimate tensile strength (Treadaway, 1971). Moreover, a risk of brittle failures also increases for high-strength metal. Regarding the study of corrosion cracking, it is essential to differentiate between corrosion fatigue cracking (CFC), stress corrosion cracking (SCC), and hydrogen embrittlement (HE). From these three brittle failures, initiation of corrosion fatigue cracking in U.S. bridges and parking garages is rarely discussed in the literature, but SCC and HE are widely addressed as a serious threat to those structures. Figure 2.12 shows a brittle fracture of a steel cable as a result of hydrogen induced cracking.

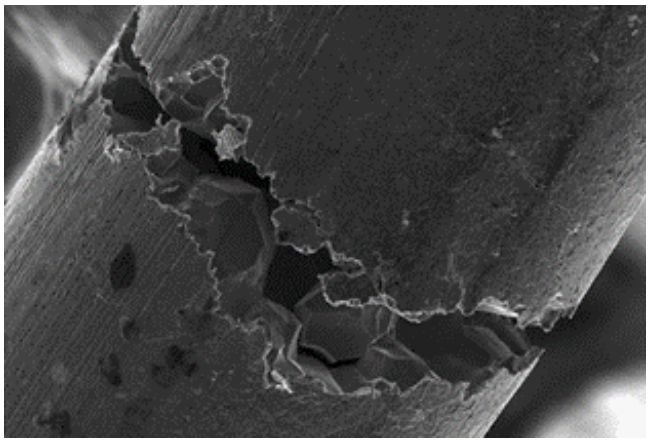

Figure 2.12: Brittle failure of high-strength steel wire as a result of SCC or HE, reprinted from (Popov, 2015) with permission.

Figure 2.13: Rupture of steel wire due to fretting fatigue, reprinted from (Winkler et al., 2015) with permission.

2.4.3.1 Fretting Fatigue

Fretting Fatigue is a brittle failure initiated in a gaseous medium if steel strands are gradually abraded due to cycling loading. When prestressing strands are under tension, a cold welding forms as a result of excessive compression force between contact surfaces of wires (Mondal, 2014). If tendons are subjected to a vibration load, then cables tend to slip past one another and welding edges are broken off. Consequently, the surface wires are gradually eroded at the contact areas leading to removal of the oxide film and a formation of pits (Figure 2.13). ACI 222.2R-01 reported that 0.04 μin slip of low-relaxation steel wires is enough that fretting corrosion forms on the metal surface. Hence, only little motion is required to result in an abrasive wear of steel components.

ICCP does not directly protect the metal from fretting fatigue. In fact, fatigue related failures often happen with a combination of SCC or HE. Thus, adequate potential that prevents brittle failures of prestressing strands would also lead to reducing the negative impact of fretting fatigue in concrete structures.

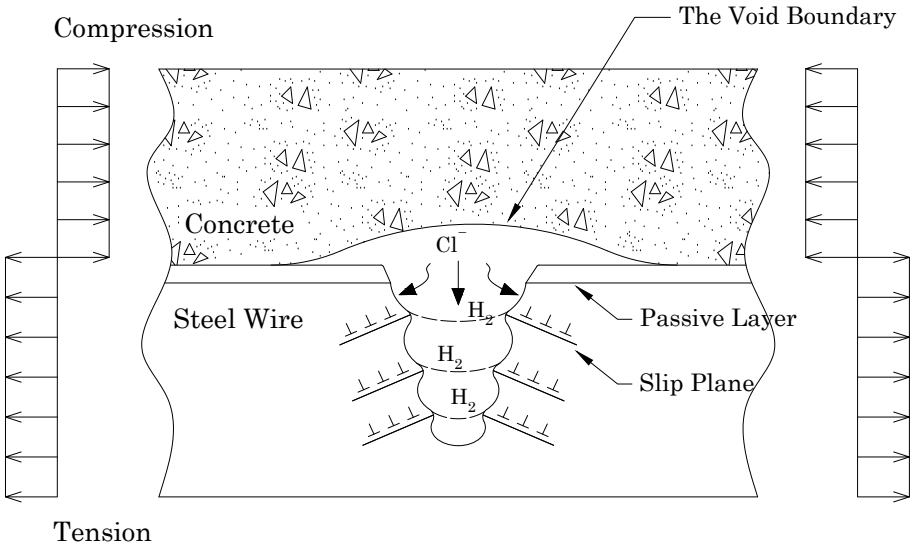

Figure 2.14: Schematic representation of stress corrosion cracking according to dissolution-based theory and cleavage control Mechanism.

2.4.3.2 Stress Corrosion Cracking

Stress corrosion cracking occurs when tendons are experiencing tensile stresses that are 60% or more of the metal yield strength (Mondal, 2014). This type of brittle failure is possible in any conditions, and it is not necessarily isolated to corrosive environments according to ACI 222.2R-01 (2014). The exact mechanism that leads to stress corrosion cracking in metals is not known. However, a common belief is that applied or residual stresses along slip planes open micro cracks on the metal edges causing a rupture of the passive layer. Then, the redox reactions proceed as soon as iron is in contact with the corrosive solution. As the deformation proceeds along the active plane, the rate of dissolution will be greater than passivation resulting in a brittle fracture in steel wires over a period of time (Figure 2.14). The process can be defined according to the dissolution based theory and cleavage control mechanism (Mondal, 2014). Alanso et al. (1993) investigated the formation of SCC in prestressed concrete. The authors observed that brittle failure happens at the crack tip if the ambient pH is higher than 9.7; otherwise, a localized attack such as pitting would occur rather than SCC (ACI cmte. 222, 2014). Moreover, hydrogen embrittlement intensifies

propagation of stress corrosion cracking in prestressing strands in a way that hydrogen ions produced in electrochemical reactions easily diffuse in pearlite layers at the crack tip and cause embrittlement of wires (Song et al., 2011). Both Alanso et al. (1993) and Song et al. (2011) concluded that SCC is a potential dependent phenomenon. ACI 222.2R-01 reported the relative potential required to a formation of stress corrosion cracking is above -600 mV vs. SCE.

2.4.3.3 Hydrogen Embrittlement

Another brittle failure that is likely to occur in prestressed concrete structures is hydrogen embrittlement. This type of failure is a well-known phenomenon that has been studied since the 19th century when Johnson (1875) published one of the earlier works on corrosion of steel components due to hydrogen atoms and acidic solutions. Regarding high-strength steel wires, hydrogen contamination is essentially introduced in metal during the metallurgical work. However, gaseous atoms would escape to the surrounding environment later in the baking process. That said, not all hydrogen atoms leave the iron crystal. In fact, some portions of these atoms are stored in defects and traps in the metal lattice. When the atomic size of hydrogen ions generated during redox reactions pass the barriers and diffuse into the steel crystalline lattice, they will combine with the molecular hydrogen encapsulated in traps and raise localized pressure in the metal. In addition, transportation of atomic hydrogen between the crystalline structures also alters the metal mechanical properties (Popov, 2015). In fact, the steel wires gradually become brittle and eventually break, similar to ceramics (Figure 2.15).

Bhadeshia (2016) investigated the initiation of a brittle fracture in iron base elements as a result of hydrogen diffusion. A key point highlighted in the author's work is that only the atomic size of hydrogen atoms generated during reactions are capable to diffuse in substrate and cause the beginning of embrittlement process, while the molecular size of hydrogen atoms essentially does not result in the initiation of HE in the steel substrate.

Although it is difficult to differentiate between stress corrosion cracking and hydrogen

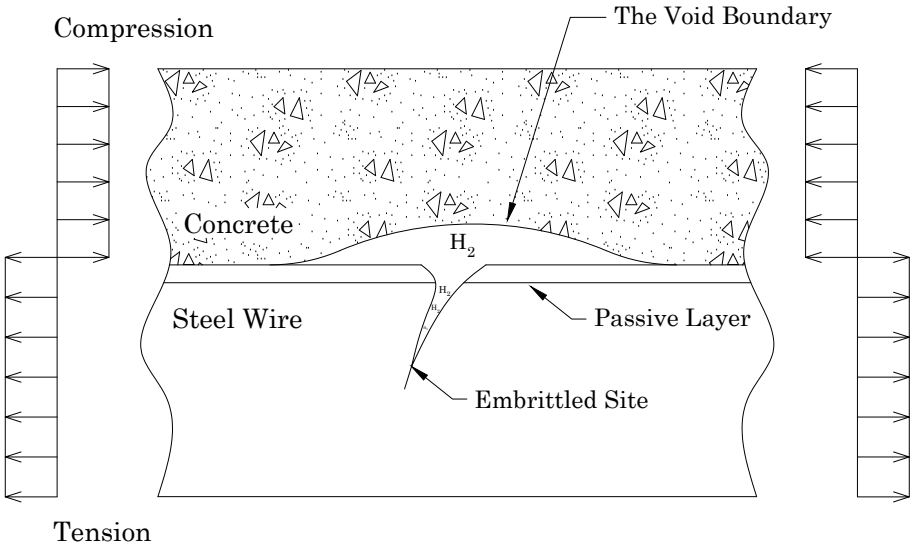

Figure 2.15: Schematic representation of hydrogen embrittlement in high-strength steel.

embrittlement, the nature of hydrogen diffusion in low-relaxation strands is entirely different from SCC. Hydrogen atoms diffuse in steel at any conditions. For example, there are a few reports (ACI cmte. 222, 2014) that wires were observed to be embrittled even before stressing out and grouting injection. As discussed, cathodic protection shifts the equilibrium in favor of hydrogen evolution, thus a large amount of hydrogen atoms become available for transport in the crystalline structure of wires. ACI 222.2R-01 reported if the relative potential of steel elements is less than -900 mV vs. SCE, then the likelihood of hydrogen diffusion in substrate increases. Figure 2.16 shows the propagation of possible brittle fractures happening in high-strength steel cables as time passes.

2.4.4 Microbiological Corrosion

This type of corrosion occurs when a metal component is corroded due to bacterial activities. Microbiological corrosion can usually be found at the metal surface contacting soil and groundwater. However, regarding prestressed concrete, lubricants such as oil emulsion—which protects post-tensioning wires prior to grouting injection—can support bacterial growth. Another example of microbiological corrosion is when prestressed cables and post-tensioned piers are exposed to industrial waste elements. Papé and Melchers (2008) studied corrosion

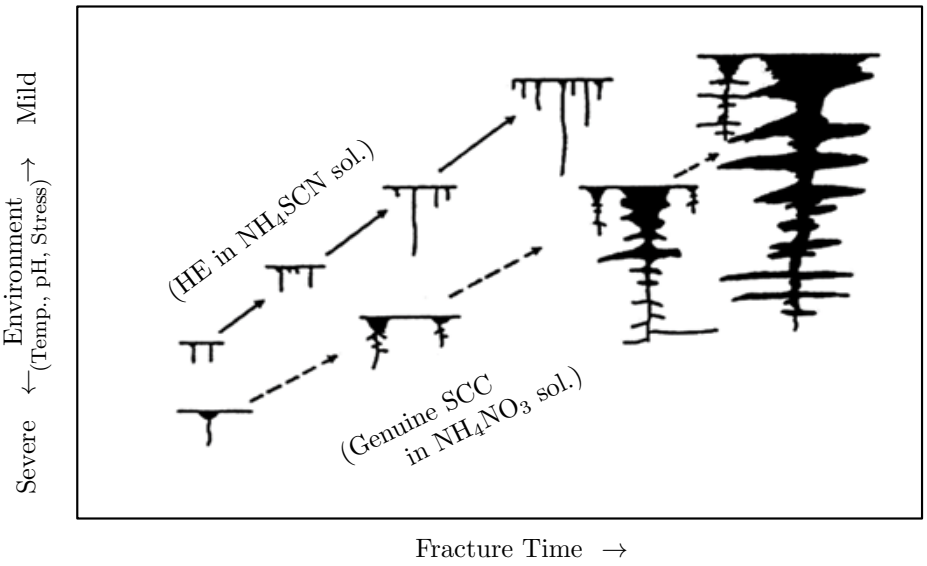

Figure 2.16: Comparison between stress corrosion cracking and hydrogen embrittlement in high-strength steel strand, reprinted from ACI 222.2R-01 (2014) with permission.

Figure 2.17: Corrosion propagation due to bacterial activities, reprinted from (Little & Staehle, 2001) with permission.

formations on the 45-year prestressed Sorell Causeway after the bridge was replaced in 2002. The authors observed signs of bacterial activity on some ligatures and strands. Little and Staehle (2001) investigated the possibility of localized corrosion initiation and a brittle failure of post-tensioned cables as a result of the presence of fungi (Figure 2.17). Their conclusion stated that bacterial activities reduce the ambient pH and lower concrete quality.

Bacterial activities can proceed in both aerobic and anaerobic conditions. The risk of microbiological corrosion occurrence in anaerobic conditions is more plausible in concrete

structures. As an example, sulfate-reducing bacteria may consume hydrogen atoms that cause a chemical reaction leading to bisulfite production. Then, black ferrous sulfide and hydrogen sulfide will be produced as a result of a reaction between bisulfite and iron. The former initiates localized corrosion such as pitting, and the latter drops the ambient pH which results from an acidic environment. In fact, bacteria can survive in such an environment as long as the ambient temperature remains between 35°C and 40°C and pH falls between 5.5 and 8.5 (Popov, 2015).

2.4.5 Galvanic Corrosion

Galvanic corrosion begins after setting up a potential cell between two metals. During this process, a metal with more negative potential loses electrons and essentially corrodes. Hence, a potential cell will be generated in a set number of electrochemical reactions. In fact, corrosion activities proceed forward because of the potential difference between the metals. A well-known example of galvanic corrosion is a zinc coating of steel reinforcement in concrete, known as a sacrificial coating. As corrosion reactions begin, zinc is consumed and protects steel from corrosion. The sacrificial coating system is widely used in reinforced concrete, but its utilization in a prestressed system is questionable. The hydrogen atoms produced in redox reactions easily diffuse in the coating layer and cause the substrate to become embrittled. Therefore, the use of galvanized prestressed cables in North American bridges is banned by the Federal Highway Administration (ACI cmte. 222, 2014).

Another type of galvanized corrosion would be possible in prestressed concrete is when a potential cell is built up between galvanized corrugated ducts and low-relaxation prestressing tendons. For example, galvanized ducts can be oxidized and lose material as time passes. Thus, a defected duct will no longer act as a protective barrier. In addition, potential cells established between galvanized components and steel strands can lead to the shielding effect that makes the application of cathodic protection difficult.

2.4.6 Corrosion Behavior of Reinforcement in Concrete

It is common to obtain a polarization curve to describe the transition between passive and active states and analyze the kinetics of the electrochemical process taking place in concrete. Studying the polarization curve also helps to identify the driving potential required for the steel protection. The typical polarization curve for steel embedded in concrete is shown in Figure 2.18. As illustrated in this figure, increasing the chloride contents adjacent to the reinforcement lowers the voltage for the passive state.

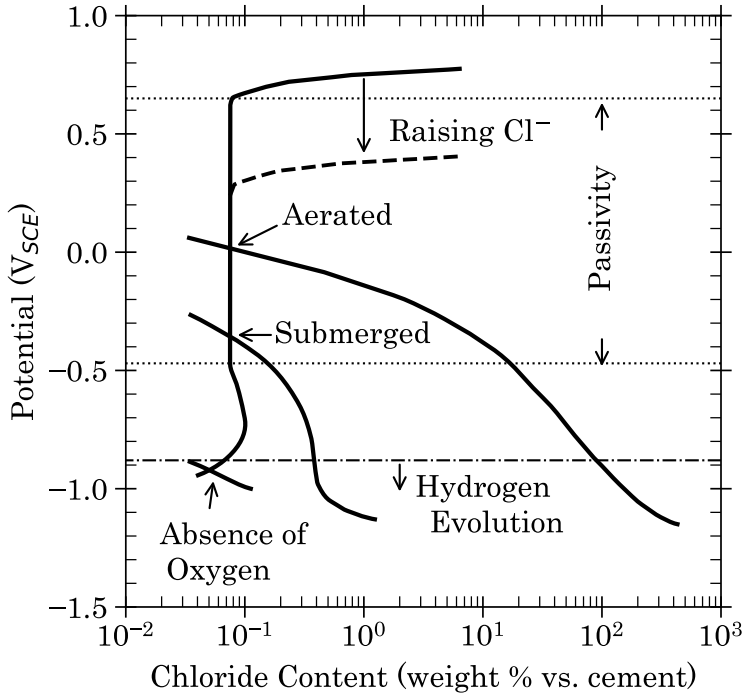

Figure 2.18: Polarization curves, reprinted from (Bertolini et al., 2004) with permission. Herein are anodic and cathodic reactions in reinforced concrete placed in aerated environment in addition to submerged in water and in absence of oxygen.

Pedeferri (1996) studied the corrosion behavior of steel embedded in concrete with applying an impressed current. Figure 2.19 shows the diagram reported by the author and identifies the potential of steel in concrete with respect to chloride content. Here, the Pedeferri diagram is modified by considering the potential needed to avoid corrosion cracking and brittle failures.

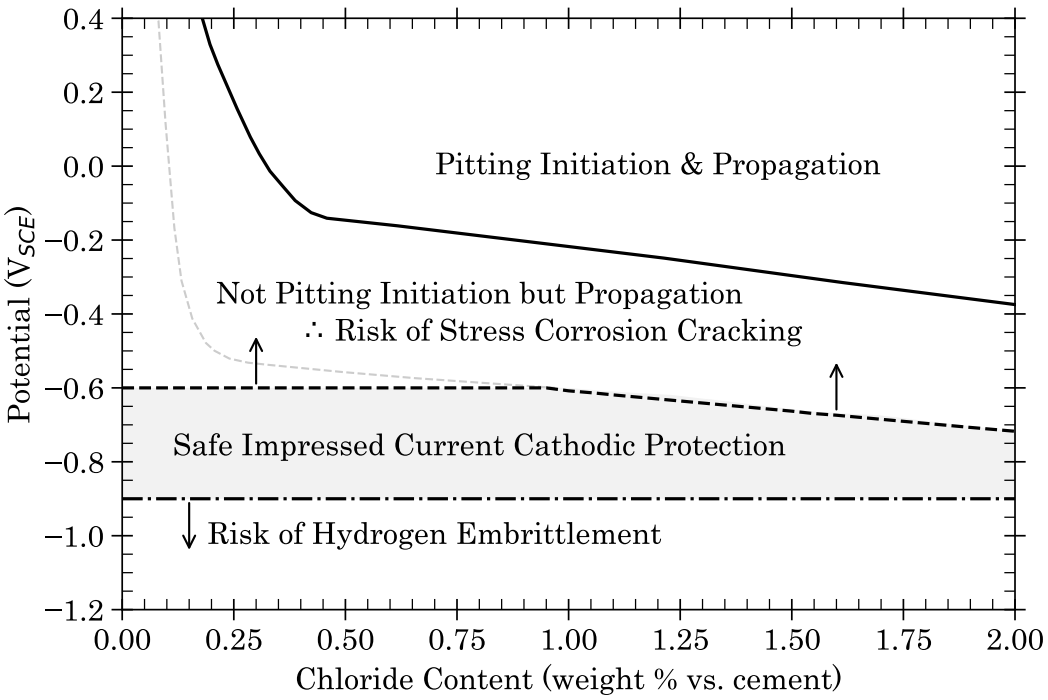

Figure 2.19: Pedeferri diagram. Corrosion behavior of steel embedded in concrete based on electric potential and chloride content, modified for ASTM A 416 steel from (Pedeferri, 1996) with permission.

As it is evident from Figure 2.19, the range of potential, possible to operate for a safe cathodic protection, reduces with increasing the chloride content adjacent to prestressing tendons. This can be more prominent if the risk of hydrogen embrittlement is also taken into consideration.

2.5 Cathodic Protection

Application of cathodic protection in reinforced concrete has already been approved for decades. Austin (2010) noted that more than 700 reinforced sub- and super structures in the UK are protected by cathodic protection. That said, the cost of anode systems as well as some drawbacks related to overprotection can be reasons that bridge owners and authorized officials may avoid the utilization of ICCP in concrete structures. Broomfield (2003) pointed out that concerns about the cost of cathodic protection can be overlooked in the long run when a non-building structure such as a long span bridge is considered. However, the formation of corrosion cracking, more explicitly in prestressed concrete, is a serious concern that ought to

be addressed precisely.

2.5.1 History of Cathodic Protection in Concrete Structures

Today, there is no doubt that ICCP is the most reliable technique to protect the reinforcement from corrosion in an aggressive environment. The idea of introducing an impressed current to control the corrosion rate in a bridge deck was proposed by Stratfull in the 1970s (Pedeferri, 1996). After that, there were some contributions to improve anode systems until Pedeferri (1996) used cathodic protection to prevent corrosion formations in new reinforced concrete structures (Bertolini et al., 2004). In the meantime, a number of research studies were conducted mainly in the U.S. to investigate the feasibility of applying this technique in prestressed concrete (Hope & Ip, 1993; Novokshchenov, 1994; Enos et al., 1997; Chaix et al., 1995; Enos et al., 1998). The goal was to understand whether or not corrosion cracking failures occur in prestressed pilings placed in seawater as a result of cathodic protection. In the end, all studies agreed that hydrogen embrittlement may not cause the failure of tendons if the steel potential is maintained at -900 mV vs. SCE. Since then, ICCP has protected prestressed pilings in a marine atmospheric environment, such as the coastal regions of Florida.

Shifler et al. (2005) discussed factors influencing the corrosion rate in marine structures. The rate of reinforcement degradation in a concrete pier placed in brackish and seawater relies on the acidity of the environment, the time of concrete wetness, and the oxygen diffusion rate as a result of an extensive wind. Therefore, impressed current has to be continuously applied to save the steel members from an aggressive environment in those structures. That said, Presuel-Moreno et al. (2005) conducted a research study to understand long-term consequences of cathodic protection in concrete structures placed in a marine environment. The authors studied the corrosion mechanism in a concrete column for almost nine years and concluded that corrosion would not initiate in reinforcement right after stopping the polarization process, but it can be expected to propagate again in a month or so. On the other hand, Hartt et al. (1995) reported that localized protection of an impressed current

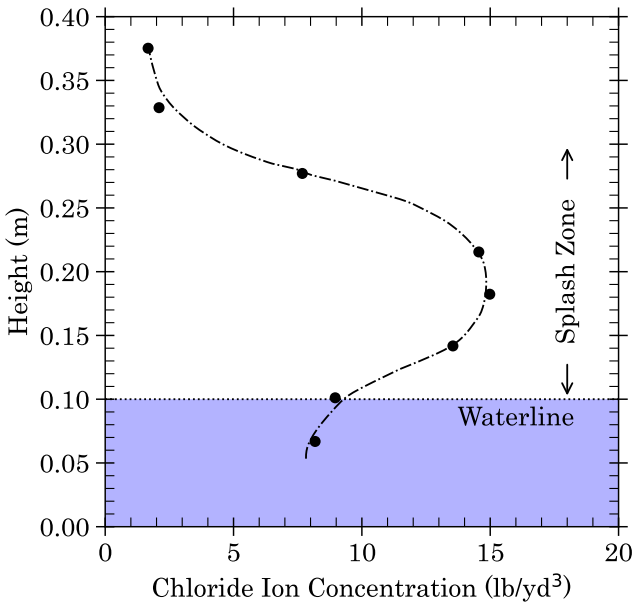

Figure 2.20: A comparison between the distribution of chloride content in a prestressed piling at splash zone and submerged region based on a laboratory study, modified from (Chaix et al., 1995) with permission.

does not necessarily depend on the concrete properties but relies on the anode's height. Note that corrosion related problems in marine structures are more probable to occur in the splash zone where the spray water evaporates due to sunlight and wind, and residual salts accumulate in the concrete bulk (Figure 2.20).

Enos et al. (1998) investigated the initiation of hydrogen embrittlement in a prestressed piling in both the splash zone and the submerged region as a result of long-term cathodic protection. The authors specified that time is a variable in the formation of corrosion in marine structures, while position, due to the nonuniform resistivity of concrete, also affects the corrosion initiation in prestressed high-strength steel strands. Furthermore, it was concluded that -780 mV vs. SCE is required to protect the prestressed tendons from corrosion for almost 40 cm above and below the waterline without any formation of hydrogen embrittlement, which could be achieved by applying an impressed current at the level of 1.33 μA/cm^2 for 48 days. Figure 2.21 represents the results reported by Enos et al. (1997). As shown, hydrogen permeation in prestressed strands increases upon the potential drops in tendons.

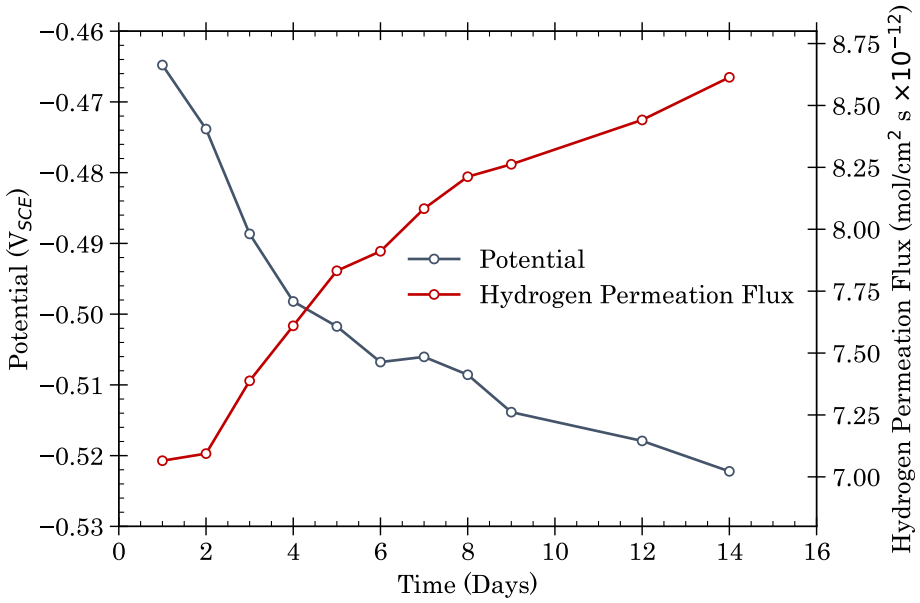

(a) Results from the splash zone at current density 1 μA/cm^2. pH level was 4.8 for the splash zone.

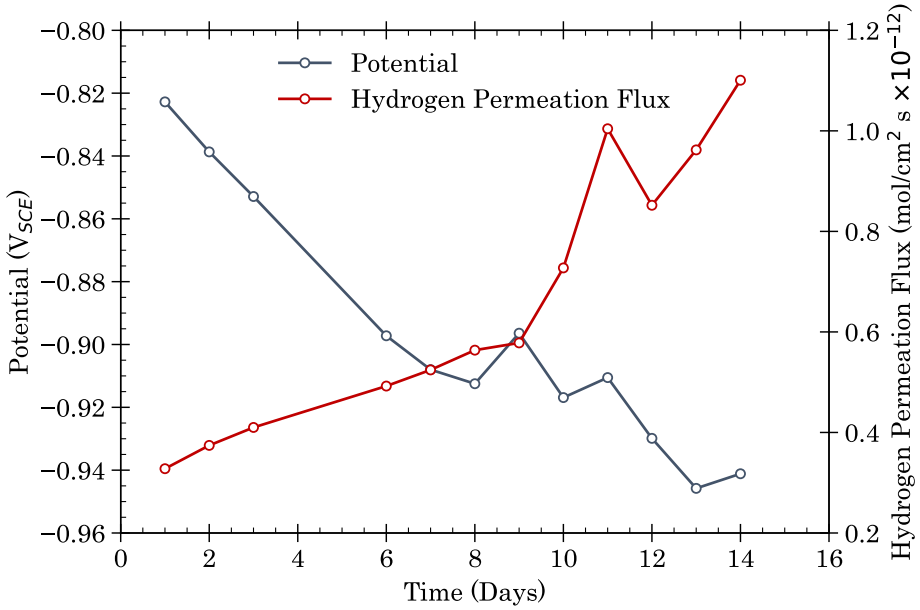

(b) Recordings for the submerged region at current density 2 μA/cm^2. pH level was 11.8 for the submerged region.

Figure 2.21: Potential distribution and the rate of hydrogen permeation in a laboratory prestressed piling, adapted from Enos et al. (1997) with permission.

2.5.2 Drawbacks of Cathodic Protection

Despite the advantage of cathodic protection to reduce the corrosion rate, there are some negative consequences of applying an impressed current in concrete structures. Some of these disadvantages have already been discussed, yet more details will be highlighted in this section.

2.5.2.1 Corrosion Cracking

As steel electric potential drops below -900 mV vs. SCE, hydrogen evolution happens at a fast rate as a result of overprotection (ACI cmte. 222, 2014). If so, atomic hydrogen formed in an electrochemical process readily embrittles reinforcement causing the failure of the member. This is indeed an existing challenge to utilization of cathodic protection in order to protect prestressed structures from the corrosion. Brittle failures in prestressing strands do not occur just as a result of the impressed current. If sulfuric acid is produced by bacterial activities adjacent to the high-strength steel wires, then the risk that corrosion cracking occurs in steel strands noticeably increases. Moreover, the brittle failure can also happen in the metal because of aggressive agents such as nitrate ions that sometimes are available in concrete constituent materials (Treadaway, 1971).

2.5.2.2 Alkali–Silica Reaction, ASR

When alkaline hydroxides react with siliceous aggregates in a highly alkaline environment, sodium silicate gel forms leading to alkali–silica reaction (ASR). This phenomenon is sometimes referred to as 'concrete cancer' because of its devastating effect on concrete durability. Pedeferri (1996) mentioned that ASR can take place as a consequence of long-term cathodic protection in reinforced concrete. A formation of ASR gel should be a matter of concern when higher current density more than 1 μA/cm^2 is applied to concrete structures.

2.5.2.3 Shielding

Metallic or plastic ducts in post-tensioned concrete can divert the electric potential target that has been designed to protect prestressing tendons. In other words, a metallic duct

may absorb a portion of the current required to save steel strands from corrosion; on the contrary, a plastic duct may act as an electrical insulator and block the current needed for cathodic protection (ACI cmte. 222, 2014). Other steel reinforcement such as stirrups may also absorb a portion of the impressed current distributed in the concrete bulk. Concrete is a nonconductive and nonhomogeneous material; consequently, its electrical resistivity is not uniform throughout the concrete bulk. Hence, the potential distribution as a result of an impressed current is not consistent in concrete.

Figure 2.22 represents a study coordinated by Pedeferri (1996) on a 100 m concrete slab with 20 cm depth with a relative humidity up to 85%. As illustrated in this figure, the potential distribution in the reinforced concrete slabs is nonuniform and decreases in magnitude as distance from the titanium net located at the top of slab; hence, it is difficult to impress sufficient current to protect reinforcement at the bottom side. Similar to reinforced concrete, tendons embedded in pretensioned or post-tensioned concrete ought to receive the required current so that steel strands are cathodically protected, which is sometimes difficult to achieve in practice.

2.5.2.4 Adhesion Loss Between Concrete and Reinforcement

Pedeferri (1996) noted the possibility of adhesion loss between reinforcing steel and concrete constituents, especially in the case of non-ribbed steel, when the metal potential is -1100 mV vs. SCE. Hence, it can be argued that utilization of ICCP has to be treated with some caution in prestressed structures that are continuously under tension. However, separation of high-strength steel wires and high-quality concrete, or grout in post-tensioning systems, is unlikely because the mechanisms of interaction between strands and concrete are not similar to conventional reinforced concrete. This will be discussed later in Section 2.7.

2.6 Metallic Coating

The primary corrosion protection in prestressed concrete is achieved by a thickness of sound crack-free concrete. To protect reinforcement from corrosion, AASHTO (2012) mandated at

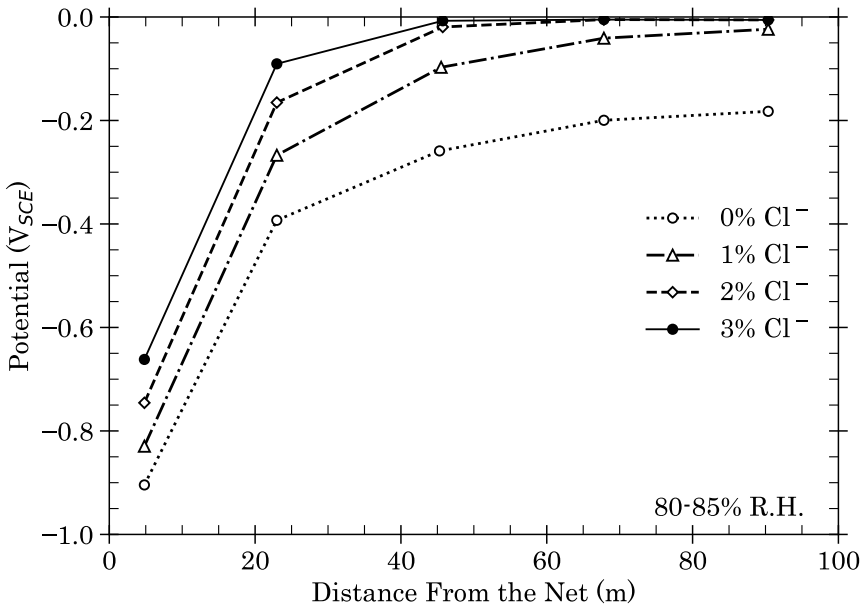

Figure 2.22: Polarization of the reinforcement due to cathodic protection on $100 \times 20 \times 20$ centimeters concrete slab. Titanium net was placed on the top of the reinforced concrete, reprinted from (Pedeferri, 1996) with permission.

least 2 and 3 inches [5 and 7 cm] of concrete cover in a non-corrosive environment and in a coastal region and marine environment, respectively. These conditions are valid as long as cracks with a width of 0.004 inches [0.25 mm] or greater do not appear on the concrete surface (Moore et al., 1970). If so, then reinforcement can easily be exposed to corrosive agents and could be corroded after only a short time has elapsed. Corrosion is a time-dependent process, yet it usually happens fast and with no sign of warnings in the case of prestressed concrete.

A low-relaxation strand used in prestressed structures is composed mainly of iron as well as 0.8% carbon in weight and small fractions of the other elements such as manganese, silicon, copper, etc. The crystal structure of a high strength steel wire at room temperature consists of ferrite and pearlite, the reader is referred to the SEM image of the as-received ASTM A 416 wire portrayed in Figure 2.23. Ferrite includes iron atoms structured with a body-centered cubic (BCC) lattice pattern, and pearlite is alternating layers of ferrite and cementite (Fe_3C). The former is a low carbon layer, yet carbon content in longitudinal cementite layers is so high that it results in increasing the strength of the steel wire.

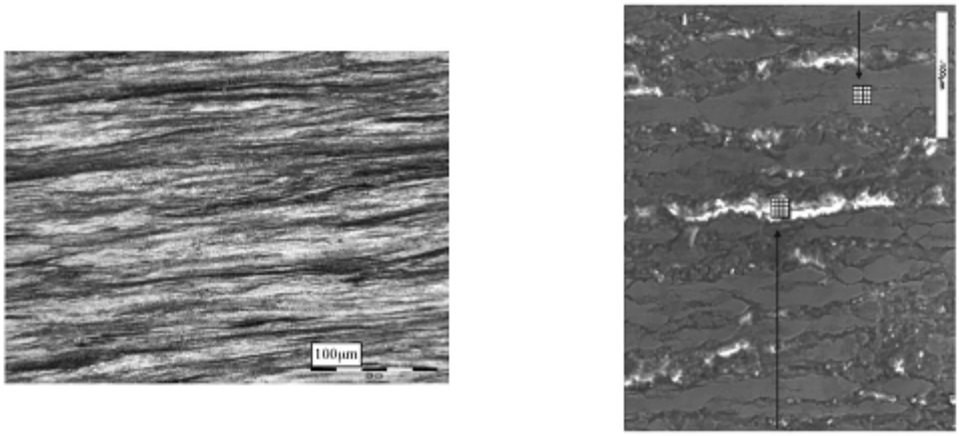

Figure 2.23: SEM image of as-received ASTM A 416 wire representing longitudinal pearlite microstructure (left) and heterogeneous phosphate coated layer (right), reprinted from (Díaz et al., 2009) with permission.

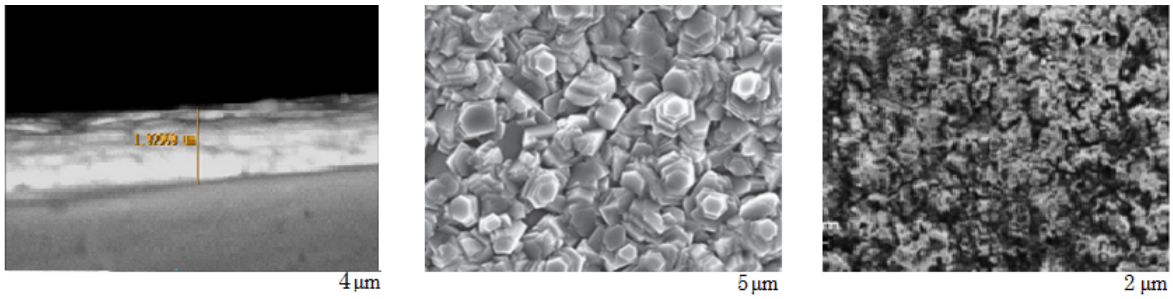

Figure 2.24: SEM micrograph of plated cadmium to iron (left) reprinted with permission from (Oliveira et al., 2010), zinc-nickel (middle) reprinted with permission from (Rashmi et al., 2017), and nickel-cobalt (right) reprinted with permission from (Srivastava et al., 2006).

Diffusion of hydrogen in high strength strands relies on the microstructure of carbon steel wires. Hydrogen, with an atomic radius smaller than iron, easily diffuses into the crystal structure of carbon steel wires, or more specifically the tiny spaces created as a result of microstructure defects like dislocations, inclusions, and grain boundaries. However, solubility of hydrogen atoms in ferrite occurs at a slow rate, while the diffusion of hydrogen atoms from ferrite to pearlite happens at a faster rate because of the crystal structure of iron atoms. The pearlite layers provide a variety of trap sites for diffused hydrogen. Therefore, along with crystal imperfections, cementite/lath interfaces are also strong inhibitors of hydrogen atoms (Bhadeshia, 2016; Souza et al., 2017; Y. Song et al., 2018). As discussed in Section 2.4.3.3, diffusion of hydrogen atoms in the crystal structures of steel eventually causes hydrogen

embrittlement in a high-strength steel wire.

As a second barrier, metallic coating of prestressing wires ensures protection of steel strands in corrosive environments, particularly from hydrogen embrittlement. Moore et al. (1970) reviewed studies that investigated the effectiveness of a coating system in prestressed concrete. According to the authors, galvanized coating in reinforced concrete is a common technique; however, the usefulness of the sacrificial coating in prestressed concrete is questionable because corrosion of zinc occurs at a faster rate in the highly alkaline environment. In addition to that, hydrogen gas produced in the electrochemical process can embrittle the steel substrate. Because of this,

"*the use of galvanized prestressing strands is not common in North America and is currently prohibited by the Federal Highway Administration for use in bridges. The use of galvanizing in prestressing applications and stay cables, however, is very popular in Europe as well as in Japan*" (ACI cmte. 222, 2014).

Therefore, any proposed coating on prestressed strands should be an obstacle to hydrogen diffusion in addition to preventing corrosion. Furthermore, since steel wires are constantly under extreme tension, the coating layer has to withstand the relative elongations due to tensile stresses.

Cadmium plating on steel has been used in the industry for a quite long time, yet its utilization has declined in recent years because of toxicity issues (Das et al., 1997; Bhadeshia, 2016; Rosas et al., 2018). Cadmium, akin to zinc, is used as a sacrificial coating, but in contrast to zinc, cadmium is a hydrogen barrier. Figure 2.24 shows a SEM image of cadmium plated steel as well as zinc-nickel and nickel-cobalt alloy coated surfaces. As shown in this figure, cadmium is deposited on the steel substrate in such dense layers that it makes it difficult for hydrogen atoms to move between cadmium layers. In addition to the toxicity issue, plating cadmium on steel is known as a soft coating, which implies some limitations on using cadmium in prestressed structures. A thin coated layer of cadmium causes a low wear resistance of the coating, and a thick coated layer increases the risk of cracking and delamination of the

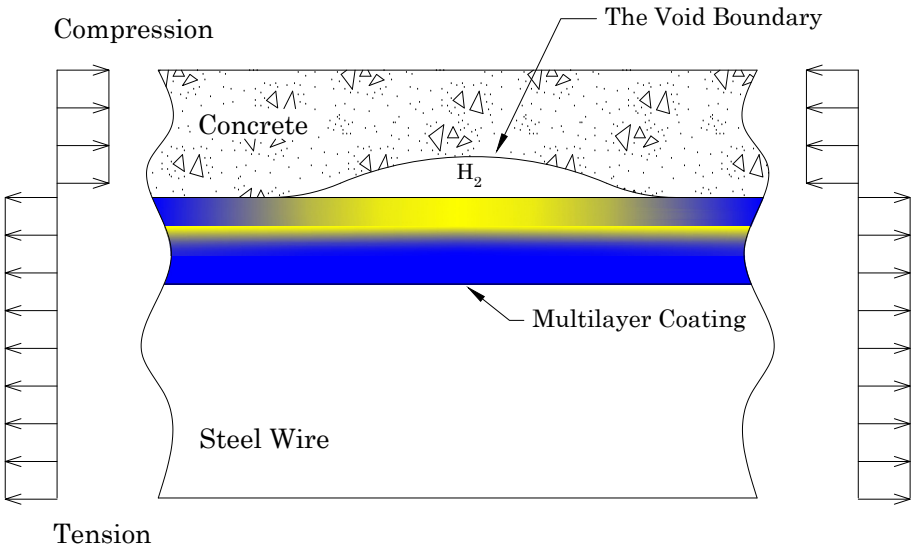

Figure 2.25: Multilayer coating reduces hydrogen permeation in substrate.

protection system. Hillier and Robinson (2004) also reported another drawback of cadmium coating that is the possibility of hydrogen evolution during the electrodeposition process. These hydrogen atoms are not able to escape from the surface and can embrittle the metal substrate.

As an alternative, a zinc-nickel alloy can be plated on a steel wire as a barrier to hydrogen. Nickel atoms form with the face-centered cubic (FCC) structure in a solid state; consequently, hydrogen atoms are able to occupy spaces between nickel atoms. The diffusion of hydrogen in nickel occurs slower than in ferrite because the coated layer provides strong trap sites for hydrogen atoms (Bhadeshia, 2016). Hillier and Robinson (2004) tried 8 μm of zinc plus double layers of 0.5 μm nickel, Zn/Ni 10%, plated on medium carbon steel AISI 4340. The authors reported the embrittlement index is close to 0.0037 if zinc-nickel alloy is plated on AISI 4340, whereas this index is about 0.047 for the baked cadmium sample. Nickel deposited prior to zinc during electroplating can be addressed as an advantage of zinc-nickel alloy compared to galvanized coating since a thin layer of nickel protects the substrate from HE. In addition, if steel wires are coated with a multilayer of nickel as depicted in Figure 2.25, hydrogen atoms diffuse laterally through the interface between plating layers, thus the rate of hydrogen permeation in steel substrate decreases (Rashmi et al., 2017).

Nickel-cobalt based alloy has been used as tubing in deep wells containing aggressive corrosive agents, such as sour gas (Kane & Berkowitz, 1980). Recently, Rosas et al. (2018) proposed nickel-cobalt plating on steel to protect bolts and nuts used in drilling riser connections. The authors concluded that nickel-cobalt alloy is not only a strong barrier to hydrogen, but also the corrosion rate of plated elements is significantly smaller because the alloy is not reactive to the corrosive agents. Nickel-cobalt alloy shows extraordinarily high corrosion resistance, likely because of a combination of nanocrystal structure of nickel (FCC) and cobalt (HCP) (Myung et al., 2003). An advantage of plating this alloy on steel is that if the coated layer was damaged, the rate of oxidation of steel happens at a much slower rate since the alloy does not tend to participate in galvanic reactions (Rosas et al., 2018).

2.7 Loss of Transfer Bond Due to Corrosion Mitigation Techniques

Pedeferri (1996) pointed out that ICCP may reduce the transfer bond between reinforcement and concrete, yet this happens with applying extreme current over an extended period of time (Pedeferri, 1996; Chang, 2002; Ihekwaba et al., 1996). In fact, extreme cathodic protection affects microstructure of cement paste by softening the calcium silicate hydrate (C-S-H) gel and results in the loss of bond between tendons and cementitious material (Chang, 2002). It can be argued that the loss should be significant for a prestressed system since strands are under such utmost tensile stresses that have already caused steel detachment from cementitious material, and the extreme cathodic protection would cause the transfer bond loss. However, this should not raise concerns because, dissimilar to reinforced concrete, interaction between concrete and prestressed strands is not achieved by the adhesion bond. Instead, mechanical interlock (the helical shape), friction (due to a curve shape of tendons), and confinement (known as the Hoyer effect) provide a required bond between steel and concrete (Tepfers, 2000) as shown in Figure 2.26. Overprotection only causes loss of adhesion that is not the case in prestressed structures since

"*slip occurs in the transfer zone due to strain differentials between the steel and concrete, adhesion does not play a role in developing transfer bond*" (Janney, 1954).

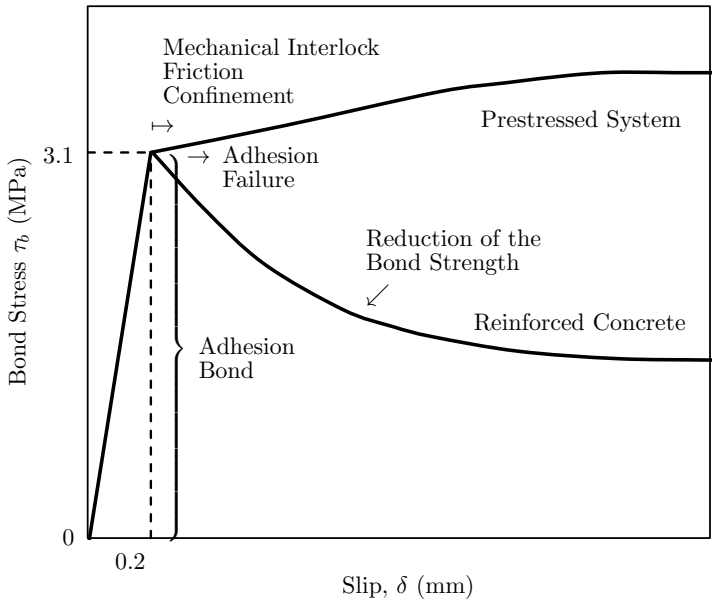

Figure 2.26: Average adhesion bond stress against slip for seven stress-relieved cold-drawn steel wires as well as conventional plain wires, modified from Laco (2018) with permission.

Regarding metallic coatings proposed in this work, neither mechanical interlock, nor confinement conditions would differ from uncoated strands embedded in concrete; however, the bond between high strength steel and cementitious material due to friction will be influenced by the wear resistance of wires contacting the concrete surface. Abrasive wear resistance of a metal can be estimated by Vickers hardness number, H_v, since the specific wear rate of materials generally decreases linearly with increasing the hardness (Landolt & Mischler, 2011). The Vickers hardness of seven stress-relieved cold-drawn steel wires is in the range of 4.32 to 5.83 GPa (Singh, 2000) indicating a relatively low wear rate and good wear resistance compared to mild steel. Cadmium is referred to as solid lubricant (Jovanović et al., 2018), and it may not be applied to prestressed members because the coating layer reduces the friction between strands and concrete. Contrary to cadmium, the Vickers hardness number of zinc alloyed with 10% nickel is close to the hardness of mild steel (Ganesan et al., 2007), and the Vickers hardness of nickel-cobalt alloy is in the range of 4.72 to 5.98 GPa (Hagarova et al., 2015) which is relatively more than the hardness of stress-relieved cold-drawn steel wire.

3. PREPARATION AND ELECTROPLATING ON ASTM A 416 STEEL WIRES

3.1 Introduction

As discussed in Chapter 2, metallic coating of prestressing wires provides a layer of hydrogen barrier and reduces risks associated with brittle failures. Certain conditions ought to be imposed on the system so that a brittle crack occurs on steel wires. The right temperature, defects in crystal structure of steel wires, high net section stress, and the presence of atomic hydrogen exemplify those conditions that are quite expected for prestressing strands. Therefore, providing a barrier to hydrogen atoms is a plausible solution to avoid that kind of failure in high-strength steel wires.

3.2 ASTM A 416 Prestressing Wires

A relatively high tensile strength of the steel makes prestressing wires superior to other types of steel used in concrete. This is a result of the chemical constituent of the metal and the manufacturing process including heat treatment and cold working. ACI 222.2R-01 provided a comprehensive report on the steps that have to be taken to produce high-strength steel strands known as ASTM A 416, but a brief review of the process required to prepare this type of prestressing wires is also given in this chapter.

High carbon steel strands that are typically used in civil engineering applications are made of 6 wires helically wound around a straight wire (Figure 3.1). These strands ought to bear up loads in a range of 55 to 65% of their ultimate tensile strength during their service life. Since the wires are under constant applied stress, the strength of these wires plays a significant role in the durability of the whole system. In order to achieve such a strength, steel producers use continuous-cast steel composed of carbon (four times greater than what is used in common carbon steel) and small amounts of manganese supplemented with chromium and vanadium. After the phase transformation reaches completion, the wire mil should cool down rapidly. Thus, a series of fans provides fresh air passing over the roll of metal chains

Figure 3.1: Comparison between intact and corroded ASTM A 416 strands. The corroded steel strand was left outside for more than 3 years and were exposed to air and moisture.

during the Stelmor cooling process and ensuring the formation of the very fine pearlite layers. These alternate layers of ferrite and cementite provide proper strength to the steel wire. The next step is the surface treatment that ought to be done by immersing the coils in 20% hydrochloric or sulfuric acid for a short duration and applying a zinc-phosphate layer to the metal chains. The coating also improves the bonding of the lubricants during the wire drawing process. Cold working reduces the cross-sectional area of the steel up to 85% and enhances the tensile strength of the wires even more. At the final stage, the metal chains are exposed to hot air so that the temperature of coils reaches to 800°C. Note that the heat treatment results in stress relieving leading to improved mechanical properties of the steel wires.

3.3 Electrodeposition

The experimental study began with the electrodeposition of nickel, cobalt, and zinc on a low-relaxation, grade 270, seven-wire steel strand. Electroplating of the alloys on steel is not a successful process if a strong bond between coating layer and substrate was not achieved. The adhesion between the plated film and steel substrate comes from a variety of reasons such as the condition of interface region, mechanical properties and atomic bonding between two metals, thickness, porosity, and ductility of coating layers (Dini, 1993). In the case of high-strength steel, an activation treatment prior to electroplating is essential to maintain

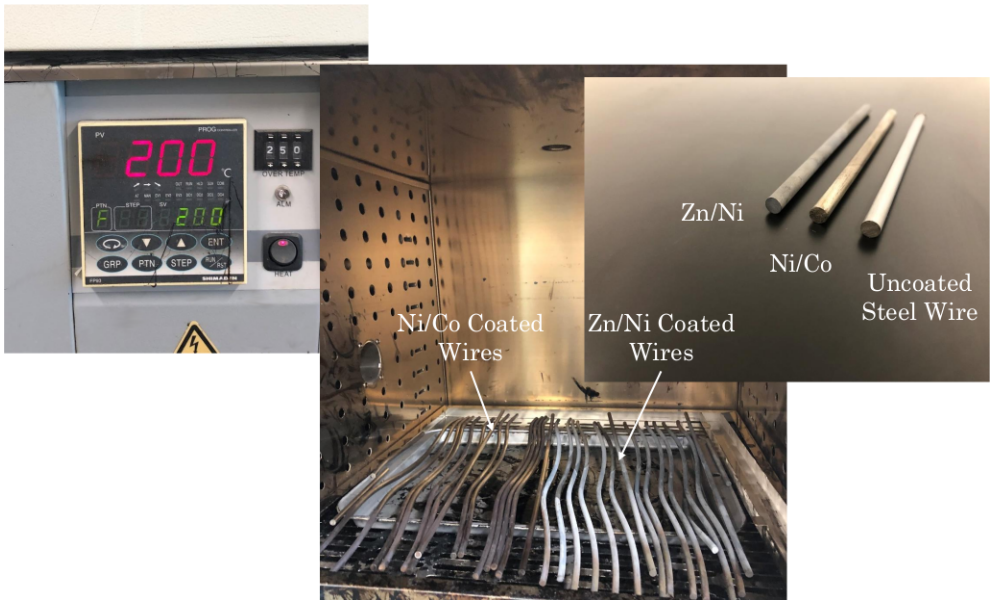

Figure 3.2: Baking nickel-cobalt and zinc-nickel coated wires for twenty-seven hours at 200°C.

sufficient adhesion to substrate. Graham (1971) suggested a series of surface activators, including anodic cleaning and acidic treatment, before plating on high carbon and low alloy steel to improve adherence of coating layers.

Note that the hydrogen atoms produced during the electroplating process eventually cause brittle failure in the future. In addition to the plating process, Dini (1993) addressed other sources of hydrogen atoms such as activation treatments (pickling), cathodic cleaning, and solvent cleaning. The atomic hydrogen has the potential to reduce the ductility of steel and results in hydrogen embrittlement as discussed in Chapter 2. Dini (1993) recommended an effusion process for at least twenty-four hours of heat treatment, 200°C to 230°C prior to coating steel that is completed during metallurgical work of the final preparation of high-strength strands. The author also suggested a baking process of electroplated high-strength steel for at least twenty-two hours in a chamber within a range of 190°C to 220°C. The process has to take place at most 3 hours after electrodeposition of metallic coatings on steel substrate according to ASTM B850 in order to reduce the risks associated to hydrogen embrittlement in prestressed wires. Note that the heat treatment in this range does not alter the material properties of high-strength steel strands. The baking process has been similarly

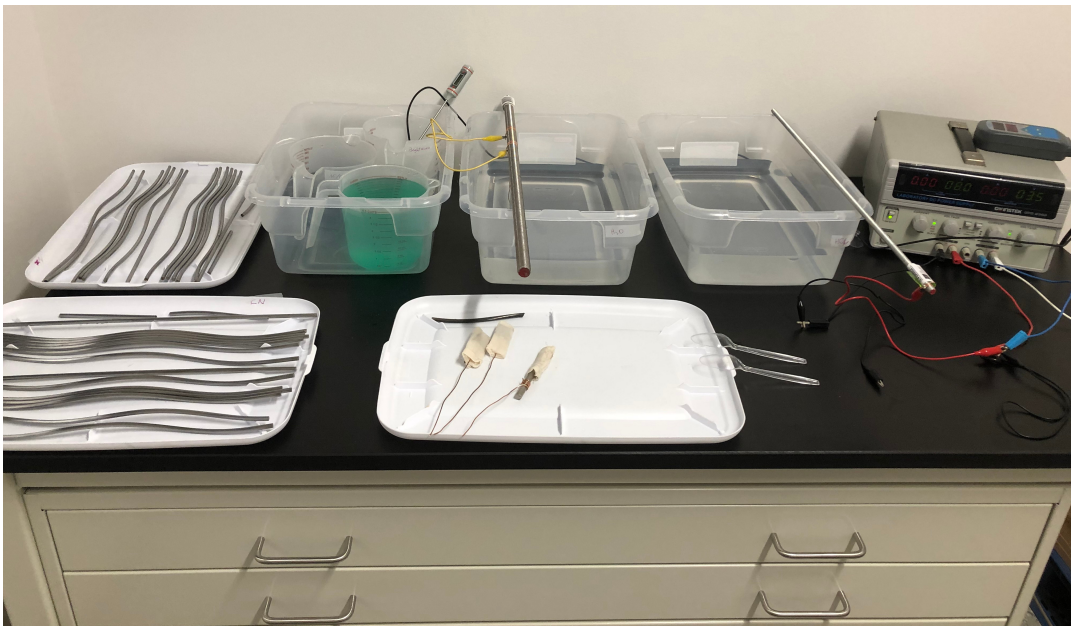

Figure 3.3: Apparatuses and materials used for metallic coating on steel wires.

recommended by other researchers (Bhadeshia, 2016; Hillier & Robinson, 2004). Figure 3.2 shows all the coated wires during and after finishing the heat treatment.

3.4 Electroplating Process

In this study, a multilayer coating was considered in order to produce a proper barrier to hydrogen diffusion. Hence, a thin layer of zinc-nickel conforming to ASTM B841 was plated on half of the steel wires, then the same bath was used to coat the finishing layer. For the rest of the samples, a nickel-cobalt layer complaint with ASTM B994 was coated in two layers. Figure 3.3 designates the electroplating equipment used for coating of the proposed alloys on high-strength steel wires. A pH meter tester was used to assess the ambient conditions of electroplating solutions while a power supply and thermometers helped to carefully control the electrodeposition process.

The flowchart in Figure 3.4 demonstrates the process required for electroplating deposition to steel wires. Prior to the electroplating process, any contaminants and impurities were removed from the steel surface. This treatment included sanding the residues off of the steel surface in addition to anodic electrolytic cleaning to eliminate any stains, scales, and

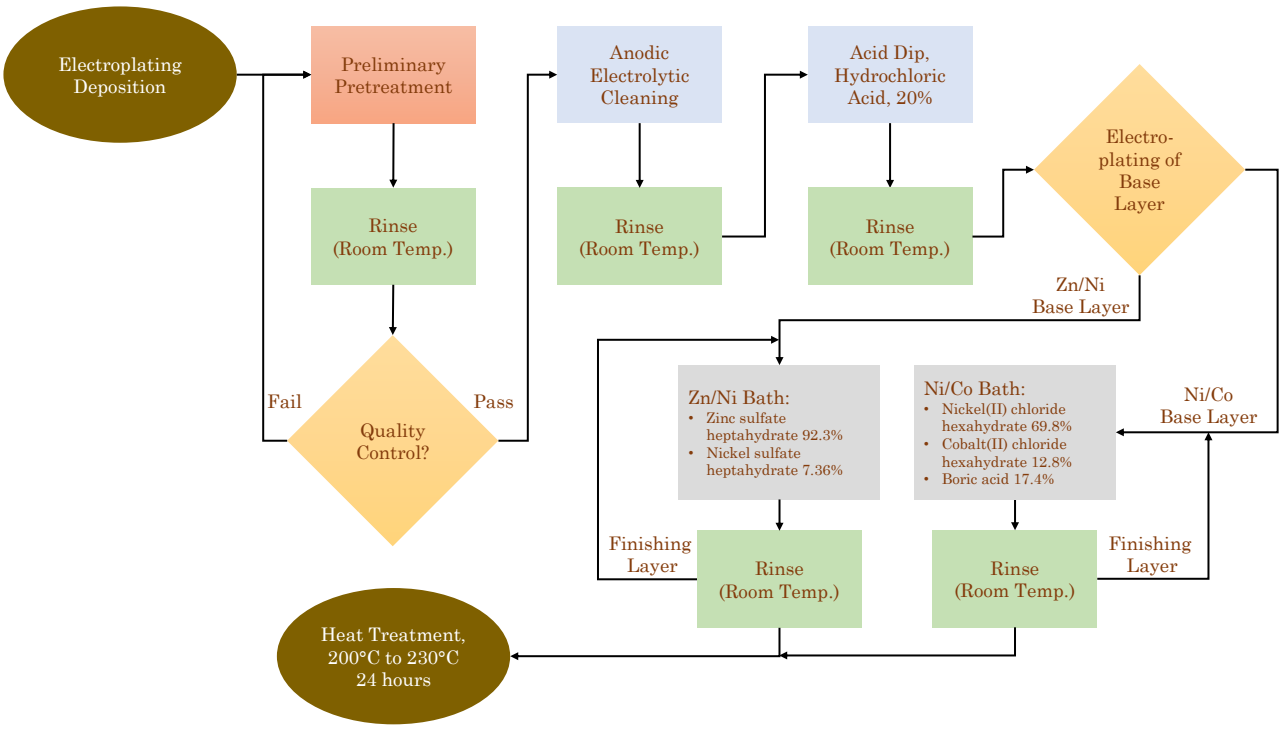

Figure 3.4: Process required for electroplating on high-carbon and low-alloy steel.

corrosion products from the steel wire. Note that a trace of corrosion on steel wires was found at the contact areas of half of the samples after unlaying strands for the purpose of electroplating. Although these strands were never placed under tension, uniform corrosion damage was observed at the crevice areas.

After preliminary pretreatment and anodic electrolytic cleaning, samples were rinsed with deionized water several times at room-temperature. Then, samples were immersed in a 20% hydrochloric acid bath for 20 to 30 seconds and immediately rinsed out again with deionized water at room-temperature. Finally, samples were transferred to the electroplating bath. The surface treatment selected herein was indeed a more aggressive approach that was proposed by Graham (1971). In fact, the author recommended softer treatments for avoidance of hydrogen embrittlement since a dip in strong hydrochloric acid contributes to the hardening of steel wires. Hence, the use of a softer treatment is suggested in practice, while an aggressive approach was considered for this experiment.

The bath compositions for both zinc-nickel and nickel-cobalt coatings are given in Table

Table 3.1: Composition of the plating baths.

Bath Composition	Concentration	Temperature	Time	pH	Current Density
	(g/l)	(°C)	(min)		(mA/cm^2)
Zn(92-89%)Ni(8-11%)					
$ZnSo_4.7H_2O$	264.5	23±2	32	5.5	10.5
$NiSo_4.7H_2O$	21.0				
Ni(60-50%)Co(40-50%)					
$NiCL_2.6H_2O$	102.7	21±1	15	3	7.9
$CoCL_2.6H_2O$	18.8				
H_3BO_3	25.6				

3.1. The deposition bath of zinc-nickel alloy consisted of zinc sulfate heptahydrate and nickel sulfate heptahydrate. Similar to the experiment performed by Hillier and Robinson (2004), a small amount of commercial sulfate-free liquid dishwashing detergent was added to the bath composition to reduce the risk of hydrogen production that causes coating defects. Titanium mesh was used as the anode during the plating process of zinc-nickel to steel wires. The temperature of the bath was 23±2°C, and the pH was maintained constant at 5.5. In addition, the deposition process was conducted for the base layer at a current density of 10.5 mA/cm^2 and the finishing layer at a current density 5.26 mA/cm^2. The electrodeposition of zinc-nickel alloy to steel wires took about 20 minutes on average for each sample for the primary coating and 10 minutes for the finishing layer.

The bath composition of nickel-cobalt alloy contained nickel (II) chloride hexahydrate, cobalt (II) chloride hexahydrate, and a small amount of boric acid. A nickel anode was used during electrodeposition because of higher deposition of nickel in the second bath. The temperature of the bath was reduced to 22±1°C, and the pH was held at 3. In order to ensure that the electrodeposited layer was not burned, the current density was reduced to 7.9 to 8.4 mA/cm^2 for the base layer and 3.15 mA/cm^2 for the finishing layer. The primary coating was completed in 10 minutes, and the finishing layer took about 5 minutes.

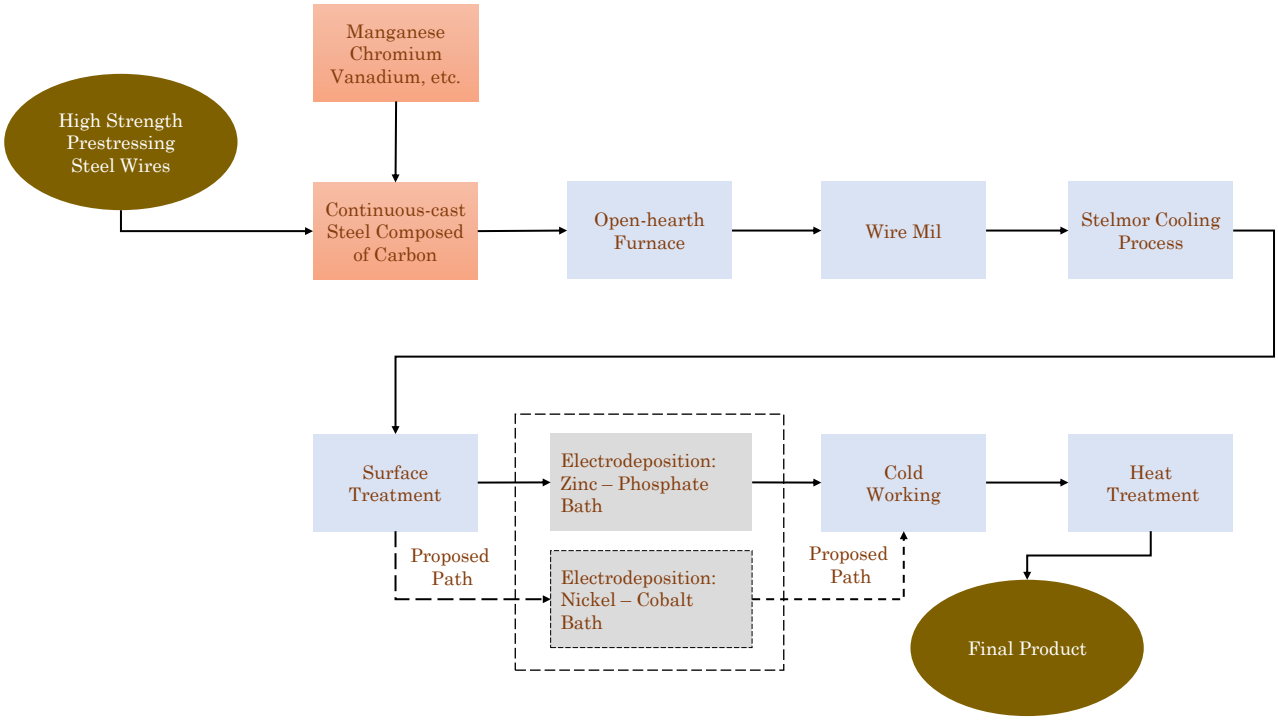

Figure 3.5: Process required in making high-strength steel wires, ASTM A 416, adapted from (ACI cmte. 222, 2014).

Since a baking process was needed in order to remove the absorbed hydrogen during the plating process, the samples were transferred to a chamber with a temperature of 200°C for 27 hours. Figure 3.2 demonstrates a 127 millimeters [5 inches] long uncoated sample as well as 127 millimeters [5 inches] wires coated with nickel-cobalt and zinc-nickel alloys after finishing the electrodeposition and heat treatment.

3.5 Further Discussion and Closing Remarks

Metallic coating of high-strength steel is already performed during steel production. Although galvanized coating of prestressing strands for use in non-building structures is prohibited by the Federal Highway Administration, it is still acceptable to alloy zinc with phosphate. Zinc-phosphate alloys are applied to the steel wires mainly for surface treatment purposes during cold working, yet the coating is able to improve the corrosion resistance of the steel wires. Zinc is inexpensive and conveniently available that makes it reliable for industrial applications; however, neither zinc nor phosphate is a hydrogen barrier.

Nickel is a barrier against hydrogen diffusion, and alloying it with zinc provides a reliable protection system. Similarly, nickel-cobalt alloy protects steel substrate from hydrogen embrittlement and improves corrosion resistance of the steel wires. In order to enhance the properties of ASTM A 416 steel, the current procedure shown in Figure 3.5 can be modified so that nickel plating is done prior to electrodeposition of the current coating. Alternatively, the electrodeposition process can be completed in a nickel-cobalt bath instead of zinc-phosphate to reduce the risks associated with hydrogen diffusion.

4. CYCLIC POTENTIODYNAMIC POLARIZATION

4.1 Introduction

Potentiodynamic polarization measurement is a common procedure that is widely used to identify the electrochemical properties of metals or alloys in an aqueous solution. The method consists of recording potential variations of a working electrode (specimen) and a counter electrode (platinum mesh) with the aid of a Potentiostat. It is common to study the corrosion behavior of reinforcement in concrete in an aqueous alkaline solution that approximates the concrete environment. Trejo et al. (2009) conducted an experiment using Cyclic Potentiodynamic Polarization (CPP) to evaluate the susceptibility of high-strength steel ASTM A 416 to localized corrosion, such as pitting corrosion. The authors modeled the concrete pore environment with a solution consisting of hydroxides. The test was initially conducted in a solution with no chloride ions, and later repeated in a similar solution but with a chloride concentration of 0.06 and 1.8%. Moser (2011) used a similar procedure to investigate the electrochemical properties of ASTM A 416 steel wire. The concrete pore environment was modeled with a solution composed of potassium hydroxide, gypsum, sodium hydroxide, calcium hydroxide, and sodium chloride. The tests were completed in a solution with a chloride concentration varied from 0 M to 1 M. Although the simulated pore solution is a suitable model of the concrete environment, both studies agreed that the result of the experiments should not be expected to simulate the real conditions of the prestressed concrete environment.

In 1982, the Deutsches Institut für Bautechnik (DIBt) introduced a new approach to investigate the resistance of cold-drawn high-strength steel wires to hydrogen embrittlement. After conducting a chemical analysis of the samples taken from embedded service ducts in prestressed structures, the DIBt concluded an aqueous solution of potassium chloride, potassium sulfate, and potassium thiocyanate simulates the service environment of prestressed

steel strands. Prior to the DIBt approach, the International Federation for Structural Concrete (FIP) recommended a radical aqueous solution of 20% ammonium thiocyanate to model a corrosive environment for ASTM A 416 steel wires.

In this study, CPP was used to identify the susceptibility of uncoated stress-relieved, cold-drawn high-strength steel wires to localized corrosion, and compared the results with zinc-nickel, and nickel-cobalt coated wires. It was decided to perform the potentiodynamic polarization test with the solution proposed by the DIBt in addition to the simulated pore solution used by Trejo et al. (2009) since the former solution simulates a realistic corrosive environment. Then, the test was repeated once more in an environment recommended by the FIP in order to study the change of electrochemical properties of ASTM A 416 steel wires in an aggressive environment.

4.2 Experimental Procedure

The preparation of samples for potentiodynamic polarization measurements included the use of a portable electric saw to cut as-received ASTM A 416 steel strands in 127 millimeters [5 inches] length wires. Then, P120 and P220 sandpaper sheets were used to remove scales and every possible trace of corrosion product from the surface of the half of the samples. These wires were either coated with zinc-nickel or coated with nickel-cobalt, or used as uncoated wires during the experiments. The other half of the samples were kept in their as-received condition during the tests. In order to restrict the exposure area, a polyolefin shrink tube with a 6.4 mm [0.25 in] in diameter was used to protect the entirety of the samples, except an exposed 303 mm^2 [0.47 in^2] surface. In addition to heat-shrink tubing, polytetrafluoroethylene coatings were also applied to not only form an air-tight seal but reduce crevice volumes between the mask and sample surface. The ends of the steel wires were left out with no protection. This was the area that was used for electrical connections.

CPP was conducted for as-received and uncoated wires as well as samples with zinc-nickel and nickel-cobalt alloy coatings. Figure 4.1 shows the typical corrosion cell and apparatus required for cyclic polarization technique. As discussed, the simulated pore solution was used

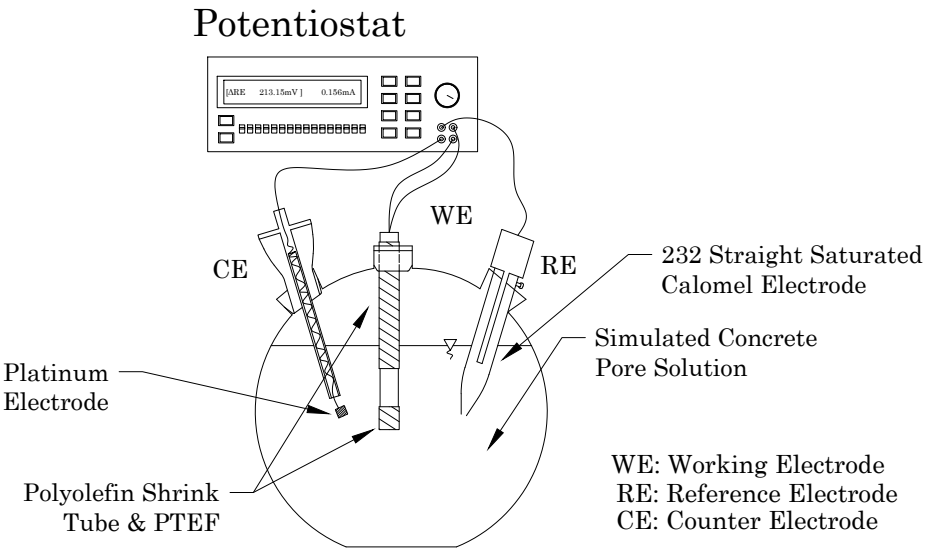

Figure 4.1: Schematic view of corrosion cell during CPP operation.

to simulate the concrete environment. Table 4.1 shows the components of the simulated pore solution in addition to DIBt and FIP.78 solutions. The volume of the solution used in CPP was 1.5 liters of the aqueous solution that gives a ratio of solution mass-to-surface area 4.64 ml/mm^2. Samples were cleaned with acetone and further rinsed with deionized water before they were transferred and installed in the corrosion cell. A potentiodynamic polarization measurement was conducted at room temperature, but the pH of the solution changed depending on the environment simulated during the experiments. The average pH of simulated pore solution was 11.5, corrosive environment was 6.5, and acidic solution was 4. As shown in Figure 4.1, a three-electrode cell was used to identify the electrochemical parameters of ASTM A 416 steel wires. A platinum electrode was used as a counter electrode, and a single salt bridge calomel reference electrode 232 was employed as a reference electrode. In order to measure the flowing current in the cell and the electrodes, it was decided to use a Solartron 1287A Potentiostat electrochemical interface with an IEEE-488 bus (GPIB cable), which provided a communication between the Potentiostat and computer. A python script (Appendix A.3) simultaneously recorded the data measurements in a CSV file that was used for further analysis.

Prior to beginning cyclic voltammetry, the working electrode was immersed in the solution

Table 4.1: Test environment to identify the susceptibility of steel wires to corrosion.

Solution	Compositions	pH	Temperature
Pore Simulated	Potassium Hydroxide (KOH, 17.9 g/l) Sodium Hydroxide (NaOH, 5.24 g/l) Calcium Hydroxide ($Ca(OH)_2$, 2.40 g/l) Gypsum ($CaSO_2.2H_2O$, 0.55 g/l)	11.5 – 13	21±1°C
Corrosive (DIBt)	Potassium Chloride (KCl, 0.014 M) Potassium Sulfate (K_2SO_4, 0.052 M) Potassium Thiocyanate (KSCN, 0.017 M)	6 – 8	21±1°C
Acidic (FIP.78)	Ammonium Thiocyanate (NH_4SCN, 20%)	3.8 – 4.3	15±3°C 17±1°C

for one and half hours, and the stabilized open circuit potential was meanwhile recorded. After the passivation process was complete, the counter electrode and calomel reference electrode were connected to the Potentiostat, and the flowing current and potential variations in the cell were observed for almost three hours (Figure 4.1). The applied voltage ranged between -1200 to +1000 mV with scan rate of 0.167 mV/s for all samples, except zinc-nickel coated samples which ranged from -1300 to 800 mV. The lower limit was reduced during potentiodynamic polarization measurements for zinc-nickel coated samples because the corrosion potential was actually expected to occur around -1100 mV vs. SCE, as reported by Popov (2015).

4.3 Experimental Results

Figure 4.2 demonstrates the open circuit potential of all the specimens in a simulated pore solution. It took about an hour for the voltages of the uncoated samples to stabilize, but the stabilization for coated samples reached faster at about 5 to 10 minutes. The potential instability recorded for uncoated wire is perhaps a consequence of the surface roughness of the specimen during the sample preparation. The open circuit potential registered for zinc-nickel specimens was more negative compared to other samples, and it was more positive for nickel-cobalt and zinc-phosphate coatings as compared to the one measured for uncoated samples. The open circuit potential was -173 mV vs. SCE for nickel-cobalt wire, while it was

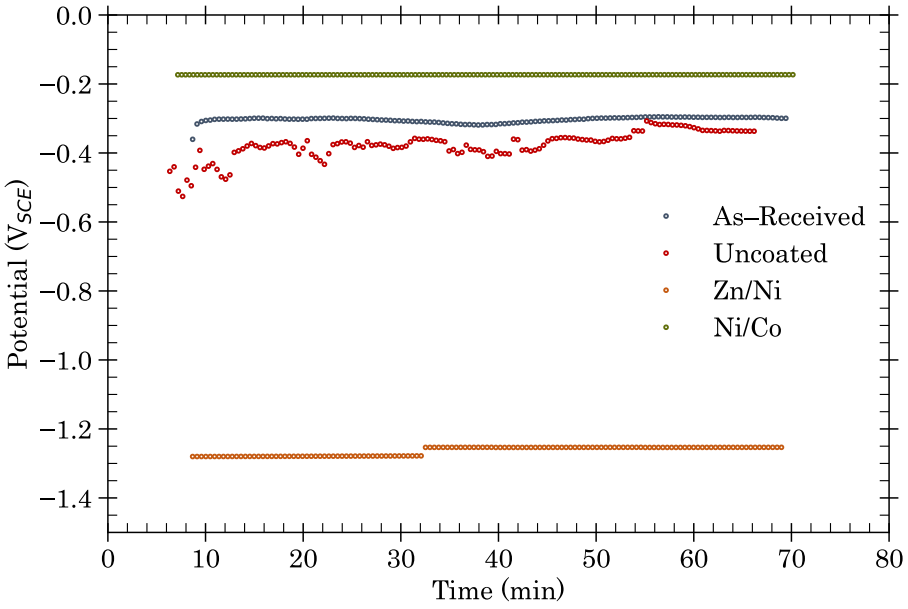

Figure 4.2: Open circuit potential for both coated and uncoated ASTM A 416 wires.

obtained at -1250 mV vs. SCE for zinc-nickel sample. As shown in Figure 4.2, this potential was -298 mV vs. SCE for as-received specimens and -337 mV vs. SCE for uncoated wires.

Figure 4.3 shows cyclic voltammogram for as-received wires coated with zinc-phosphate in dissimilar environments: a pore-simulate solution with pH 11.8, a corrosive environment proposed by DIBt with pH 7.4, and an acidic environment with pH 3.8. The current density recorded during the potentiodynamic polarization test significantly increased as the environment became more aggressive. The polarization voltage also became more negative compared to measurements logged in the simulated pore environment. The corrosion current density (i_{corr}) and the corrosion potential (V_{corr}) were calculated as 4.67 μA/cm^2 and -305 mV vs. SCE for the sample in alkaline aqueous solution, while the current density increased to 206.6 μA/cm^2 and the voltage reduced to -657 mV vs. SCE for the wire exposed to aggressive solution. Therefore, it can be concluded that the corrosion rate of as-received specimens is higher when the ambient pH drops. A passivation phase observed for the sample placed in a simulated pore environment ranged from approximately -100 to 600 mV vs. SCE.

A comparison demonstrated in Figure 4.4 was made between kinetic behavior of high-strength steel wires with different coatings. As shown in this figure, the nickel-cobalt coated

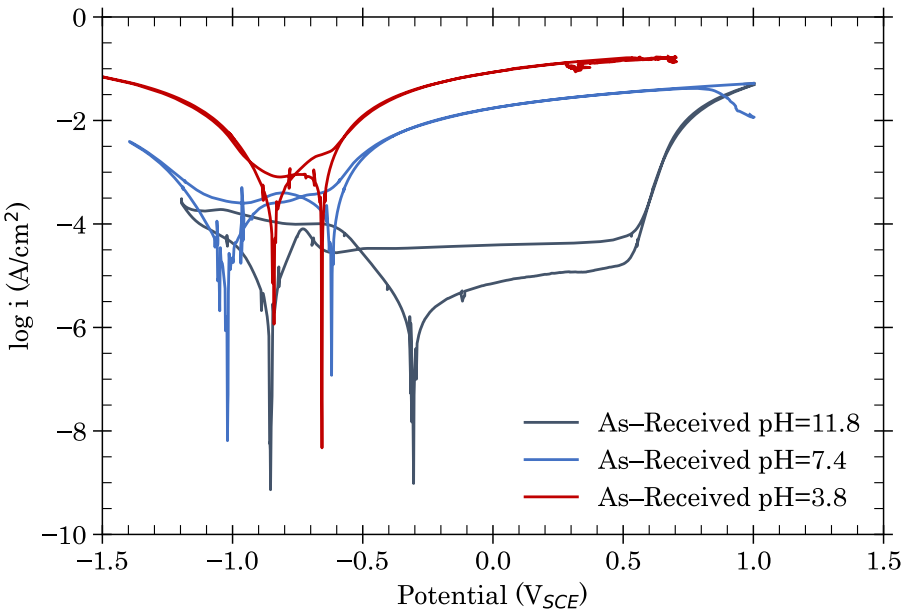

Figure 4.3: Cyclic voltammogram for as-received wires in concrete simulated, corrosive, and acidic environments.

sample exhibited nearly the same properties as the wire coated with zinc-phosphate. The corrosion current density and the corrosion potential observed for the nickel-cobalt sample were 1.85 μA/cm^2 and -206 mV vs. SCE, which is close to the corrosion current density and the corrosion potential obtained for the as-received wire. Current density for the zinc-nickel sample, where it tested in alkaline solution, was much higher than two other samples. The corrosion current density was estimated at 57 μA/cm^2, and the corrosion potential occurred at -1137 mV vs. SCE for zinc-nickel coated wire. It is evident that the corrosion rate of the zinc-nickel specimen was higher in a simulated pore solution compared to nickel-cobalt and zinc-phosphate samples. The polarization voltages recorded for the zinc-nickel wire were more negative than potentials logged for as-received specimens.

Cyclic voltammogram in Figure 4.4 also provides information regarding the break of the passive layer and pitting initiation on coatings. The pitting potential was measured at approximately 550 mV vs. SCE for the as-received wire, while it was estimated at 500 mV vs. SCE for the nickel-cobalt sample. Note that multiple oxidation states of the species were observed for the latter sample immersed in the concrete simulated environment. Cyclic

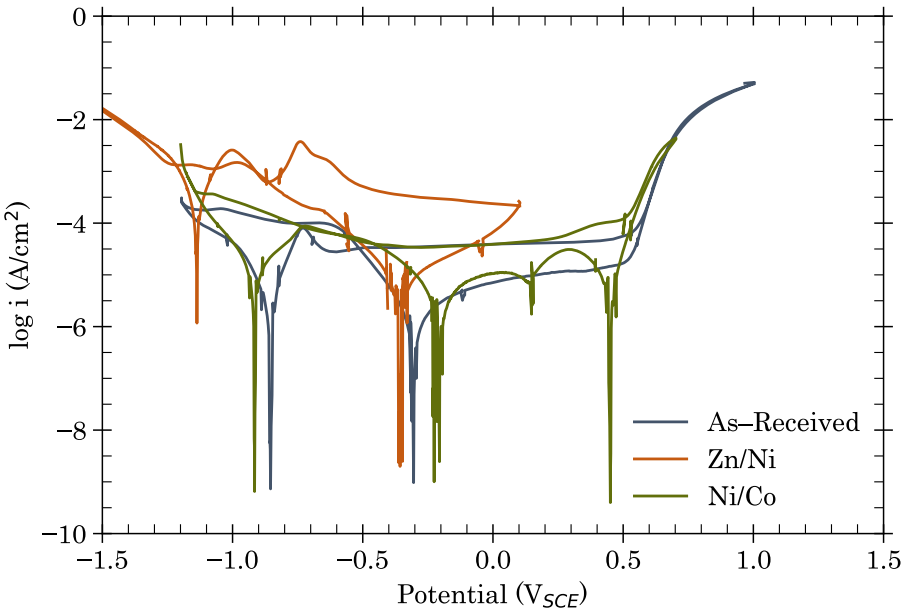

Figure 4.4: Cyclic voltammogram for ASTM A 416 wires with dissimilar coatings in simulated pore solution.

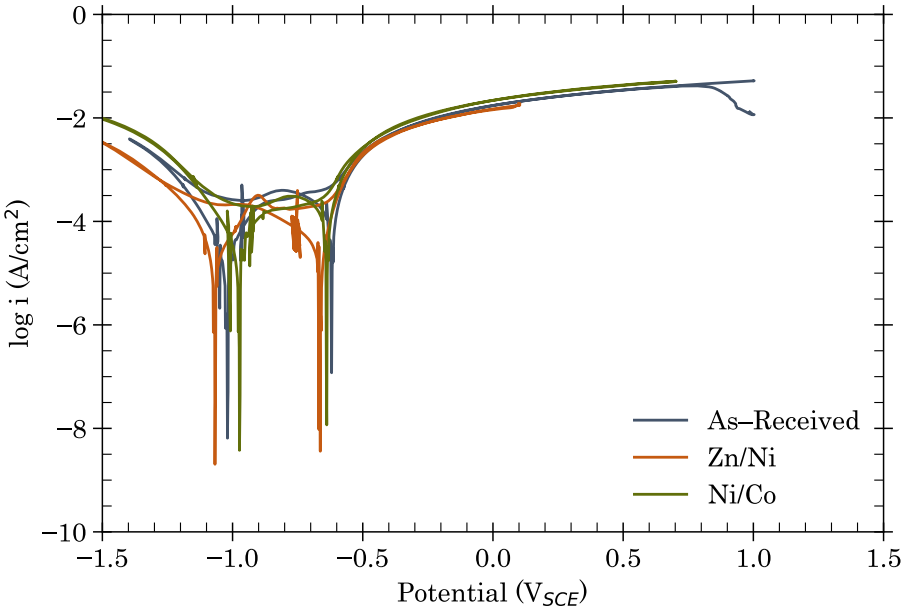

Figure 4.5: Cyclic voltammogram for ASTM A 416 wires with dissimilar coatings in a corrosive solution.

Table 4.2: Corrosion properties of metallic coated and uncoated ASTM A 416 steel wires.

Sample	Solution	R_p [a]	i_{corr}	V_{corr}	CR [b]
		kΩ cm^2	μA/cm^2	V vs. SCE	mm/y
As-Received	Simulated Pore	79.8	4.67	-0.305	0.051
As-Received	DIBt	5.19	24.1	-0.620	0.264
As-Received	FIP.78	0.47	206.6	-0.657	2.254
Uncoated	DIBt	4.69	21.3	-0.648	0.232
Ni/Co	DIBt	9.34	19.0	-0.638	0.205
Zn/Ni	DIBt	1.35	14.9	-1.067	0.211
Ni/Co	Simulated Pore	78.5	1.85	-0.206	0.036
Zn/Ni	Simulated Pore	0.45	57.0	-1.137	0.830

[a] Polarization Resistance
[b] Corrosion Rate

voltammogram shown in Figure 4.5 demonstrates the kinetic behavior of high-strength steel wires with different coatings in a corrosive environment. The solution employed in the test was the one proposed by the DIBt (Table 4.1), and pH was maintained between 6 to 8 throughout the cyclic voltammetry test. All samples exhibited more or less similar properties where they were immersed and tested in this environment. Zinc-nickel coated samples performed better than other specimens when pH dropped lower than 8. The corrosion current density and the corrosion potential obtained for the zinc-nickel sample were 14.9 μA/cm^2 and -1067 mV vs. SCE, respectively. Therefore, the corrosion rate of the zinc-nickel coated specimen was slightly lower than the rate of degradation of the zinc-phosphate coated wire. In addition, the corrosion current density recorded for the nickel-cobalt sample was also slightly lower than the as-received wire, which indicates that the corrosion rate of the specimen was also lower than the one computed for the as-received wire. The value measured for i_{corr} was 19 μA/cm^2 for the nickel-cobalt coated sample compared to 24.1 μA/cm^2 for the zinc-phosphate sample.

Nickel-cobalt alloy coating showed a resistance to corrosion similar or slightly superior to as-received high-strength steel wires commercially available today. Corrosion properties of all the coatings tested during the potentiodynamic polarization examination are reported

in Table 4.2. From the data listed in this table, it is evident that corrosion properties of samples differ considerably when the environment becomes more aggressive. For example, the electric potential for nickel-cobalt and zinc-phosphate coatings shifted to more negative voltages from alkaline to acidic environments, while the opposite occurred for zinc-nickel where the corrosion potential moved from -1137 mV to -1067 mV. Lower values reported for the corrosion current density where nickel-cobalt coated samples and as-received wires tested in simulated pore solution, yet the corrosion rate significantly increased for zinc-nickel samples tested in the same environment. It is also clear that the corrosion current density recorded for as-received wires substantially increased from alkaline environment to acidic environment from 4.67 to 206.7 μA/cm^2. The corrosion current density was lower for both proposed coatings compared to the current density obtained for uncoated and as-received wires in the corrosive solution. This indicates that resistance of the proposed coatings in a corrosive environment is superior to currently available ASTM A 416 wires.

Polarization resistance reported in Table 4.2 was computed from an impedance analysis that is covered in Chapter 5 in detail. However, the results agreed with the resistance obtained from the Stern-Geary equation

$$i_{\text{corr}} = \frac{\beta_c \beta_a}{2.3\,(\beta_c + \beta_a)} \frac{1}{R_p}\ . \tag{4.1}$$

where β_c and β_a are the cathodic and the anodic Tafel slopes, respectively. In general, polarization resistance of nickel-cobalt alloy was close to that of zinc-phosphate, while it was remarkably higher than the polarization resistance reported for zinc-nickel alloy. Corrosion rates of steel wires with and without coatings are also reported in Table 4.2. For a better comparison between the rate of degradation of the proposed coatings and as-received wire, the corrosion rates are represented in a bar diagram shown in Figure 4.6. The corrosion rate of nickel-cobalt alloy was slightly lower than that of the as-received coating system. The rate was considerably low for both nickel-cobalt and zinc-phosphate coatings in a concrete

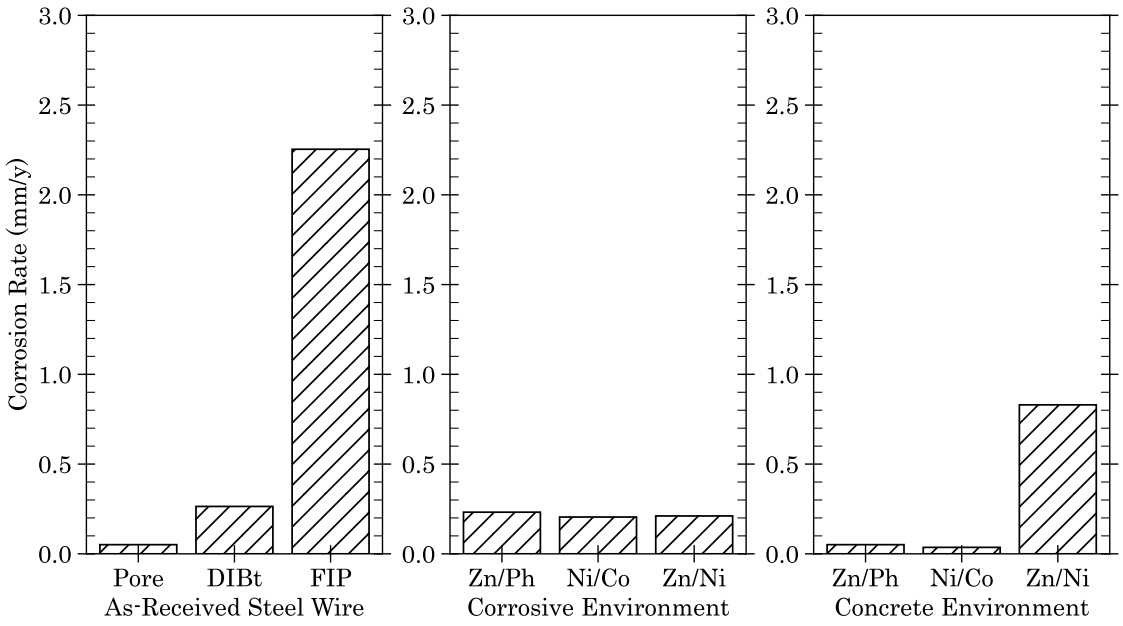

Figure 4.6: Corrosion rate computed for ASTM A 416 wires with and without metallic coatings; in alkaline (simulated pore solution), corrosive (DIBt solution), and acidic environments (FIP solution).

simulated environment. The corrosion rate of zinc-nickel alloy was high in an alkaline solution, and it decreased as the ambient pH dropped to a lower rate. This indicates that zinc-nickel coating provides a decent protection against corrosion in a corrosive environment rather than in an alkaline. Corrosion rate of as-received wire was low in a simulated pore solution and reached to 0.26 mm/y in a corrosive condition. The rate was incredibly high, 2.25 mm/y, in an acidic environment.

The severity of corrosion attack on high-strength steel wires is portrayed in Figure 4.7. A significant damage was found on as-received wires tested in the aggressive environment proposed by FIP. As shown, the exposed surface became powdery and was delaminated to some extent. Uniform corrosion was observed on specimens which were examined in the environment recommended by DIBt, although the severity of damage was modest. Corrosion pits were found on the surface of all samples including nickel-cobalt and zinc-nickel coatings. There was a greater distribution of the pits on the zinc-nickel specimen immersed in the simulated pore solution. This is demonstrated in Figure 4.7j and Figure 4.7k.

(a) As-Received ASTM A 416 wire tested in an acidic environment (pH=3.8).

(b) As-Received ASTM A 416 wire tested in an acidic environment (pH=3.8).

(c) Uncoated ASTM A 416 wire tested in an acidic environment (pH=3.8).

(d) As-Received ASTM A 416 wire tested in a corrosive environment (pH=7).

Figure 4.7: Samples after completion of CPP.

(e) Uncoated ASTM A 416 wire tested in a corrosive environment (pH=7).

(f) As-Received ASTM A 416 wire—abrasive wear damage.

(g) As-Received ASTM A 416 wire—scale and injurious defect.

(h) Ni/Co coated wire tested in a corrosive environment (pH=7).

Figure 4.7: Samples after completion of CPP, continued.

(i) Ni/Co coated wire tested in a simulated pore environment (pH=12).

(j) Zn/Ni coated wire tested in a corrosive environment (pH=7).

(k) Zn/Ni coated wire tested in a simulated pore environment (pH=12).

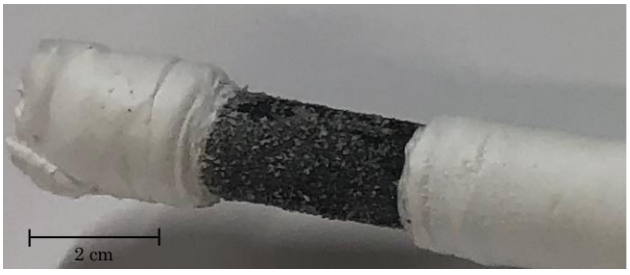

(l) Zn/Ni coated wire placed in a simulated pore solution for two days then exposed to air.

Figure 4.7: Samples after completion of CPP, continued.

4.4 Further Discussion and Closing Remarks

The kinetic properties of zinc-phosphate, nickel-cobalt, and zinc-nickel plated on ASTM A 416 steel wires were covered in this chapter. It was found that the current density measured for the specimens increased while the pH of the environment decreased, as anticipated. The corrosion rate calculated for the specimen coated with nickel-cobalt alloy was found to be similar to the one computed for the as-received wire, whereas the pitting potential recorded for the alloy occurred at a lower voltage compared to the one measured for the specimen coated with zinc-phosphate wire. It was also concluded that the corrosion rate of the zinc-nickel alloy is remarkably higher when the specimen was tested in a simulated concrete environment, while the kinetic performance of the coating improved in the aqueous solution recommended by DIBt.

5. ELECTROCHEMICAL IMPEDANCE SPECTROSCOPY

5.1 Introduction

Impedance analysis is a powerful approach to determine the polarization resistance of a working electrode that is then used to calculate the corrosion rate of the sample. Electrochemical Impedance Spectroscopy (EIS) is also common to study the barrier coating performance and to identify the durability of the passivation layer in metals. According to Popov (2015), Dolin and Ershler (1940) originally introduced EIS for the purpose of corrosion studies, yet Grahame (1952) and later Randles and Somerton (1997) advanced the impedance analysis to what can be recognized today.

Impedance Spectroscopy can be performed in a short period of time, and it is usually non-destructive. However, certain conditions have to be taken into consideration in order to guarantee reliable data; e.g., EIS should not be performed for non-stable systems. During the test operation, a low range alternating voltage (typically 20 mV_{pp}) is applied to the corrosion cell, and the impedance response of the system at the metal-electrolyte interface is recorded over a specific range of frequencies. The final phase is to develop an equivalent electrical circuit so that the impedance response of the model fits the experimental measurements. The results later will be used to identify the corrosion properties of the sample. A brief review of electric double layer and impedance spectroscopy is given in this chapter; however, the reader is referred to Bard and Faulkner (1983) for further details.

5.1.1 Electrical Double Layer

Electrochemical interactions in concrete are more complex than basic redox reactions that occur between the iron and water molecules, whether they be hindered adsorbed, capillary, or in excess near the metal surface. Factors like minerals in sand and coarse aggregates, hydration products, and anhydrite cement can influence the charge transfer and consequently the whole electrochemical process. As discussed in Chapter 2, the iron atoms tend to lose

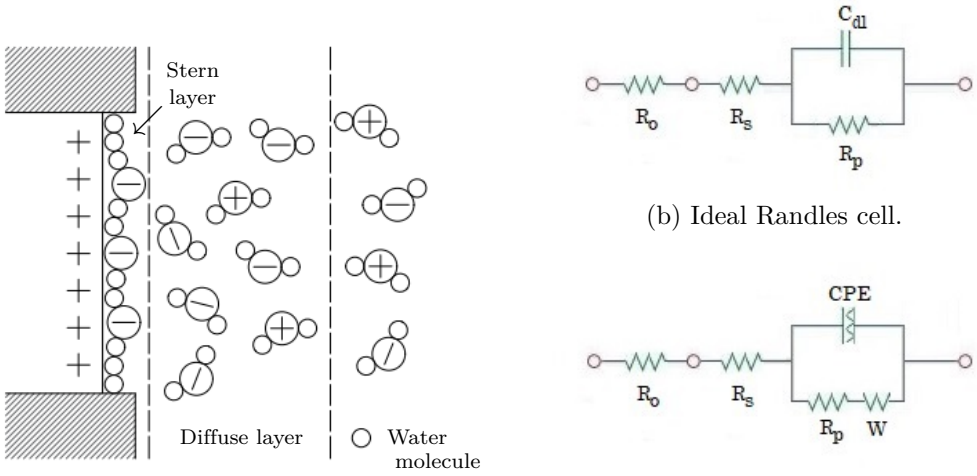

(a) Double layer theory.

(b) Ideal Randles cell.

(c) Modified Randles cell.

Figure 5.1: Electrochemical interactions at the metal surface modeled with Randles cell, modified from (Bard & Faulkner, 1983).

electrons to form ferrous (Fe^{+2}) and ferric (Fe^{+3}) ions which attract anions such as chloride ions and hydroxides. This causes a mass transport in addition to the charge transfer between the metal and its surroundings.

When redox reactions are taking place, a uniform positive or negative net charge forms on the surface depending on the metal being oxidized or reduced during the chemical interactions. Assuming positive charges are distributed at the surface of the metal (Figure 5.1a). The net charge attracts anions at the metal surface to bring the system into equilibrium. As the concentration of negative ions increases, strong intermolecular forces develop so that the attractive force pulls cations within a range of a few Angstroms, and simultaneously the repulsive force pushes anions away. The electrostatic force developed close to the metal surface results in the formation of an electrical double layer. The former layer consisting of anions is called Stern layer (also sometimes referred to as Helmholtz layer), and the latter that contains anions with a lesser degree of cations is known as the diffuse layer. Not only are anions found in the Stern layer. In fact, the population of solvent molecules in the Stern layer is more than the negative charges. Adsorbed species are usually surrounded by water molecules that are polar and attract both positive and negative charges.

5.1.2 Impedance Analysis

Understanding that the interaction between the metal components and surrounding counter ions are measured during impedance spectroscopy performance, it is required to find an electrical equivalent circuit to model both ionic exchange at the metal surface and electrostatic interaction developed as a result of osmosis. A Randles circuit shown in Figure 5.1b is normally used to fit the experimental data. The electric double layer is simulated with a capacitor, C_{dl}, in parallel with polarization resistance, R_p, that is used to estimate the corrosion rate of the sample. The model is in series with an ohmic resistance, which sums a known load resistance, R_o, and a solution resistance between working electrode and solution, R_s. The Randles model is beneficial because it makes it possible to develop impedance analysis for the experimental measurements from EIS.

Impedance, $\hat{z}$, quantifies the resistance of electric components to an alternating current, which is defined according to Ohm's law,

$$\hat{z} = \frac{v(t)}{i(t)} \ . \tag{5.1}$$

Electric potential, $v(t)$, is a time-dependent quantity that is modeled with a sine function;

$$v(t) = V \sin(\omega \mathrm{t}) \ . \tag{5.2}$$

Similarly, alternating current $i(t)$ is

$$i(t) = I \sin(\omega \mathrm{t} + \phi) \ . \tag{5.3}$$

Therefore, the impedance defined in Eq. 5.1 in terms of alternating voltage and current can

be rewritten as

$$\hat{z} = Z\frac{\sin(\omega \mathrm{t})}{\sin(\omega \mathrm{t} + \phi)} \ , \tag{5.4}$$

where $Z = V/I$ is the amplitude signal. The time phase shift, ϕ, between the input voltage and measured current introduced in Eq. 5.4 demonstrates the fact that the current leads the voltage for the electric double layer described above. Any change in phase between input and output signals corresponds to a given change in frequency. Hence, the phase alteration over a range of frequencies can be obtained where the experimental data is converted to the frequency domain with the aid of Fast Fourier Transform (FFT) for each signal applied to the cell. After computing the experimental impedance $\hat{z}$, the goal is to find an equivalent impedance of Randles cell in frequency domain (Eq. 5.5) so that z fits the experimental data, $\hat{z}$,

$$z = R_\Omega + \frac{R_p}{1 + j(\omega R_p C_{dl})} \ , \tag{5.5}$$

where $R_\Omega = R_o + R_s$, $j^2 = -1$, and C_{dl} is double layer capacitance. In order to differentiate between charge transfer process and mass transport in an electric double layer, it is convenient to simplify Eq. 5.5 to

$$z = z_{re} + j z_{im} \ , \tag{5.6}$$

where real and imaginary components of impedance are

$$z_{re} = R_\Omega + \frac{R_p}{1 - (\omega R_p C_{dl})^{\,2}} \ , \tag{5.7}$$

$$z_{im} = \frac{\omega {R_p}^2 C_{dl}}{1 - (\omega R_p C_{dl})^{\,2}} \ . \tag{5.8}$$

Since z is defined in complex plane, the magnitude and the phase of impedance are $|z| =$

$\sqrt{z_{re}^2 + z_{im}^2}$ and $\phi = \tan^{-1}(z_{im}/z_{re})$, respectively.

Obtaining the equivalent Randles cell, it becomes possible to construct Bode and Nyquist diagrams that are used to interpret the EIS data. For example, the imaginary component in Eq. 5.6 approaches zero in the case of a low frequency signal, meaning the equivalent impedance becomes a summation of ohmic and polarization resistance. However, the impedance becomes only ohmic when a high frequency signal is applied to the system.

The simplified Randles model sometimes fails to predict charge transfer at the surface of the metal with adequate accuracy or to depict the mass transport process, more particularly when a low frequency is applied to the cell. Therefore, the model can be enhanced by using a constant phase element (Figure 5.1c) instead of the ideal capacitor so that the model fits the data well. Eq. 5.9 represents impedance in term of a constant phase element,

$$z = Z_o(j\omega)^{-n} = Z_o\omega^{-n}\mathrm{e}^{-jn\pi/2} \ . \tag{5.9}$$

n is defined in the range of 0 to 1. If the parameter n is equal to 1, Randles cell models an ideal capacitive system, and if it approaches 0, the circuit simulates a resistive system. If n is 0.5, then the impedance in Eq. 5.9 reduces to Warburg impedance. All in all, n ought to be over 0.5 for the systems that both charge transfer and mass transport control the cell's interactions.

5.2 Experimental Procedure

Figure 5.2 represents a schematic view of a corrosion cell and apparatus required for impedance measurements. A three-electrode cell consisted of a platinum counter electrode, a single salt bridge calomel reference electrode 232, and the specimen as a working electrode. Prior to beginning impedance spectroscopy, specimens were prepared for EIS operation similar to the procedure used for CPP. The wires used during EIS included 127 millimeters [5 inches] long ASTM A 416 wires that are metallic coated, uncoated, or kept in as-received conditions. A polyolefin shrink tube with 6.4 mm [0.25 in] in diameter separated the exposure area, 303

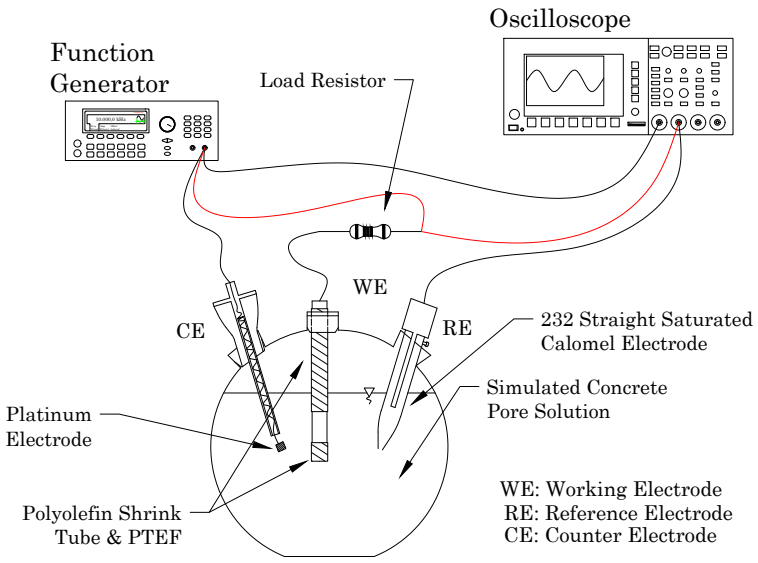

Figure 5.2: Schematic view of corrosion cell during EIS operation.

mm^2 [0.47 in^2] from the rest of the sample. Then, the polyolefin mask was covered with polytetrafluoroethylene plastic tube for air-tightening purposes and protection purposes as discussed previously for CPP.

As the goal of EIS performance is to identify the electrochemical properties of coating layers in corrosive environments, it is most appropriate to use an aqueous solution of potassium chloride, potassium sulfate, and potassium thiocyanate proposed by DIBt (Table 4.1), which models a realistic corrosive environment in prestressed concrete. The test was also repeated in a simulated pore solution so that it is possible to evaluate polarization resistance of the samples in different conditions. A smaller corrosion cell was used in EIS operation as compared to CPP so that it becomes possible to hold the reference electrode closer to the working electrode. Hence, the volume of the solution in EIS was reduced to 400 milliliters which satisfies ASTM G 31 limitations. After cleaning wires with acetone and deionized water, the samples were placed in the solution for about one and half hours to stabilize. EIS was performed at room temperature with an average pH of 7 for the corrosive environment and 12 for the simulated pore solution.

As shown in Figure 5.2 and Figure 5.3, the EIS operation was completed with the aid of a function generator and an oscilloscope. A low voltage range of a sine wave (20 mV_{pp})

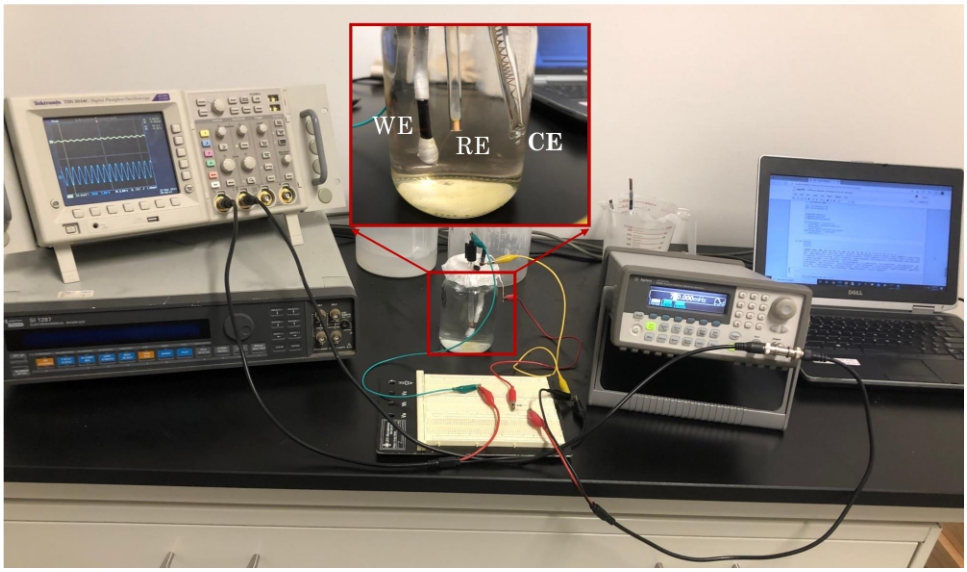

Figure 5.3: EIS experimental setup and apparatus.

constructed from the function generator was applied to the corrosion cell, and the results were visualized on the oscilloscope and compared to the reference signal that directly came from the function generator. A python script (Appendix A.3) was developed to log the visualized measurements from the oscilloscope, and to perform FFT on all the input and output signals. The frequency of the input signal was swept logarithmically with 10 points per decade where the frequency range was 1 Hz to 100 kHz. The python script determined phase shifts between the input voltage and output signals for every decade and recorded the results in a spreadsheet file. During the operation, 10 kΩ load resistor was added to the circuit to avoid any instability in calculations. The ohmic resistance was later subtracted from the results to obtain polarization resistance with a good accuracy from the EIS data. Additionally, it may be suggested to enclose the three-electrode cell in a Faraday's Cage to reduce noise in the measurements.

5.3 Experimental Results

All the frequency responses registered during EIS are shown in the magnitude and phase Bode diagrams in Figure 5.4. A significant change in impedance response was seen where high-strength steel wires were tested in dissimilar environments. As an example, the amplitude

impedance of the system was approximately 80 kΩ cm^2 for as-received wire when EIS was performed in a simulated pore solution, but it reduced to less than 10 kΩ cm^2 for the test with the aqueous solution proposed by DIBt. In addition, the phase angle computed for the sample in a concrete simulated environment was approximately 53 degrees, whereas it was closer to 17.1 degrees in the corrosive solution (Figure 5.4a). A phase shift observed for the sample tested in different solutions implies capacitive behavior of the system in an alkaline environment.

Recorded data for the sample coated with nickel-cobalt alloy shows a similar impedance response. The impedance was reduced by 70 kΩ cm^2 when the sample was tested in the aggressive environment. The phase angle was also computed lower in this environment—almost 51 degrees in the simulated pore solution and 38.4 degrees in the corrosive solution (Figure 5.4b). An opposite response registered for the steel wire coated with zinc-nickel alloy. As shown in figure 5.4c, the amplitude impedance obtained for the specimen tested in alkaline environment was quite low at 0.45 kΩ cm^2, yet it intensified to 1.35 kΩ cm^2 where EIS was operated in a lower pH solution. Phase angle was also shifted from almost 33 degrees to 53 degrees as the pH of the solution decreased to 7. This observation agrees with the conclusion drawn from potentiodynamic testing in Chapter 4. Steel wires coated with zinc-nickel showed more corrosion resistance in a corrosive solution rather than an alkaline environment.

The capacitive behavior of the system observed in phase diagrams identifies the quality of coatings and their performance in dissimilar environments. As discussed, phase angles increased for both zinc-phosphate and nickel-cobalt coated specimens were examined in a simulated pore solution that indicates a high performance of the coating systems in a concrete environment. The Bode diagram in Figure 5.4d demonstrates a comparison between frequency response from as-received and uncoated ASTM A 416 wires in an aqueous solution with pH above 11. The amplitude impedance of the specimen with zinc-phosphate coating is slightly higher than uncoated sample implying the influence of the coating layer on the frequency response of the system. Analyzing the phase diagram computed from EIS data makes the

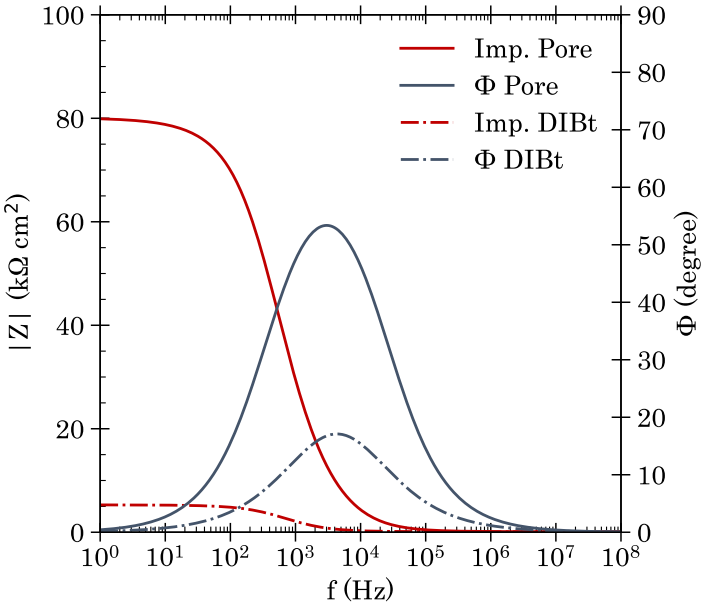

(a) As-received specimen tested in simulated pore and corrosive environments.

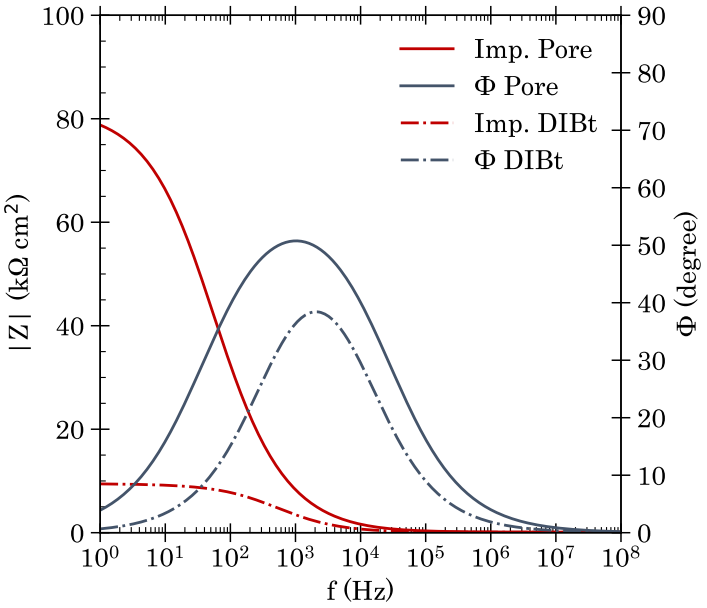

(b) Nickel-cobalt wire tested in simulated pore and corrosive environments.

Figure 5.4: Amplitude and phase Bode diagrams.

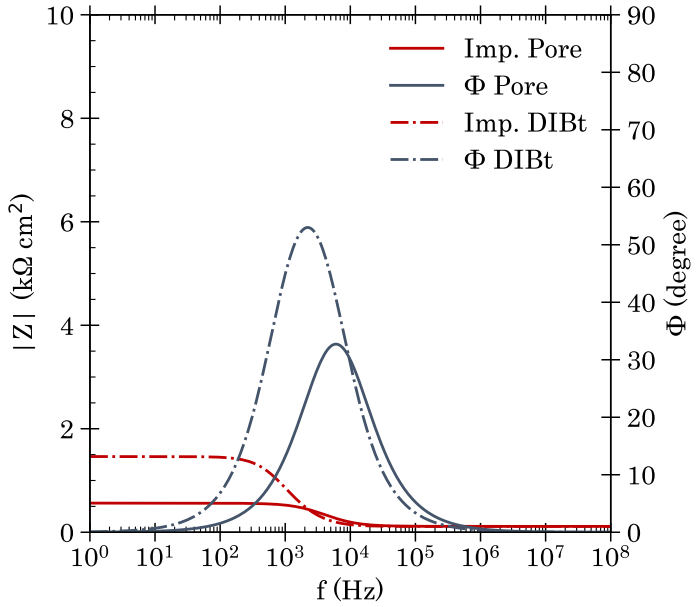

(c) Zinc-nickel wire tested in simulated pore and corrosive environments.

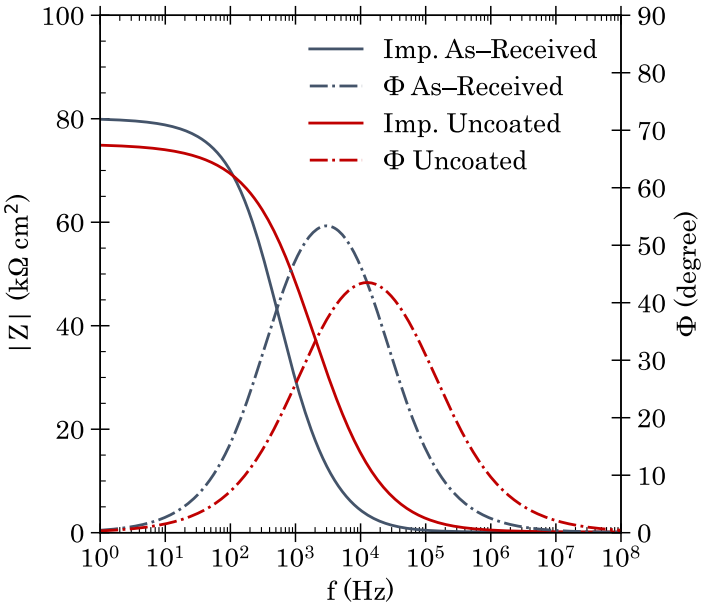

(d) As-received and uncoated samples tested in simulated pore environment.

Figure 5.4: Amplitude and phase Bode diagrams, continued.

Table 5.1: Fitting parameters obtained from a modified Randles cell.

Sample	Solution	R_p [a]	R_s [b]	Q = 1 / Z_o	n
		kΩ cm^2	Ω cm^2	μs Ω^{-1}cm^{-2}	
As-Received	simulated pore	79.8	93	1.23	0.81
	DIBt	5.19	93	5.37	0.93
Ni/Co	simulated pore	78.5	100	1.73	0.75
	DIBt	9.34	87	13.2	0.72
Zn/Ni	simulated pore	0.45	113	729	0.96
	DIBt	1.35	113	210	0.95
Uncoated	simulated pore	74.8	108	1.93	0.70

[a] Polarization Resistance
[b] Solution Resistance

effect of coatings more noticeable. As shown in Figure 5.4d, the phase angle increased from 43.5 degrees for the uncoated wire to 53.4 degrees for the as-received specimen that specifies the effective performance of the coating layer.

Coatings indeed improved the time constant of charge transfer reactions. As shown in Figure 5.4d, the resonance frequency shifted to lower frequency from 12.9 kHz for uncoated specimen to 3 kHz for as-received wire indicating that the mass transport process takes place at a faster rate for the uncoated wire. This was also evident from the results obtained for as-received wires in dissimilar aqueous solutions since the time constant became slightly more when the sample tested in a concrete simulated environment (Figure 5.4a). The time constant similarly increased for the nickel-cobalt coated sample for the test performed in the simulated pore solution (Figure 5.4b). As it was anticipated, the resonance frequency moved to a higher frequency when zinc-nickel wire was tested in an alkaline environment (Figure 5.4c) implying that diffusion plays a dominant role in the process.

Table 5.1 gives the optimal values of fitting parameters obtained from the Randles equivalent circuit that was modified with a constant phase element. Frequency independent variables, Q and n, modify the admittance of the constant phase element so that the impedance

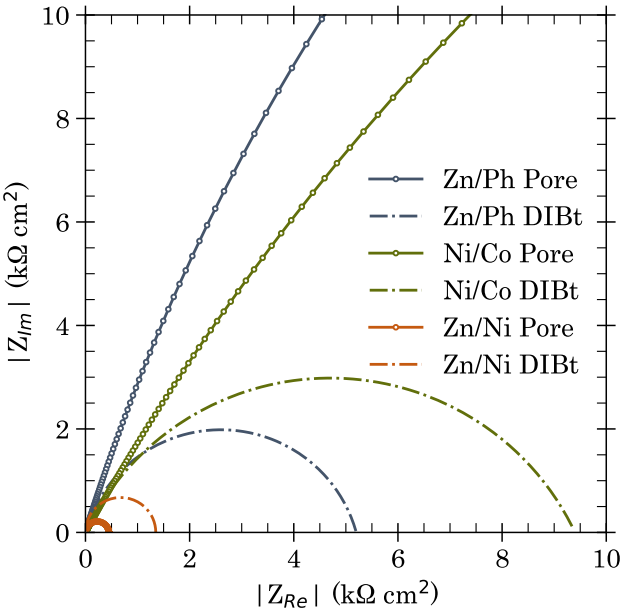

Figure 5.5: Nyquist plot constructed for high steel-strength wires coated with zinc-phosphate as well as zinc-nickel and nickel-cobalt alloys.

results of an equivalent cell fit the experimental data. The resistance between working and reference electrodes, which is defined as ohmic resistance of the electrolyte or R_s, was measured on average 100 Ω cm^2. The polarization resistance of the systems given in Table 5.1 was computed from Nyquist plots in Figure 5.5 and Figure 5.6. Since the values agreed with the results determined from Stern-Geary equation, they were used to obtain corrosion rate of the coated and uncoated steel wires tested in different environments as reported in Table 4.2.

The polarization resistance of ASTM A 416 wires coated with zinc-nickel tested in both the concrete simulated and the corrosive solution was quite low in comparison with the values obtained for other samples. The polarization resistance estimated for the zinc-nickel sample was 0.45 kΩ cm^2 in the alkaline environment and was 1.35 kΩ cm^2 in the aqueous solution proposed by DIBt. This was also shown in the Bode diagram in Figure 5.4 where the amplitude impedance was significantly lower than the results computed for other coatings. However, the polarization resistance found for the nickel-cobalt sample in the simulated pore solution was close to the one registered for as-received wire, approximately 80 kΩ cm^2, and it was slightly higher than the polarization resistance determined for uncoated wire

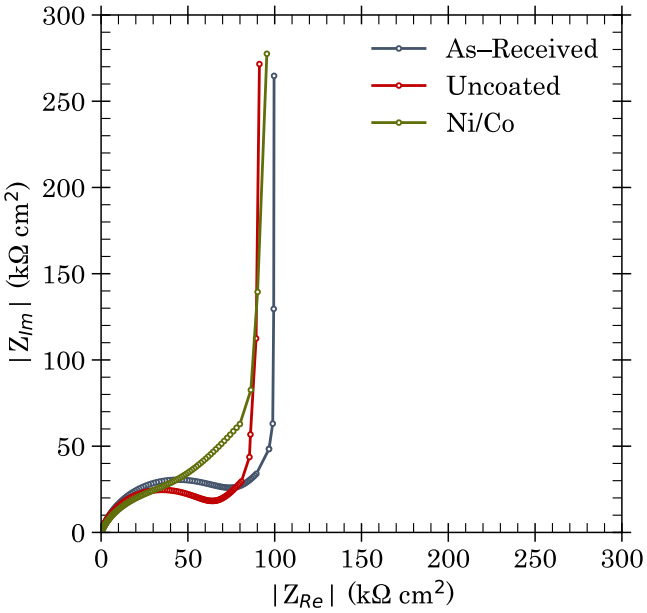

Figure 5.6: Nyquist plot constructed for uncoated ASTM A 416 steel wire as well as ones coated with zinc-phosphate and nickel-cobalt alloy tested in simulated pore solution.

that was 74 kΩ cm^2. This implies that the coatings improve the corrosion resistance of the high-strength steel wire in concrete. When coatings were tested in a corrosive environment, the polarization resistance substantially reduced to less than 10 kΩ cm^2. It was observed that the polarization resistance recorded for the nickel-cobalt specimen was slightly higher than the one obtained for as-received wire (Figure 5.5). As anticipated, the impedance of the system was controlled by diffusion process rather than charge transfer at low frequency signals, so a modified Randles cell with a constant phase element was used to construct the Nyquist plot in Figure 5.6. Zinc-phosphate layer showed a higher resistance where mass transport was a dominant process. Similarly, the nickel-cobalt coating exhibited a relatively strong diffusion resistance, even though the rate of kinetics happened slightly faster. The transition between charge transfer and diffusion process for the nickel-cobalt sample occurred at approximately 40 kΩ cm^2, and the tail of the impedance was a straight line at 45 degrees before the slope increased to almost 90 degrees for very low frequency signals. Figure 5.7 displays the specimens tested in a corrosive environment after finishing the EIS operation. As shown, no severe corrosion was observed on samples after completion of the experiment.

(a) As-Received ASTM A 416 wire tested in a corrosive environment (pH=7).

(b) Uncoated ASTM A 416 wire tested in a corrosive environment (pH=7).

(c) Ni/Co coated wire tested in a corrosive environment (pH=7).

(d) Zn/Ni coated wire tested in a corrosive environment (pH=7).

Figure 5.7: Samples after completion of EIS.

5.4 Further Discussion and Closing Remarks

This chapter focused on the impedance response of ASTM A 416 steel wires that were tested in dissimilar environments. It was concluded that the impedance of all the samples is relatively high, about 80 kΩ cm^2, in a concrete simulated solution, except for the samples coated with zinc-nickel. However, the impedance response of the zinc-nickel coated samples improved where the test was performed in a corrosive environment that agrees with the conclusion drawn from the potentiodynamic test in Chapter 4. Studying the phase diagrams constructed from EIS data revealed that the coating systems, either the zinc-phosphate that is currently applied to steel wires or the metallic coatings proposed in this work, enhances the time constant of the charge transfer process. In general, polarization resistance of as-received wires and the specimens coated with nickel-cobalt alloy were found higher than the ASTM A 416 steel wires without any coating. The resistance significantly decreased for EIS repeated in a corrosive environment instead of the simulated pore solution. For the specimen coated with zinc-nickel, polarization resistance was reduced three times where the test was performed in a concrete environment.

6. GALVANOSTATIC CHLORIDE ACCELERATION

6.1 Introduction

An additional study was conducted to assess the efficacy of impressed current against chloride ions in order to prevent localized corrosion on ASTM A 416 wires with or without coatings. Hence, Galvanostatic Chloride Acceleration (GCA) was conducted to identify kinetic properties of the steel wires in corrosive environments while the cathodic protection system is operating. During the galvanostatic test, a fixed impressed current is applied to the cell to protect a sample that was immersed in a chloride solution, meanwhile the potential variations of the specimen are measured over time. The equipment needed for the test operation is similar to CPP: a three-electrode cell consisting of a working electrode, a reference electrode, and a platinum counter electrode as well as a galvanostat that maintains the impressed current during the test. Chloride ion concentration is increased over time during the galvanostatic test since the aggressive ions are the main reason for localized corrosion in reinforced concrete, while the other variables that influence the experiment have to remain unchanged.

Pedeferri (1996) discussed the application of impressed current in reinforced concrete and described requirements to cathodically protect reinforcement from corrosion. Determining the proper current density to protect steel from degradation depends on both the ambient conditions and chloride content of the surrounding concrete. It is evident that the impressed current should be higher for the aggressive environment; however, an extensive impressed current may alter the mechanical properties of adjacent cement, or may cause hydrogen embrittlement in the metal, as discussed in Chapter 2. Pedeferri also noted that the influence of oxygen diffusion should be considered in the design of cathodic protection systems. In this study, a current density in the range of 0.01 to 0.3 μA/cm^2 is considered as a norm impressed current for the use in concrete structures, and higher than 1 μA/cm^2 is assumed as extensive,

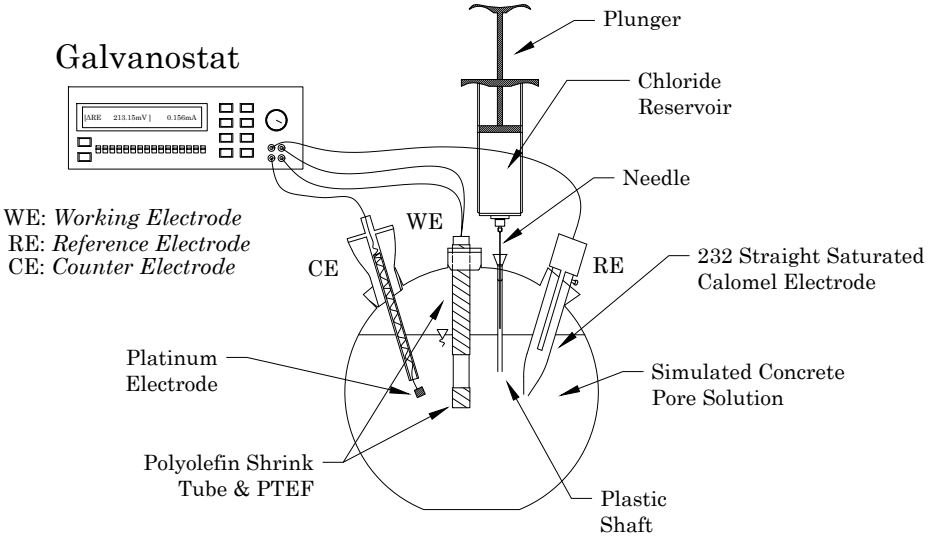

Figure 6.1: Schematic view of corrosion cell during GCA operation.

which increases the risk of ASR in concrete and results in brittle failure of the reinforcement.

6.2 Experimental Procedure

In order to evaluate the efficacy of the impressed current system to prevent localized attacks, a fixed current was applied to the corrosion cell (Figure 6.1). A Solartron 1287A galvanostat maintained a continuous current and logged the potential variation of the cell for almost three hours. Before applying the current, all the working electrodes were placed in the solution for two hours until the passivation process reached its end. It was decided to conduct the experiments in an environment suggested by Trejo et al. (2009) since the pH of the simulated pore solution is much closer to the one in concrete bulk. Note that the solution was made of a combination of three hydroxides and a small amount of gypsum as given in Table 4.1.

The sample preparation process was similar to steps followed during CPP operation. After pretreatment of 127 millimeters [5 inches] long ASTM A 416 wires, a polyolefin shrink tube was used to secure the top and bottom of the exposed area in addition to a few layers of Polytetrafluoroethylene that were applied to seal the contact areas and avoid moisture penetration. The unmasked area was 303 mm^2 [0.47 in^2] for all samples both with and without coatings.

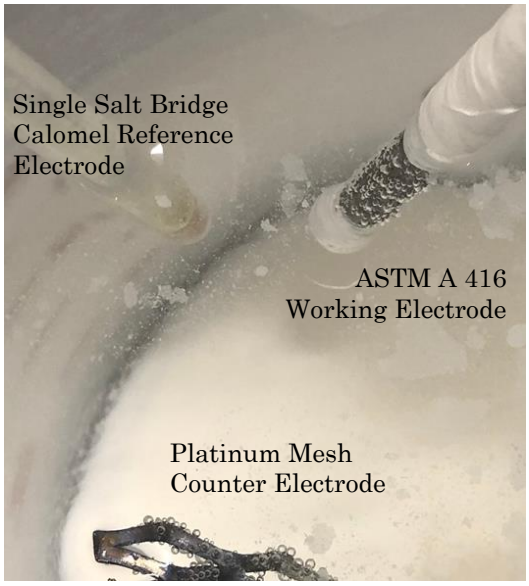

Figure 6.2: Three-electrode cell during GSA performance.

After the preparation process was completed, the Galvanostat was connected to a platinum counter electrode, the working electrode, and a single salt bridge calomel reference electrode 232 (Figure 6.2). In addition to these electrodes, a small size plastic shaft was provided for the purpose of saline water injection. As the stabilization of the sample reached, the Solartron 1287A electrochemical interface was set on galvanostatic mode to apply 1.33 μA/cm^2 fixed current to the working electrode, while 100 ml of a chloride laden water was injected to the solution over 3 hours.

A python script (Appendix A.3) logged the readings from the Galvanostat in a CSV file. Two sets of data were collected from the galvanostatic test, voltage variation with time and the percentage of chloride content in the simulated pore solution. Note that the injection of an aqueous salt solution was repeated every 5 minutes and continued up to the time that the 3% chloride content threshold in the concrete simulated solution was reached. The procedure explained herein was repeated for high-strength steel samples in the same environment but for the current density fixed at 0.13 μA/cm^2 so that it becomes possible to study the effect of norm and extensive impressed currents on electrochemical properties of wires.

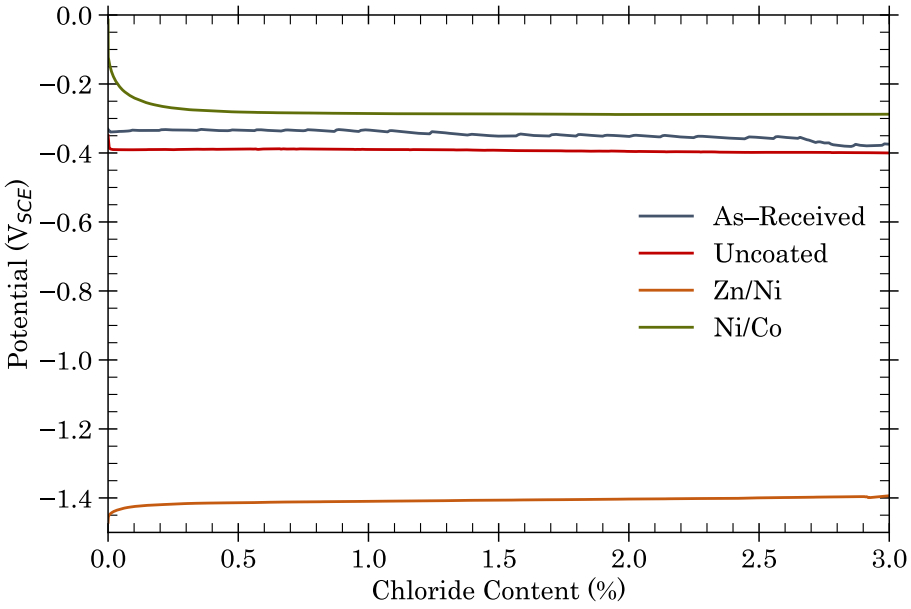

Figure 6.3: Specimens protected in an aqueous solution of 3% chloride laden water during the galvanostatic test where an extensive impressed current density (1.33 μA/cm^2) was applied to the cell.

6.3 Experimental Results

The specimens used during GCA testing included as-received wires coated with zinc-phosphate, samples coated with nickel-cobalt and zinc-nickel alloys as well as ASTM A 416 wire without any coating, herein referred to as uncoated wire. Figure 6.3 shows potential variations of samples as a function of chloride content in the solution where an extensive current density is applied to the cell. No sign of corrosion was observed during operation and after the test completion, and the voltage became steady for all the samples as the test progressed. The potential of the nickel-cobalt sample was higher than other coatings, while the voltage recorded for the zinc-nickel sample was as low as -1400 mV vs. SCE, which was about 200 mV lower than the open circuit potential measured for the zinc-nickel wires before. Potential logged for as-received wire was slightly higher than uncoated wire, and it became even closer at the end of the experiment. The results demonstrated in Figure 6.3 prove the efficacy of cathodic protection in a corrosive environment since the samples were immersed in a solution where pH gradually dropped in a range of 7 to 8 during the test operation.

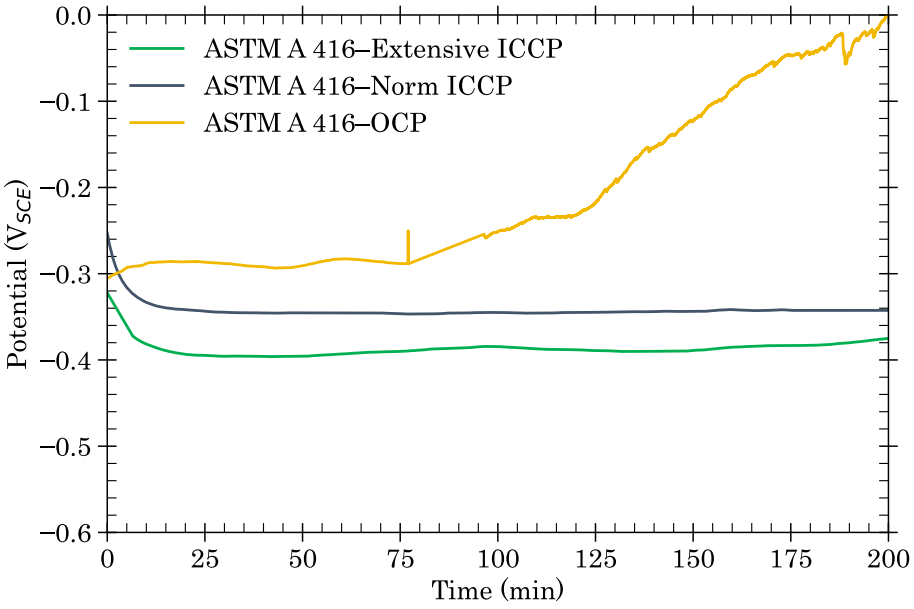

Figure 6.4: Uncoated ASTM A 416 wires immersed in 3% aqueous salt solution and protected by the impressed current system.

Figure 6.4 shows potential variations with time for uncoated ASTM A 416 wires in 3% aqueous salt solution. The experiment was initially conducted in this environment without any protection system, and the open circuit potential was measured during the test operation. Then, the experiment repeated for a sample protected with a norm current density (0.13 μA/cm^2) and for another sample protected with an extensive current density (1.33 μA/cm^2). Corrosion pits initiated after 75 minutes of testing for the sample that was not cathodically protected where the potential increased over time with a positive rate. This was not the case for other samples protected with impressed current. The voltage variations were steady proving that localized corrosion did not initiate during the test period. Consequently, raising current density results in negative potential in the cell. This becomes more evident when a comparison is made between the voltage logged for the samples protected with norm and extensive current density. As shown in Figure 6.4, the potential of the cell was about 20 mV less when an extensive current density was used.

Figure 6.5 demonstrates change in voltage over time for ASTM A 416 uncoated wires placed in dissimilar environments. One sample was immersed in a simulated pore solution

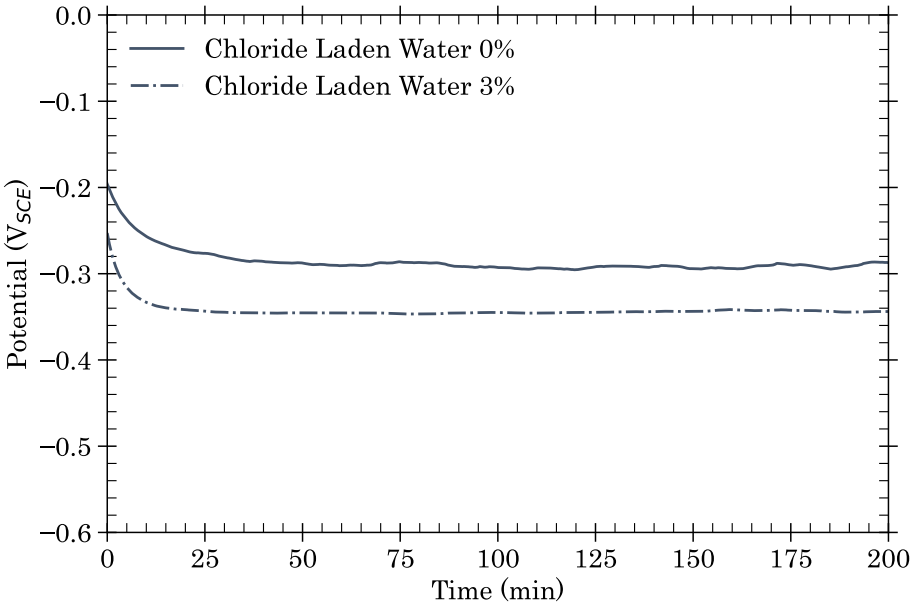

Figure 6.5: Uncoated ASTM A 416 wires protected by norm impressed current, 0.13 μA/cm^2.

with no chloride ions, and another specimen was positioned in the same environment with a chloride concentration of 3%. Both samples were protected with a norm impressed current during the galvanostatic test. No traces of localized corrosion were detected during and after the experiment for samples protected from degradation in both concrete simulated and corrosive environments. Potential recorded for the sample placed in the solution with high concentration of chloride ions was more negative compared to the other one that shows a higher current density was required to protect the metal in this environment.

Figure 6.6 shows ASTM A 416 steel wires with and without coatings tested during the galvanostatic test. The level of degradation was severe on the tails of all samples that were exposed to aqueous salt solution and left in the air. In contrast, the heads that were cathodically protected remained intact without sign of degradation or pitting initiation. If the design current density is not sufficient to protect the metal in a corrosive environment, then corrosion pits initiate and propagate in a short time period. Their severity depends on the ambient conditions. Figure 6.6g indicates that the protection level was not adequate for the zinc-nickel sample. Pits appeared during the experiment and grew in a day after the sample was left in the air at room temperature.

(a) Uncoated steel wire protected in corrosive environment (pH=7).

(b) Uncoated steel wire exposed to corrosive environment (pH=7).

(c) Ni/Co coated wire protected in corrosive environment (pH=7).

(d) Ni/Co coated wire exposed to corrosive environment (pH=7).

Figure 6.6: Samples after completion of GCA.

(e) Zn/Ni coated wire protected in corrosive environment (pH=7).

(f) Zn/Ni coated wire exposed to corrosive environment (pH=7).

(g) Zn/Ni coated wire protected with impressed current. The potential limit to protect the sample was not achieved, causing the zinc coated layer to break off and develop uniform pits on the surface of the substrate. Pits were small and it was difficult to see with an unaided eye. After the sample was left at room temperature for a day, the uniform pits propagated throughout the surface and caused uniform corrosion.

Figure 6.6: Samples after completion of GCA, continued.

6.4 Further Discussion and Closing Remarks

This chapter examined the efficacy of impressed current to protect ASTM A 416 steel wires in an aggressive environment. It was concluded that both norm and extensive impressed currents are capable of protecting steel wires in a corrosive environment, and no trace of corrosion was detected during or after the completion of the galvanostatic test. It took nearly 75 minutes for the system to become unstable when as-received specimens were immersed in simulated pore solution mixed with 3% chloride laden water without utilization of cathodic protection. Another observation was the influence of chloride ions on the electric potential of the system so that the voltage level was more negative for a higher concentration of the chloride ions.

7. HYDROGEN EMBRITTLEMENT EXAMINATION

7.1 Introduction

This is a standard test designed to examine the susceptibility of high-strength steel wires to hydrogen embrittlement in laboratories mainly based on recording time-to-failure of prestressing wires (ACI cmte. 222, 2014). By 1970, the number of publications on brittle failure of high-strength steel had been limited to European research works, while a few studies conducted in the U.S. laboratories were more focused on improving the metallurgical properties of wires (Wu & Clifton, 1981). However, a set number of examinations were conducted in Oak Ridge National Laboratory in the mid-70s to investigate the failure mode of steel strands as a result of tensile stress (Griess, 1978) and to study the efficacy of coating layers to reduce the brittle failures of prestressing wires (Naus, 1979). In 1978, the International Federation of Prestressed Concrete collected all the tests that had been performed by the time and proposed a standard approach to study the risk associated with hydrogen embrittlement for high-strength steel strands used in prestressed structures. The proposed test is known as the FIP.78 guideline, and as of today it is a common technique to identify the susceptibility of steel strands to hydrogen embrittlement.

FIP.78 recommended the use of an aqueous environment of ammonium thiocyanate (NH_4SCN) in corrosion cells. This recommendation was based on studying several tests conducted in dissimilar solutions. In the end, it was concluded that those experiments performed in ammonium thiocyanate showed reproducible results compared with others (Wu & Clifton, 1981). While FIP.78 was a significant breakthrough to investigate hydrogen permeation in high steel strands, there were still some concerns over the environment employed in the embrittlement test. ACI 222.2R-01 (2014) reported some of these concerns and summarized problems attributed with stress corrosion cracking rather than hydrogen embrittlement.

The aggressive environment used in FIP.78 is not what a prestressing wire experiences over the course of its service life; hence, a few years after FIP's guideline, the Deutsches Institut für Bautechnik introduced an alternative environment as discussed in Chapter 4. Table 4.1 gives the details of the test environment used in FIP.78 and DIBt. The difference between the two standards comes from the chemical solutions in the corrosion cell, and only the test environment differs from each test. Hence, a radical condition that is a very acidic environment is recommended for the FIP.78 test, while a more realistic condition is employed in the DIBt approach. That said, a drawback that has to be addressed for the DIBt technique is the time duration of the test that takes at least 2000 hours of operation. Elices et al. (2008) conducted an experiment in order to compare the results from both tests. The conclusion was that although FIP.78 does not recommend a realistic concrete environment, it is acceptable to use as a quality control of prestressing wires.

7.2 Experimental Procedure

Sample preparation began with cutting the as-received wires to a 381 millimeters [15 inches] length and coating them with zinc-nickel and nickel-cobalt alloys with the steps stated in Chapter 3. After finishing electroplating, a 6.4 mm [0.25 in] diameter polyolefin shrink tube was applied to the sample wires to restrict on either side of the exposed area of 6.28 cm^2 [1 in^2]. Then, the coated samples were placed in a test setup that was built for the purposes of the embrittlement test. Figure 7.1 demonstrates a schematic view of apparatuses used during the hydrogen embrittlement test. A test frame consisted of a 100-ton single acting hydraulic cylinder with 57.2 millimeters [2.25 inches] stroke jack that was sandwiched between two 30×30×1.3 centimeters [12×12×1/2 inches] base plates. These steel plates were held in place by four 0.91 meters [3 ft.] long and 1.6 cm [5/8 in] in diameter zinc plated threaded steel rods. Two 20×10×2 centimeters [8×4×3/4 inches] hot-rolled A36 angles provided to support the bottom base plates.

Two 12.7 millimeters [half-inch] holes were drilled in the middle of the left and the right side of the base plates other than four 22.2 millimeters [7/8 in] holes that were bored at

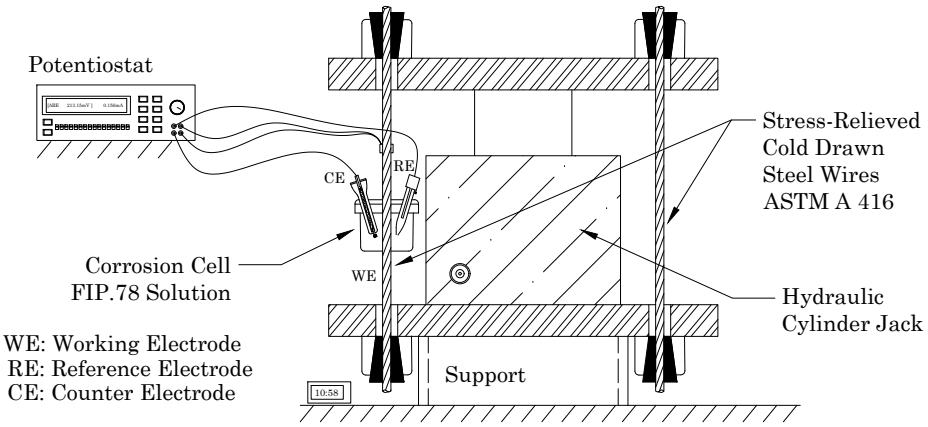

Figure 7.1: Schematic view of apparatus employed in hydrogen embrittlement test.

the corners of the base plates for the studs. The reason to drill the half-inch holes in the base plates was to secure samples during installation in the test setup. The space between these two holes was 228 millimeters [9 inches] from center to center. As shown in Figure 7.1, one as-received steel wire was placed on the right side of the setup to compensate for any probable bending and shear effects on the target sample on the left that was either zinc-nickel specimen, or nickel-cobalt sample, or an as-received wire.

High strength steel wires were tightened to the base plates with the aid of anchor wedges and C-Clamps. During tensioning of the wires, a spirit level was also used so that the upper base plate did not tilt out of position. Base plates were initially level and secured with four 15.9 mm [5/8 in] hex nuts positioned in each stud. However, no contact was made between support rods and base plates during the operation to ensure that the load generated from the jack was only transferred to the sample wires. The diameter of ASTM A 416 wires used in this study was 4.76 mm [3/16 in]; therefore, it was required that the hydraulic jack maintained its maximum capacity during the embrittlement testing in order to keep the applied load over 60% of steel stress rupture.

Figure 7.2 shows the hydrogen embrittlement test for a steel wire coated with zinc-nickel in progress. The environment employed in the test was an aqueous solution of 20% ammonium thiocyanate as recommended by FIP, and the corrosion cell was a three-electrode cell including a 9.7 cm^2 [1.5 in^2] platinum mesh counter electrode, a single salt bridge calomel reference

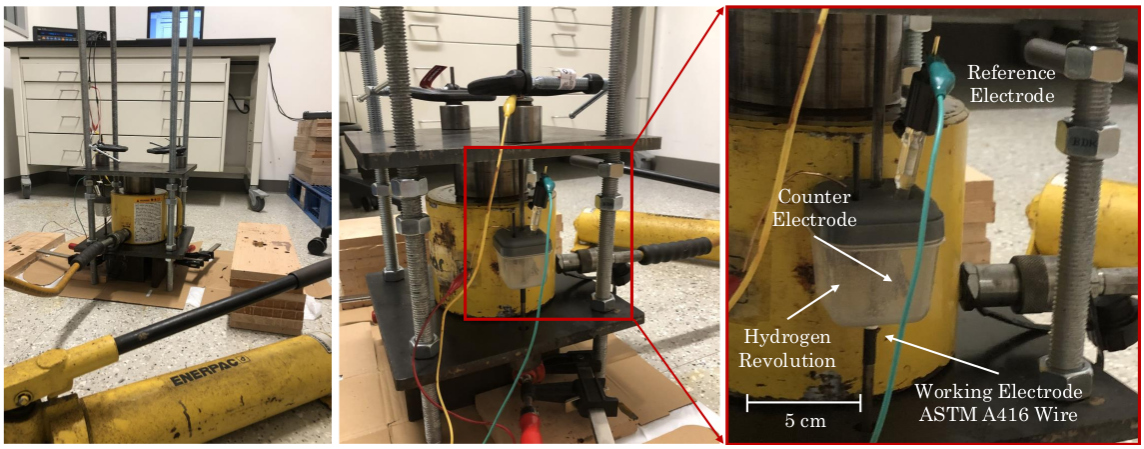

Figure 7.2: Experimental setup in hydrogen embrittlement test.

electrode, and the working electrode. A Solartron 1287A Potentiostat electrochemical interface continued in operation to keep the potential of steel wires as low as -1600 mV vs. SCE for the purpose of evolving hydrogen gas in the corrosion cell. An IEEE-488 GPIB interface made communication possible between the Potentiostat and a python script (Appendix A.3) where time-to-failure of prestressing wires and electric current variations were recorded for each sample during the experimental testing.

7.3 Experimental Results

The embrittlement test is dependent on the surface condition of prestressing wires, so the time to rupture may be different from each sample. Nürnberger et al. (1997) concluded a time to failure in a range of 12 to 48 hours for high-strength steel wires under tension in excess of 60% of their ultimate stress. However, this range was reduced to 2 hours on average for samples with surface defects as reported by Elices et al. (2008). In addition, the authors found that there is no significant variation of time to rupture for the samples tensioned up to 80% of their ultimate stress compared to the ones tensioned with 60%. Therefore, the result from the embrittlement test relies more on stress concentrations produced in wires because of surface defects as opposed to applied load.

FIP.78 recommends maintaining the temperature of the corrosion cell at 50°C to increase the solubility of hydrogen atoms in steel substrate. However, this is indeed not realistic

and does not model the environment that prestressing wires experience in concrete. Diaz et al. (2009) studied the effect of temperature on brittle failure of high strength steel wires in different environments. It was evident that the electrochemical behavior of wires was not altered by temperature; except that corrosion pits initiated when the temperature rose to 40°C. Hence, the failure of steel wire occurs as a result of surface defects and development of stress concentration rather than hydrogen diffusion. That said, it is a common agreement that raising the temperature in the corrosion cell increases the solubility of hydrogen atoms in steel substrate. Since the purpose of this study is to investigate the influence of impressed current on hydrogen embrittlement of steel wires, it was decided to maintain a constant room temperature in the corrosion cell. Then, hydrogen evolution in the cell occurred as a result of a negative potential that eventually led to the brittle failure of as-received steel wires. Wu (1981) also reported a set number of experiments conducted at room temperature to assess susceptibility of high-strength steel wires to hydrogen embrittlement.

Figure 7.3 shows the current density variations with time that were recorded from a Potentiostat during the test operation. The embrittlement test was initially conducted for an as-received wire that was subjected to tensile loads for multiple times prior testing, herein labeled Sample 1. The test was repeated for two other as-received wires that were tensioned once during the experiment. The Potentiostat maintained a constant negative voltage for the second sample, yet it was disconnected every 7 hours for 30 minutes so that surface defects such as pits initiated on the surface of the third sample. The significant change in current density recorded for the third sample was because of the voltage disturbance and pits initiation.

As shown in Figure 7.3, the time to rupture for Sample 1 occurred earlier than other samples. A plausible reason for the failure is perhaps microscale plastic deformations in the crystal structure of the metal that may be interpreted as the fatigue mechanism in addition to the hydrogen embrittlement. Sample 1 failed after almost 21 hours when the current density recorded by the Potentiostat considerably dropped to very small values—logarithmic current

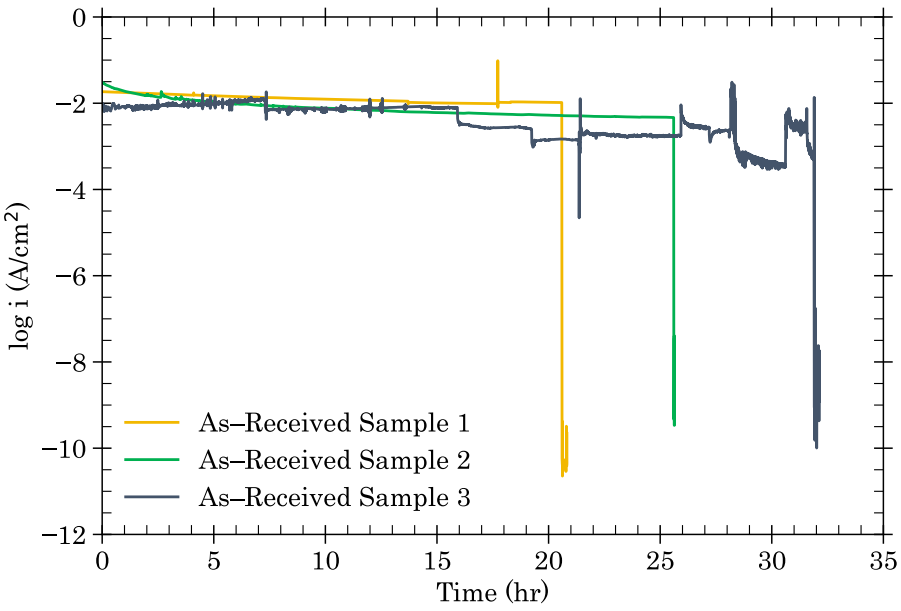

Figure 7.3: Current density variations in time for as-received wires. Sample 1 was subjected to multiple tensioning before the test began, but it was cathodically protected during the test. Sample 2 was tensioned once and continuously protected during the operation. Sample 3 was tensioned once, but it was not continuously protected during the embrittlement test.

density was approximately recorded at -10 mA/cm^2. The second sample fractured after 26 hours, and the third sample failed after 32 hours. A significant change in current density was seen prior to the failure of the third sample that may be a result of pitting initiation. However, it is evident that the voltage disturbance influenced the process of hydrogen evolution in the corrosion cell and caused a delay of the failure of the steel wire for a few hours.

Figure 7.4 shows a comparison between current density recorded for the second as-received wire (Sample 2) and specimens coated with nickel-cobalt and zinc-nickel alloys. Both proposed coatings passed the hydrogen embrittlement test. The test samples were subjected to an aggressive environment for up to 48 hours, and no sign of sharp cracks or brittle failures was seen on these samples. For the zinc-nickel sample, there were some instabilities on current measurements logged during the last 10 hours of the test operation. However, the instability on recordings should not be interpreted as initiation of pitting corrosion; in fact, it was a loose connection in electric wiring that might disturb communication between the Potentiostat and corrosion cell. No trace of localized corrosion was seen after detaching samples from the

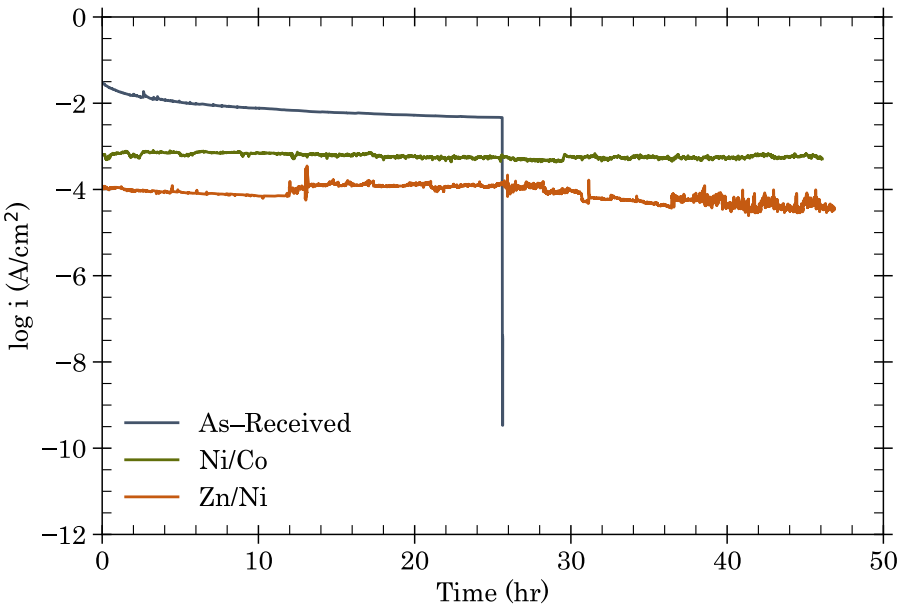

Figure 7.4: Current density variations in time for as-received as well as nickel-cobalt and zinc-nickel coated wires.

setup.

Figure 7.5 displays the second as-received wire as well as nickel-cobalt and zinc-nickel coated wires a month after the performance of the embrittlement test. As shown in this figure, a sharp and brittle crack occurred in the case of ASTM A 416 wire coated with zinc-phosphate layer, but no brittle failure occurred in the wires coated with proposed alloys. The severe localized corrosion seen on all samples did not happen during testing. After detaching samples from the corrosion cell, the test objects were stored in a drawer at room temperature where they were exposed to the oxygen. After a month, as-received wires corroded severely with a powdery surface followed by delamination of the metal surface. Propagation of corrosion pits was also found on the nickel-cobalt sample, yet the severity was not as high as the as-received wires. No signs of localized corrosion were observed for the wire coated with zinc-nickel even after a month of the test, but visible coating damage was detected as a result of detaching the sample from the corrosion cell.

Time to failure of the samples during the hydrogen embrittlement test are given in Figure 7.6. As shown in this figure, ASTM A 416 wires coated with zinc-phosphate failed on average

Figure 7.5: As-received specimen as well as nickel-cobalt and zinc-nickel coated wires a month after the embrittlement test, from top to bottom respectively.

28 hours of exposure to the aggressive solution recommended by FIP while they were protected by impressed current. Several factors including loading conditions, surface defects, and the amount of hydrogen atoms evolved during cathodic protection influence time to failure of the steel wires. For example, a range of 12 hours was registered for the time failure of as-received wires in this study. The embrittlement index demonstrated in Figure 7.6 was calculated based on time to failure logged for all the samples. The index is a dimensionless parameter in a range of 0 to 1, and it was computed from Eq. 7.1,

$$\mathrm{EI} = 1 - \frac{t_i}{t} \tag{7.1}$$

where t_i is time to failure of the samples, and t is the passing time limit of the embrittlement test assumed slightly over than 48 hours in this experiment. The index was minimal for both coatings suggesting a durable barrier to atomic hydrogen diffusion, and it was found to be much higher, approximately 0.5, for as-received wires.

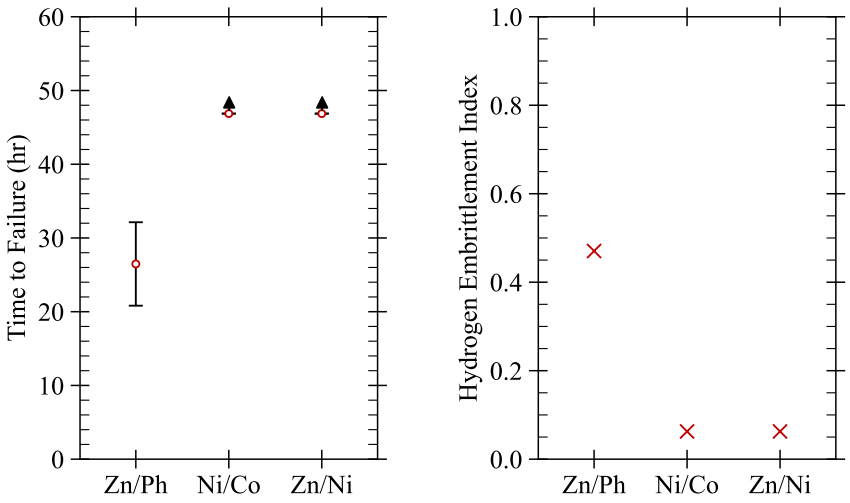

Figure 7.6: Time to failure and embrittlement index for as-received wire coated with zinc-phosphate as well as wires coated with nickel-cobalt and zinc-nickel alloys.

7.4 Further Discussion and Closing Remarks

This chapter demonstrates a research study to identify the susceptibility of ASTM A 416 steel wires to hydrogen embrittlement. It was concluded that the both zinc-nickel and nickel-cobalt alloys are promising barriers to diffusion of atomic hydrogen. However, this was not the case for as-received wires coated with zinc-phosphate since the specimens failed during the embrittlement test on average in 28 hours. The failure of the steel wires directly relied on the concentration of the hydrogen atoms in the corrosion cell. Time to failure increased for the specimen that was not continually protected by impressed current, while metal loss was seen over the exposed surface since an aggressive environment was employed in the embrittlement test. Therefore, the reduction in wire diameter was because of the initiation of corrosion pits that propagated until brittle fracture occurred. It was also observed that other factors such as surface conditions and fatigue loading might reduce the time to rupture of the specimens.

8. ADHESION AND DURABILITY OF PLATED LAYERS

8.1 Introduction

Any damage on coated layers causes the failure of the protection system. The final stage of this study examines if the metallic coatings proposed in this work are durable; particularly where steel strands were pulled through metal or plastic ducts. This chapter provides a brief review of terms that may affect the durability of coated layers in addition to an experimental procedure designed to estimate the wear resistance of the coating systems.

8.1.1 Adhesion

Adhesion refers to the atomic bonding between a deposited layer and a steel substrate so that the coating should not be readily separable from the underlying substance. A decent adhesion bond not only relies on the state of the interfacial region on which the bonding takes place between the coating layer and the substrate, but it is also controlled by interfacial cracks which form and cause the coated layer to break off. Studying the adhesion bond between plated film and metal substrate is beneficial in identifying the durability of coated layers. For example, it becomes possible to rate the quality of coatings based on the adhesive bond conditions—whether good adherence to the substrate has been achieved, or if it is in a poor condition such that rupture occurs at the interface of metallic layers. Dini (1993) divided adhesion into four groups: interfacial adhesion that is bonding with a clear interface, interdiffusion adhesion which is the diffusion of the deposited atoms in substrate, intermediate layer adhesion that is an intervention of a dissimilar layer like oxides between the plated layers, and mechanical interlocking where the roughness of metal substrate results in an atomic bond between the film and underlying substance.

Standard tests proposed for adhesion examination are more qualitative rather than quantitative and mostly depend on the operator's skill for their accuracy. The qualitative tests usually require low-cost equipment and are simpler to conduct. However, measurements

recorded from qualitative tests are not repeatable and vary with the thickness of the coated layer (Dini, 1993). In contrast, there are a few examinations such as conical head tensile, ring shear, flyer plate, ultrasonic, and peel tests that can be performed both in the laboratory and outside in order to quantitatively estimate the quality of a plated layer. However, these tests are more difficult to perform and usually require expensive equipment. Additionally, the results obtained on the same sample differ from test to test because surface damage on a plated film is more influenced by fracture failures rather than adhesion mechanism, and it is extremely difficult to predict the failure modes during operation (Dini, 1993).

8.1.2 Abrasive Wear

When analyzing the adhesion mechanism of a coated film, it is common to estimate the wear resistance of a plated layer. Wear is a uniform displacement or deformation of a solid surface over time, and its severity depends on the surface conditions, the loading rates, and the ambient conditions. Abrasive wear is the most probable damage that can occur on ASTM A 416 wires that are embedded in ducts. This can be described as the detachment of the coating layers due to plowing, cutting, or fragmentation that happens at the contact surface of a metal with another or a non-metallic substance.

Dini (1993) listed a few tests to evaluate wear performance of metallic coatings: including Taber Abrader, Falex Lubricant Tester, Reciprocating Scratch Test, Pin-on-Flat, Alfa Wear Test, and Accelerated Yarnline Wear Test. In all these wear examinations, the sample is always subjected to a cyclic abrasive load either under dry friction or with the use of lubricant. Then, the weight loss is recorded to determine the wear rate of the test sample after finishing the test operation.

8.1.3 Thickness Measurements

Estimating the wear rate of any coating film relies on the prediction of weight loss that itself is obtained from the thickness reduction of the coating film. However, sensitive equipment is needed to measure the section loss because the film is typically deposited in

micro scales. A powerful technique that can be used to measure the thickness of coating layers is Scanning Laser Doppler Interferometry (SLDI). It works based on recording the wavelength of the beam lights with relatively high precision and accuracy. A laser system illuminates two coherent beams of light as one is kept as a reference signal, and the other travels toward the subject. When the reflected light is received by the detector, a modulated voltage signal that is a wave constructed from both the reference light and the reflected wave from the specimen surface is sent to the oscilloscope. The interference pattern of the lights is then visualized and recorded for further analysis.

The mathematical representation of the modulated signal is given by the following equation;

$$\hat{I} = \hat{I}_r + \hat{I}_l + 2\sqrt{\hat{I}_r \hat{I}_l} \cos\left(2\pi \left(r_l - r_r\right)/\lambda\right), \tag{8.1}$$

where λ is the wavelength of the laser lights, 633 nm for the helium-neon laser. $\hat{I}_r$ and $\hat{I}_l$ are the intensity of reference and reflected lights, and r_r and r_l are optical paths that both reference and reflected lights travel to reach the sensor, respectively.

The output of the interferometer is a voltage variation that developed based on the bright and dark pattern of the modulated light, which itself is constructed from the Doppler frequency shift of the reflection wave. The voltages are directly proportional to the wave velocity of the returned signal. Hence, it becomes possible to apply a calibration factor to the output results to obtain the wave velocity of the recording waves. This factor is defined as the quotient of the range of measurements and the maximum voltage signal. Consequently, the wave displacement can be obtained from integrating the wave velocity over a time interval that is finally used to estimate the thickness loss of the coated film during the abrasive test. The reader is referred to (Hurlebaus et al., 2001; Kuttig et al., 2006) for the calculations carried out in the time-frequency domain and the autocorrelation of group velocity-frequency representations.

Figure 8.1: Sliding process that was completed with a 30×2 cm [12×3/4 in] galvanized cantilever beam.

8.2 Experimental Procedure

To examine the durability of coating layers in galvanized and plastic ducts, plated wires were cut to 63.5 millimeters [2.5 inches] segments. Then, samples were rinsed with deionized water and cleaned with acetone. Figure 8.1 shows the experimental setup for abrasive wear examination of electroplated wires. The coatings were subjected to two series of tests. At first, a 30×2 centimeters [12×3/4 inches] galvanized flat bar was clamped at the left side as shown in Figure 8.1. Then, the experiment was repeated once more, where the zinc plated sheet was replaced with a 30×2 centimeters [12×3/4 inches] PVC tube. In both cases, 200-gram weights were applied to the free end of the cantilever beams so that a sliding force generated between A 416 wires and the galvanized/plastic sheet. An impact driver with 155 N-m [1375 in-lbs] maximum torque that was capable of producing a speed up to 3000 RPM was secured at the location to hold the sample 127 millimeters [5 inches] from the fixed support. Then, a tachometer was used to measure the rotation speed of the driver at 100 rpm, and a zip tie was used to hold the trigger with a constant rate of rotation. The

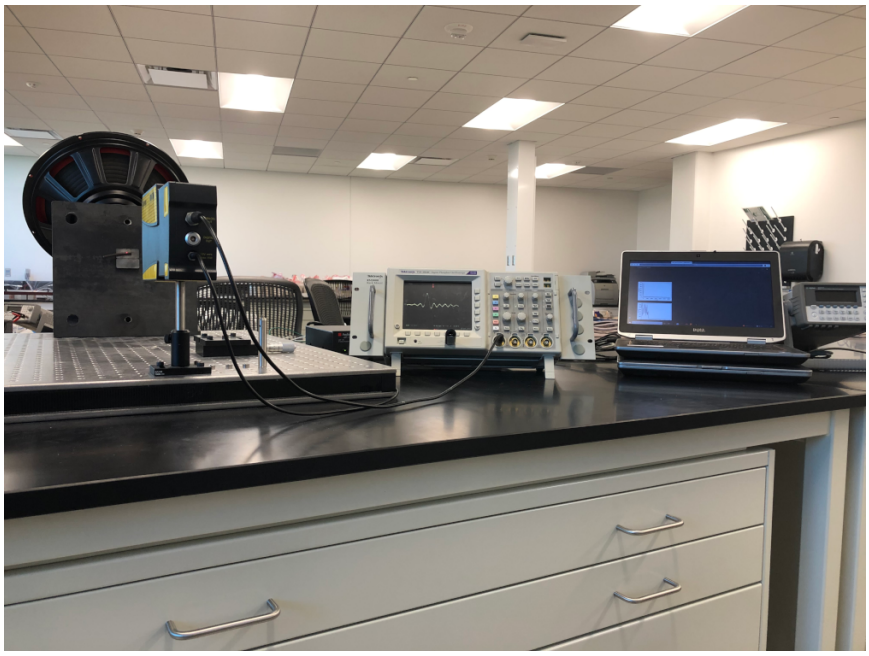

Figure 8.2: Oscilloscope visualization of the signals from the optical laser where a python script saved time domain signals in CSV files, simultaneously.

experimental procedure was followed for 5, 10, 15, 20, 25, 30 minutes of sliding duration. Then, samples were labeled for measurement with the laser.

After completion of the abrasive test, a PDV-100 interferometer system with a resolution 0.02 μm/s and an output center frequency 40 MHz was used to estimate the thickness loss of coated layers. The experimental setup consisted of a large magnet that supported a 30×30×1.3 centimeters [12×12×1/2 inches] base plate perpendicular to the optical table and held the target 54.6 centimeters [21.5 inches] from the sensor. A small magnet was also placed on the target so that the sample wires were in the correct position during the optical scanning. An oscilloscope visualized signals transferred from the interferometer.

As discussed in the previous section, the reflected beam from the wire's surface was detected with the optical laser. The device converted a bright and dark pattern produced as a result of Doppler frequency to a series of modulated output voltages. These signals were recorded in a CSV file that later was used as input for FFT analysis. Figure 8.2 demonstrates the optical laser scanning in progress.

8.3 Experimental Results

The laser interferometer used in this study had a maximum range of ±4 volts with a velocity measurement of 0.5 m/s, which results in a calibration factor equivalent to 0.125 m/s/V. This is the factor that was applied to the output signal to determine the wave velocity, $\dot{x}$, from voltages recorded by the oscilloscope, and subsequently, Eq. 8.2 was used to compute the reflected wave displacement, x,

$$\exists\ \tau \in (0, T) \ni x_\tau = \int_0^\tau \dot{x} \mathrm{d}t\ , \tag{8.2}$$

where T is the time period.

Figures 8.5 to 8.10 demonstrate the wave displacements in time domain constructed according to the procedure described above for all testing samples: as-received ASTM A 416 wires with zinc-phosphate layer available commercially in North America, and zinc-nickel and nickel-cobalt coated wires plated in the laboratory as discussed in Chapter 3. The abrasive test was completed in six periods of sliding duration where the samples abraded for 5, 10 ,15, 20, 25, and 30 minutes before scanning with the interferometer. Note that the results of the abrasive test reported here include both series of examinations completed with galvanized sheet and PVC tube.

Wave displacements in the frequency domain are also shown in Figure 8.5 to Figure 8.10. After constructing wave displacements over time from the laser interferometer recordings, a FFT analysis was performed to determine the amplitude of the output signals that later was used in the calculation of the wear rate of samples. The initial results of signals in the frequency domain were not quite satisfactory. To correct this, it was required to pad time domain signals with zeros to increase the frequency resolution of signals prior to the performance of FFT operation.

The maximum amplitude of the wave displacement in frequency domain decreased to half of the initial value after 5 minutes of sliding duration for the as-received sample abraded with

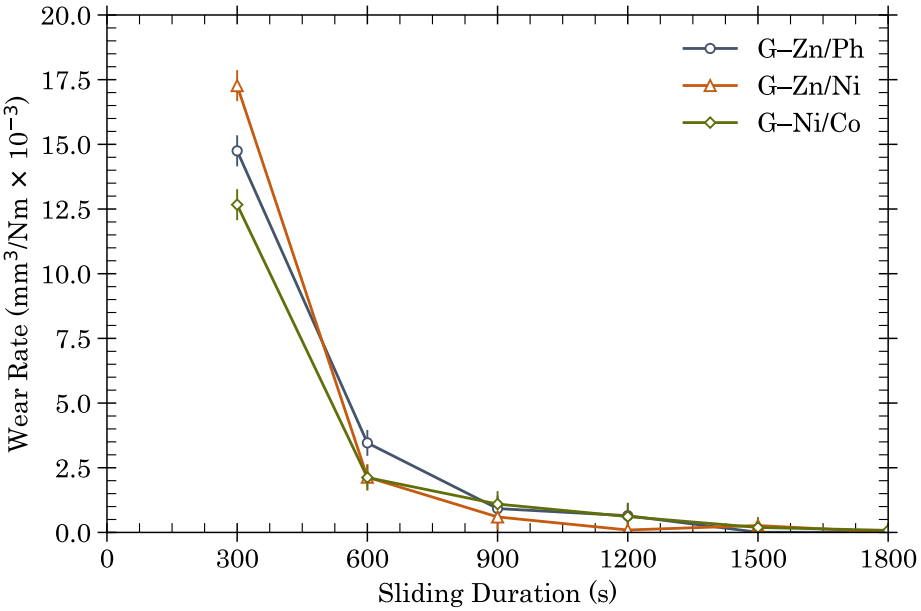

Figure 8.3: Wear rate of coatings subjected to abrasion – galvanized bar.

galvanized sheet as shown in Figure 8.5. Similarly, the amplitude was reduced by another half after 10 minutes, and a low voltage signal was recorded after 20 minutes of the test operation. It was observed that the coated zinc-phosphate layer was completely removed after 25 minutes, which was the case more or less for the other two coatings. Nickel-cobalt layer was completely abraded after 30 minutes (Figure 8.6), while zinc-nickel coated layer wore away after 20 minutes of testing (Figure 8.7). The amplitude of the signal recorded for the zinc-nickel layer dropped almost one-third after 5 minutes of sliding duration, which shows a higher rate of coating degradation in comparison to others.

When the abrasive test was repeated another time with PVC tube, damage on coatings was minor compared to the damage done during the test with a galvanized sheet. This was shown in Figure 8.8 to Figure 8.10 where the amplitude of wave displacements did not significantly decrease indicating a proper wear resistance. For the as-received wire, the amplitude was reduced to the half after 20 minutes of testing, and then coating degradation occurred at a slow rate. The amplitude signal recorded for the nickel-cobalt samples decreased a little after 5 minutes of sliding duration. The abrasion occurred with a fairly constant and negligible rate for the rest of the experiment. The sample coated with zinc-nickel exhibited

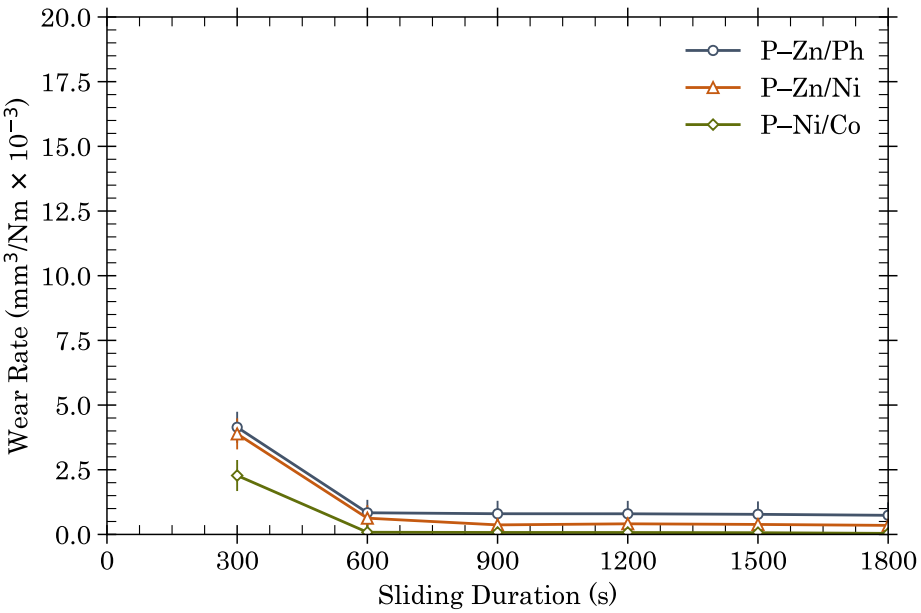

Figure 8.4: Wear rate of coatings subjected to abrasion - plastic sheet.

almost the same rate of degradation.

Archard (1953) suggested a theoretical terminology to compute the wear rate of rubbing surfaces that is still used to study the wear resistance of materials. In general, the wear rate of a coating film is the volume loss during abrasion (deformation wear) over the applied load and sliding distance, Eq. 8.3.

$$k = \frac{h}{\sigma S} \ . \tag{8.3}$$

The wear rate coefficient, k, is in $\mathrm{mm}^3/\mathrm{Nm}$. h is the wear displacement or the material thickness loss during the test operation, and σ is the applied stress at contact surfaces. S is sliding distance obtained by integrating slide rate over sliding duration. Figure 8.3 and Figure 8.4 demonstrate wear rate of the proposed coatings evaluated in the abrasive test with galvanized bar and plastic tube, respectively. The thickness loss used in Eq. 8.3 was obtained from the subtraction of two consecutive amplitude displacements.

The wear rate was higher for all the specimens at the beginning of the operation (Figure 8.3). This was perhaps because of the strong adhesion force at the interface of two solids,

yet a constant reduction in wear rates was observed as time proceeded. The wear rate of zinc-nickel coated samples was higher than other coatings, at least at the initial phase of the test, where sliding duration was 5 minutes. The rate dropped significantly after 20 minutes of abrasion, and then it continued at a steady rate. In fact, the coating was completely removed by 20 minutes of sliding as shown in Figure 8.3. The wear rates computed for 20 minutes and the higher duration are actually from steel substrate rather than the coating. Nickel-cobalt samples exhibited stronger wear resistance at the initial phase of the abrasive test. The wear rate of the coating was similar to the rate of as-received wire after 15 minutes of the test operation. The rate became small for both zinc-phosphate and nickel-cobalt coated layers by the end of the abrasive test, indicating a complete loss of the films.

In general, the wear resistance of all the coated samples was higher when the test was repeated with a plastic tube instead of galvanized bar. This was anticipated since sliding friction between coatings and plastic surface was substantially lower than metallic surface. However, it was observed that the wear rate of all samples was higher at the initial phase of the abrasive test regardless of the contact surface. Nickel-cobalt layer experienced lower wear rate compared to two other coatings, while the as-received sample abraded with a slightly higher rate in comparison to the zinc-nickel one. The wear rate for all the samples abraded with a plastic tube became steady after finishing 10 minutes of the test operation. This was not the case for specimens tested with a galvanized sheet where the coatings wore away approximately after 20 to 25 minutes of abrasion.

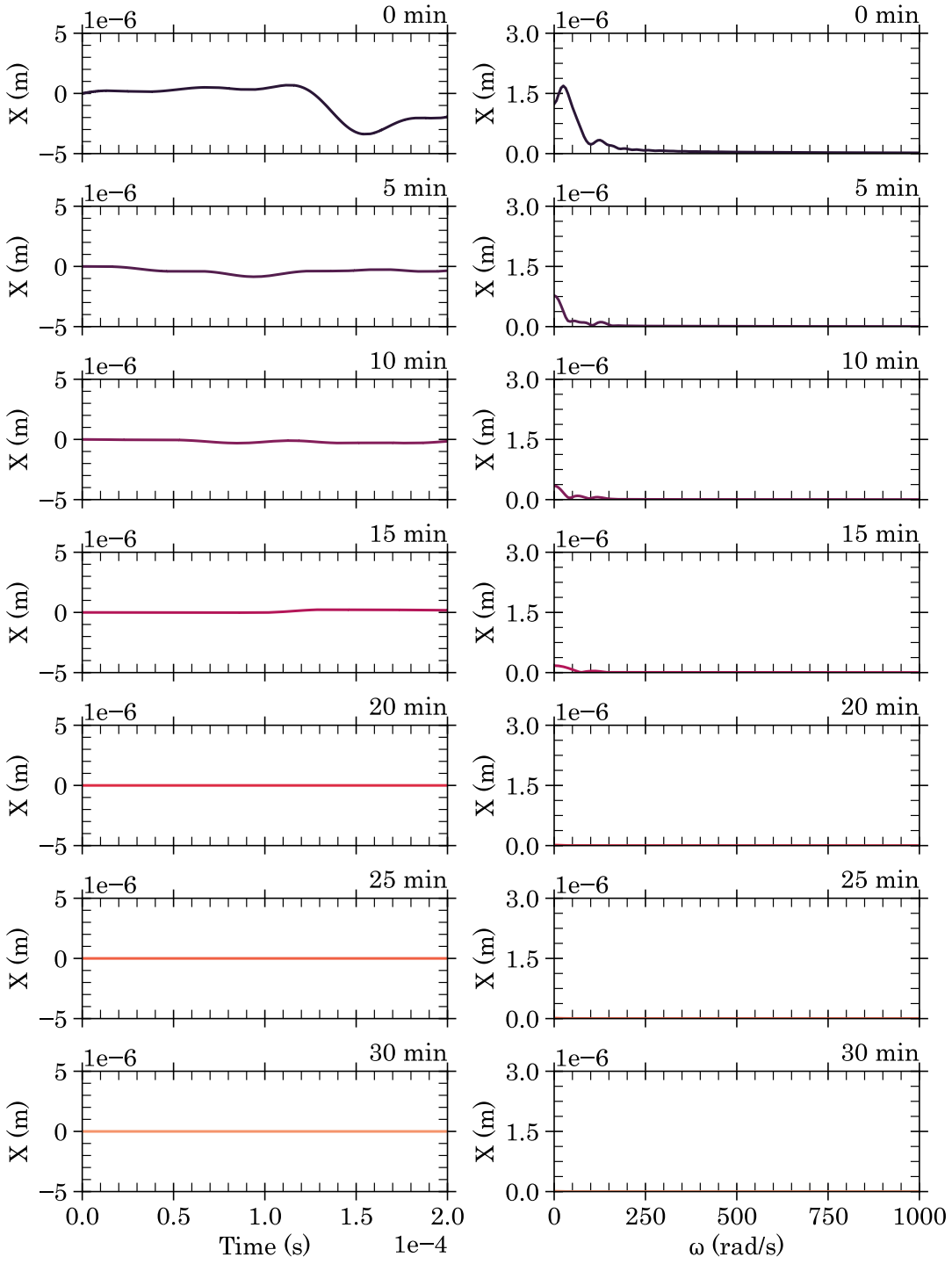

Figure 8.5: Wave displacements in time and frequency domains during the abrasive test with galvanized sheet for as-received wire.

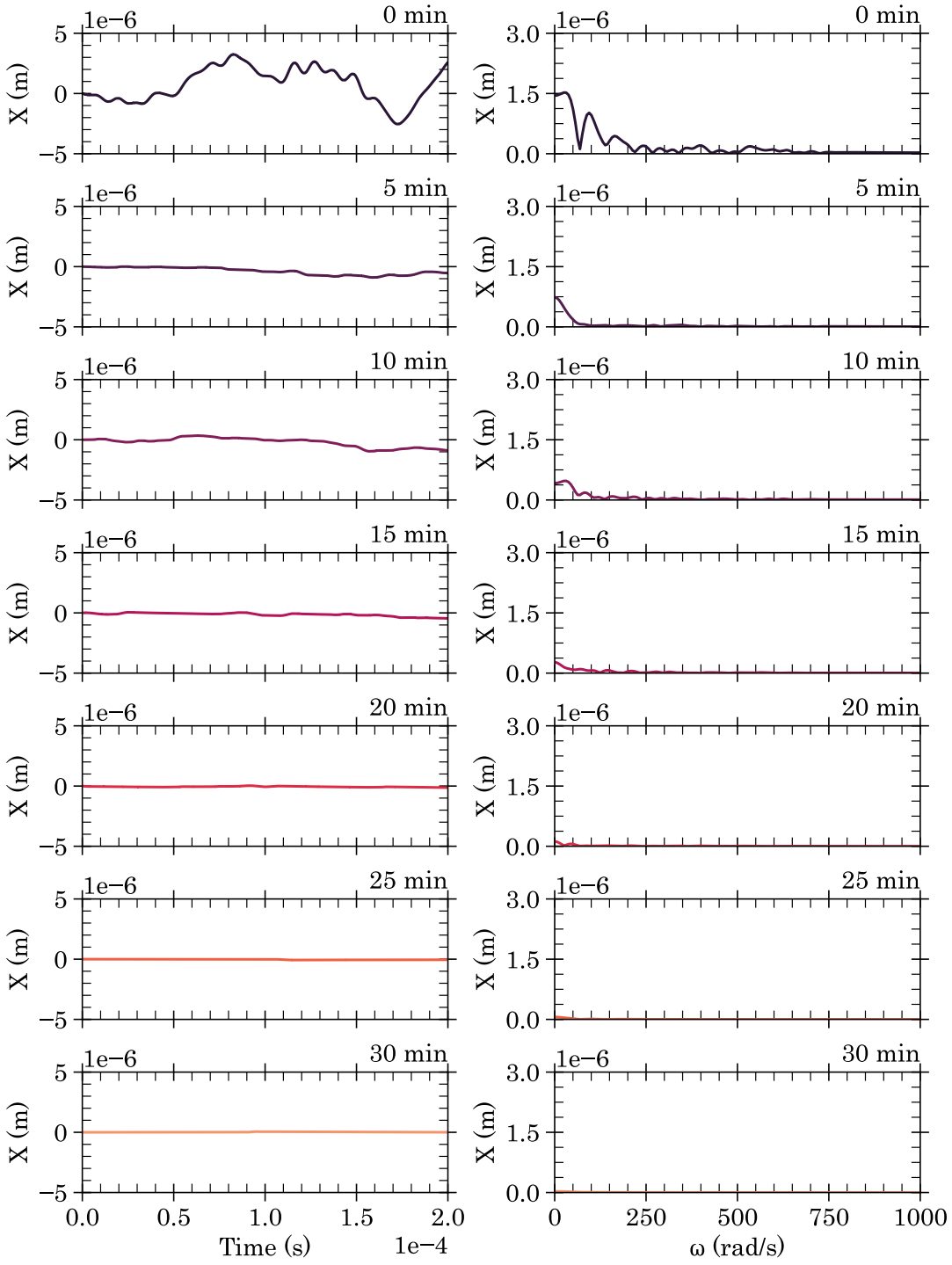

Figure 8.6: Wave displacements in time and frequency domains during the abrasive test with galvanized sheet for nickel-cobalt coated wire.

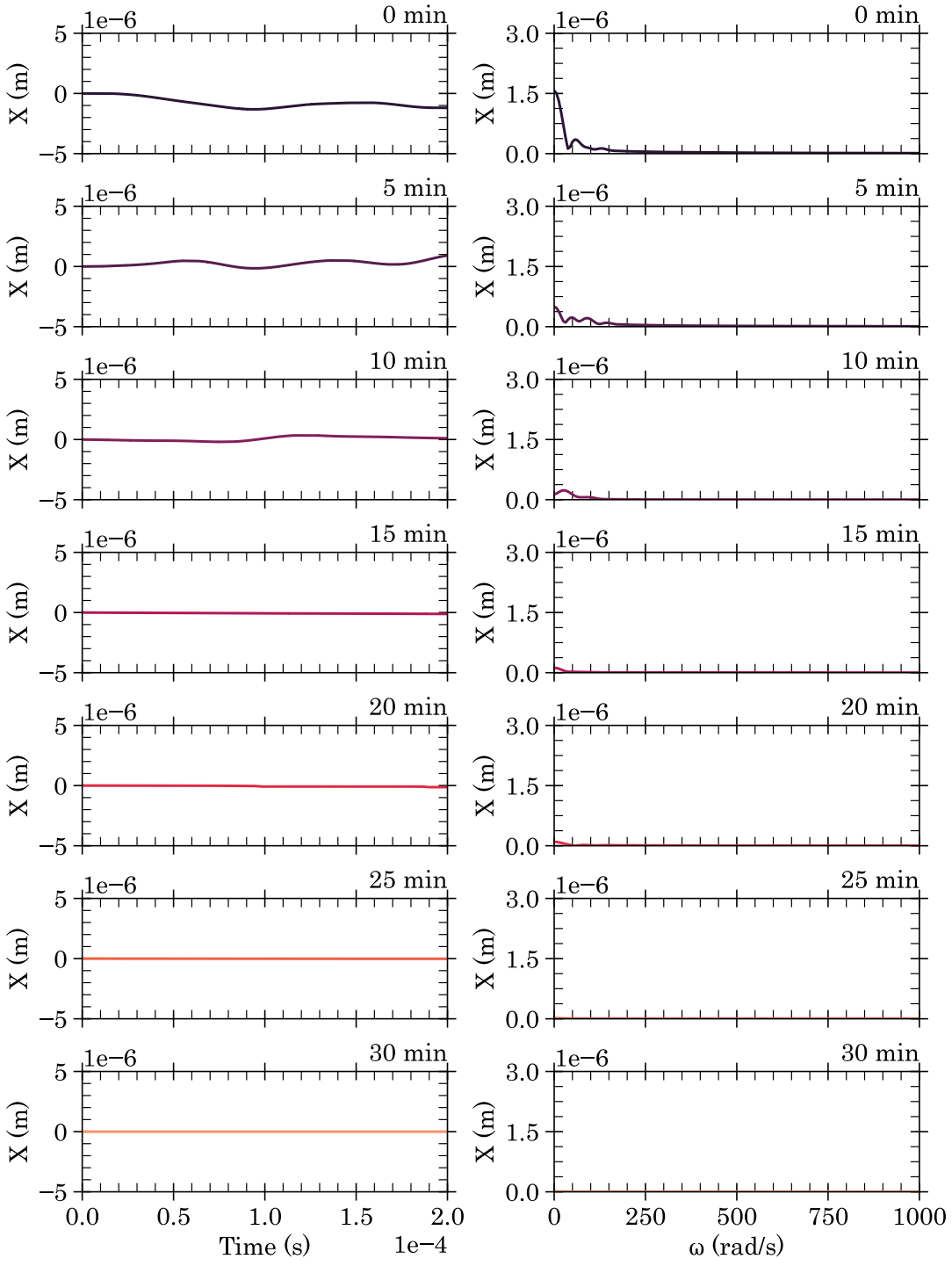

Figure 8.7: Wave displacements in time and frequency domains during the abrasive test with galvanized sheet for zinc-nickel coated wire.

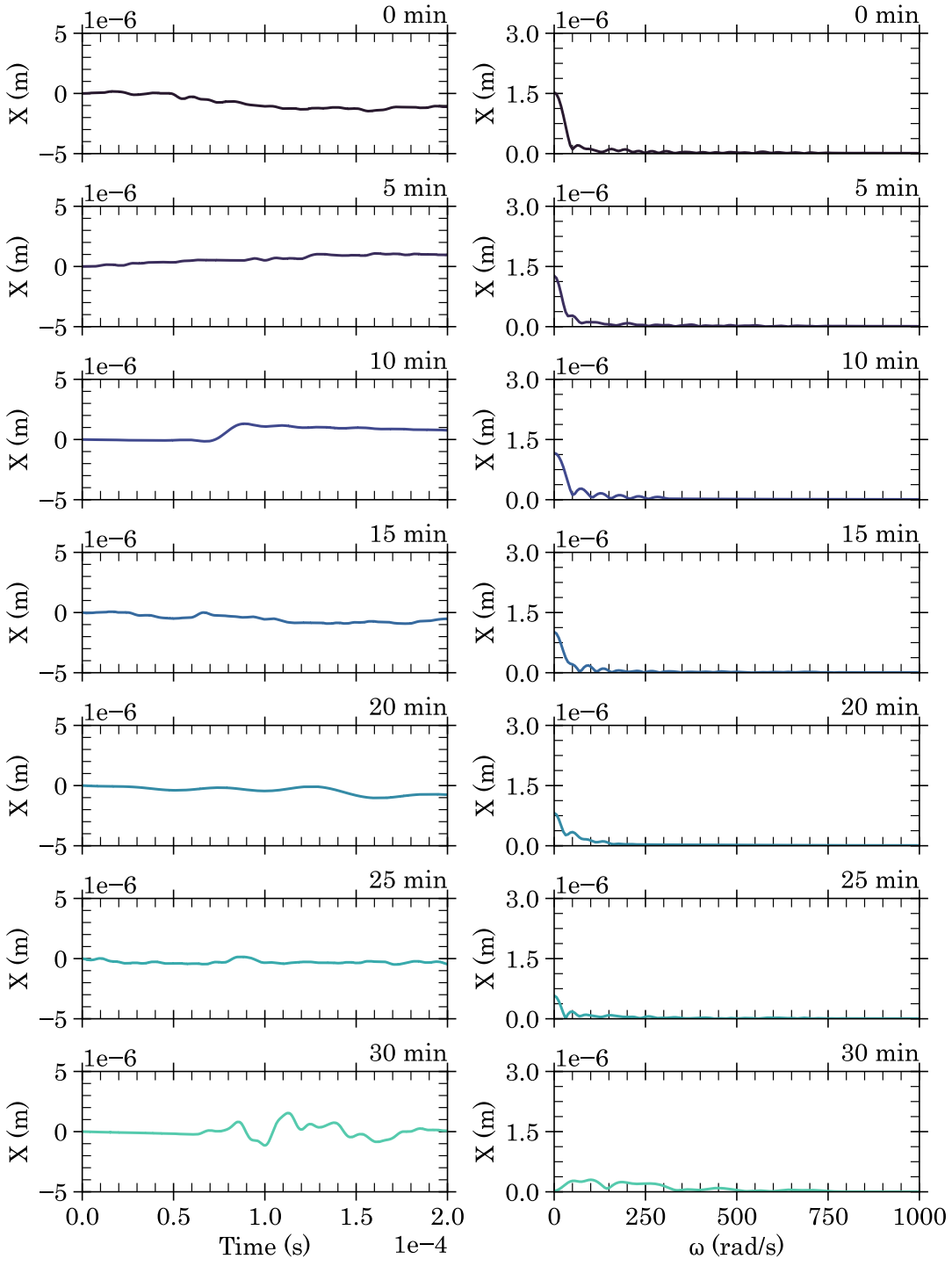

Figure 8.8: Wave displacements in time and frequency domains during the abrasive test with plastic sheet for as-received wire.

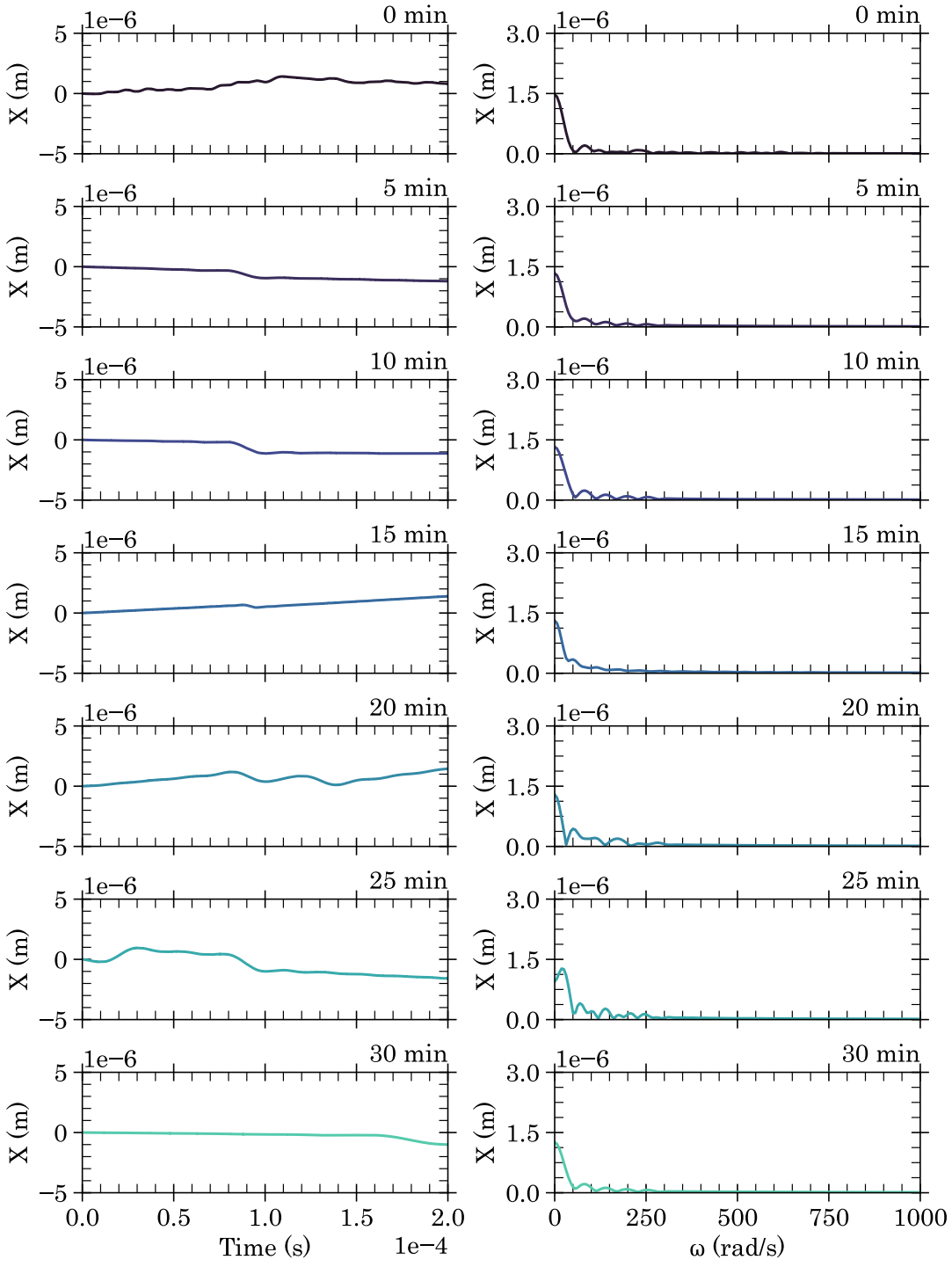

Figure 8.9: Wave displacements in time and frequency domains during the abrasive test with plastic sheet for nickel-cobalt coated wire.

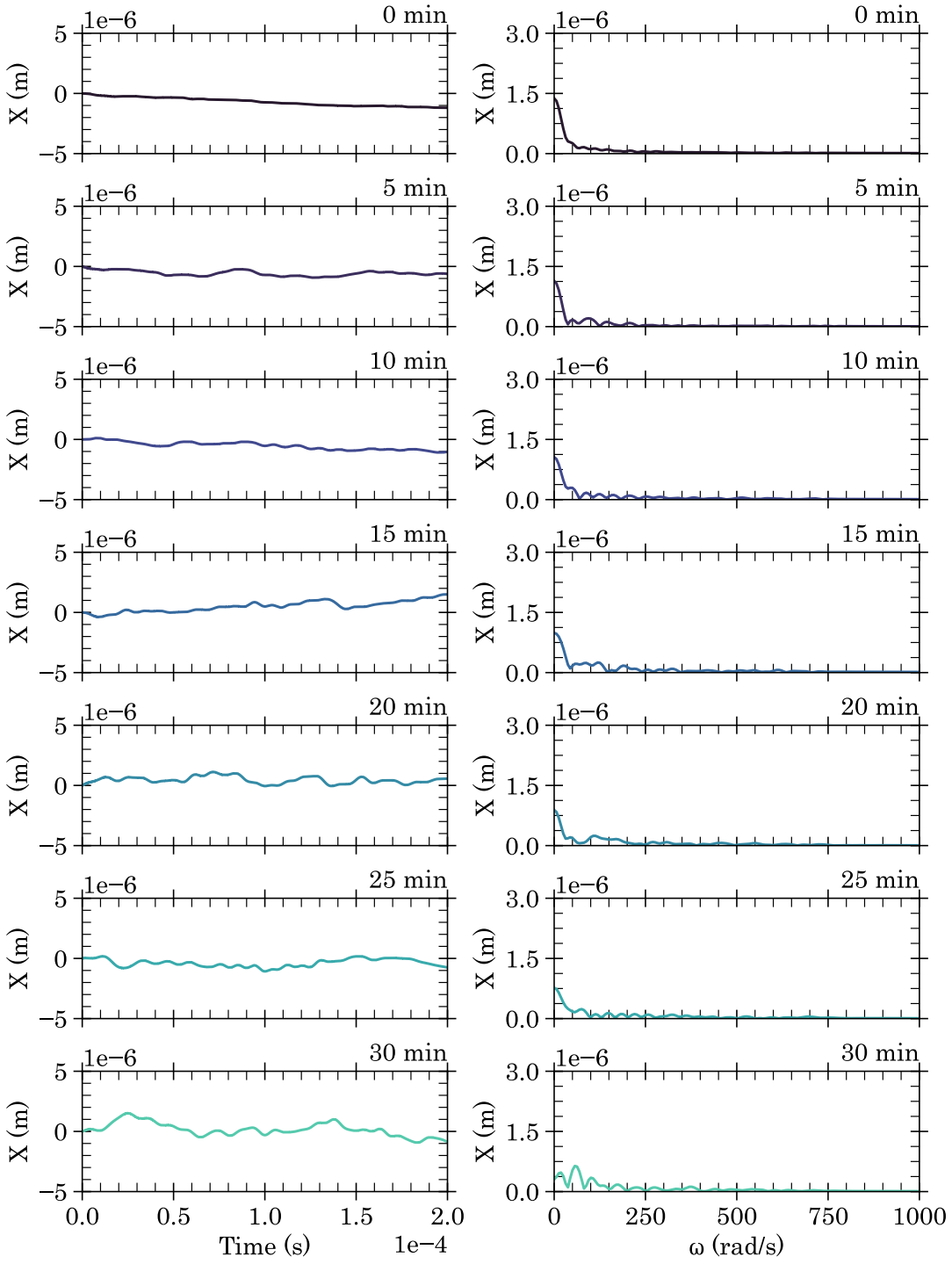

Figure 8.10: Wave displacements in time and frequency domains during the abrasive test with plastic sheet for zinc-nickel coated wire.

8.4 Further Discussion and Closing Remarks

A discussion on the durability of the metallic coatings plated on ASTM A 416 steel wires is taken in this chapter. This is more concern for post-tensioned systems since steel wires are pulled through galvanized or plastic ducts. However, it may also be a question for steel wires used in pretensioned and cable-stayed systems, particularly at the anchorage areas. Abrasive damage was observed and reported during the embrittlement test in Chapter 7 where zinc-nickel layers partially worn away as a consequence of detaching the wire from the corrosion cell. Similar damage was not seen on the nickel-cobalt and the zinc-phosphate coatings, yet a mild abrasion was noticed at the tails of the wires where the wedges were removed from the specimens.

A series of tests was conducted to assess the ability of steel wires to withstand abrasive wear. In the end, it was concluded that the wear rate of the coatings was generally lower when a plastic sheet was employed in the test, while the wear resistance of the coatings dropped as the test was carried out on metallic sheet. In addition, the wear rate of all the coatings was found significantly greater at the first 5 minutes of abrasion indicating that sliding distance impacts the wear rate of the coated films.

9. SUMMARY, CONCLUSIONS AND RECOMMENDATIONS

The application of impressed current to protect high-strength steel strands in prestressed structures has not received the concrete specialists' attention mainly because of the cost of anode systems and problems related to the brittle failure of steel components. Although the cost might be overlooked when the safety of a long span bridge or a power plant is a matter of public concern, degradation of steel strands should not be ignored since it can cause the collapse of the whole system. Although there are a few examples in Georgia and Florida that bridge owners successfully utilized impressed current to save onshore facilities from corrosion attacks and extend the service life of the system, it was also reported that the cathodically protected locations suffered from loss of flexural capacity. This research study is an attempt to find a solution that reduces the risks associated with hydrogen embrittlement in prestressed concrete systems and ensures the utilization of safe cathodic protection in civil structures.

A common form of damage resulting in degradation of steel in concrete structures is pitting corrosion. This is a localized attack that mostly arises from chloride ions stored in the surrounding pores, but other causes like carbonation and bacteria growth that lower the pH of the environment should not be ruled out. Pitting corrosion is destructive, and it enhances brittle failure of high-strength steel wires. Hence, the durability of steel components directly depends on systems that prevent the initiation of pits on wires.

Corrosion is a natural process and happens spontaneously, yet it can be controlled or delayed. This can be achieved by improving concrete properties, frequent inspections, and maintenance and rehabilitation treatments. However, several cases were reported in the past where corrosion attacks caused the failure of load bearing members despite efforts to combat it. Additionally, it is not practical to prevent the diffusion of chloride laden water in concrete bulk in marine structures. Therefore, cathodic protection can be a permanent solution to reduce the risks of corrosion attacks in concrete as long as it does not lead to

hydrogen embrittlement. The principle followed to cathodically protect steel wires from corrosion is that a driving voltage from a power source brings the potential to a level that the concentration of metal ions is low, thus there are insufficient ions to participate in redox reactions. Meanwhile, hydrogen can be evolved at extreme negative potential. The atomic hydrogen readily diffuses in steel and occupies spaces at the junction between ferrite and cementite causing brittle cracks in the prestressing strands.

ASTM A 416 steel wires are currently coated with a zinc-phosphate layer that is applied prior to cold working for surface treatment purposes. Studying the results obtained from the potentiodynamic test shows that the coating improved corrosion properties of the steel wires. The corrosion rate of high-strength steel was found to be relatively low in concrete unless the pH of the environment decreases; if so, the rate increases substantially as the environment becomes more aggressive. Alternatively, analyzing the kinetic properties of two metallic coatings proposed in this work revealed that nickel-cobalt alloy exhibited a slightly lower rate of corrosion compared to the one found for the current coating system. The corrosion rate of zinc-nickel alloy was significantly high in concrete but performed similarly to other coatings in a corrosive environment. Results of potentiodynamic testing agreed with the results obtained from the impedance analysis in Chapter 5 where zinc-phosphate and nickel-cobalt alloy improved the time constant of the charge transfer process and corrosion resistance of steel wires.

Cathodic protection reduces corrosion rate of high-strength steel wires regardless of the severity of the environment. From the results in Chapter 6, it was found that a current density in a range of 0.1 to 0.2 $\mu A/cm^2$ was sufficient to protect wires in simulated pore solution mixed with 3% salt-laden water, which exceeds the allowable chloride limits in concrete. Another conclusion derived from the galvanostatic test was that a larger driving voltage is required at higher concentrations of chloride ions.

Both nickel-cobalt and zinc-nickel coatings performed well in a hydrogen embrittlement test without ever failing, while the zinc-phosphate layer that is currently coated on high-strength

steel wires failed. It was concluded that nickel-cobalt alloy could be a proper substitution to the current coating system since the corrosion properties of the alloy are similar to those of the zinc-phosphate layer, while additionally acting as a hydrogen barrier. However, some valid concerns about the cost of the nickel-cobalt coating on steel wires may be raised which make the use of the alloy in the manufacturing process difficult. An alternative solution is perhaps applying multilayers of nickel prior to the current coating system which can reduce the risk of brittle failure of steel wires since hydrogen atoms are trapped in nickel crystal structures and cannot diffuse into substrate.

The corrosion resistance of zinc-nickel alloy in concrete is low, so it is not recommended for the use in prestressed systems. Zinc-nickel also acts as a hydrogen barrier and its utilization has been approved in the oil and gas industry where the pipelines are exposed to aggressive environments. This behavior was also observed from the experiments conducted in this study where the corrosion resistance of zinc-nickel alloy was higher in aggressive environments. In addition, the corrosion rate of zinc-nickel wires was recorded slightly lower than what was found for as-received specimens in the corrosive solution recommended by DIBt.

For any coating system, a problem that is always a matter of concern is the durability of the coated film to abrasive wear. It was found that the coatings used in this work exhibited more or less similar wear resistance, yet nickel-cobalt alloy showed slightly higher resistance. The results from the abrasive test indicate that galvanized ducts like those used in prestressed systems can cause an elevated rate of wear. In fact, it is plausible that coated films completely wear away when the strands are pulled through the metallic ducts. Therefore, the use of plastic ducts is recommended in prestressed systems; otherwise, lubricants ought to be applied prior to passing steel strands through the metallic ducts in order to reduce friction at the interface of metals. In addition, abrasion of the coated film may arise as a result of slip at the wedge. Hence, the design impressed current has to be adjusted for anchorage areas so that neither localized attacks nor brittle cracks occur.

REFERENCES

AASHTO, LRFD. (2012). *Bridge design specifications.* American Association of State Highway and Transportation Official.

ACI cmte. 222. (2014). *Report on corrosion of prestressing steels.* American Concrete Institute.

ACI Committee and International Organization for Standardization. (2019). Building code requirements for structural concrete ACI 318-19 and commentary. American Concrete Institute.

Alonso, M., Procter, R., Andrade, C., & de Santa María, M. S. (1993). Susceptibility to stress corrosion cracking of a prestressing steel in $NaHCO_3$ solutions. *Corrosion science*, *34*(6), 961–973.

Ameteksi. (n.d.). 1287A Electrochemical Interface user guide [Computer software manual].

Archard, J. (1953). Contact and rubbing of flat surfaces. *Journal of applied physics*, *24*(8), 981–988.

Bard, A. J., & Faulkner, L. R. (1983). Electrochemical methods fundamentals and applications. *Surface Technology*, *20*(1), 91–92.

Bažant, Z. (1972). Thermodynamics of interacting continua with surfaces and creep analysis of concrete structures. *Nuclear engineering and design*, *20*(2), 477–505.

Bažant, Z. P. (1975). Theory of creep and shrinkage in concrete structures: A precis of recent developments. *Mechanics today*, *2*, 1–93.

Bažant, Z. P., Hauggaard, A. B., Baweja, S., & Ulm, F.-J. (1997). Microprestress-solidification theory for concrete creep. I: Aging and drying effects. *Journal of Engineering Mechanics*, *123*(11), 1188–1194.

Bazzucchi, F., Restuccia, L., & Ferro, G. A. (2018). Considerations over the Italian road bridge infrastructure safety after the polcevera viaduct collapse: past errors and future perspectives. *Frattura e Integrita Strutturale*(46).

Bertolini, L., Elsener, B., Pedeferri, P., & Polder, R. (2004). Corrosion of steel in concrete: prevention, diagnosis, repair. *Bedin: Wiley—VCH*.

Bhadeshia, H. K. D. H. (2016). Prevention of hydrogen embrittlement in steels. *ISIJ international*, *56*(1), 24–36.

Bird, C., & Strauss, F. (1967). Metallic coatings for steel—tests indicate cadmium is a satisfactory coating material. *Materials Protection*, *6*(7), 48–52.

Briere, V., Harries, K. A., Kasan, J., & Hager, C. (2013). Dilation behavior of seven-wire prestressing strand—the hoyer effect. *Construction and Building Materials*, *40*, 650–658.

Broomfield, J. P. (2003). *Corrosion of steel in concrete: understanding, investigation and repair*. CRC Press.

Cannon, E., Lewinger, C., Abi, C., & Hamilton III, H. (2006). *St. George Island Bridge pile testing* (Tech. Rep.). Tallahassee, FL, United States: Florida Department of Transportation.

Castrodale, R. W., & White, C. D. (2004). *NCHRP Report 517, condition assessment of bridge post-tensioning and stay cable systems using NDE methods*. Transportation Research Board.

Chaix, O., Hartt, W., Kessler, R., & Powers, R. (1995). Localized cathodic protection of simulated prestressed concrete pilings in seawater. *Corrosion*, *51*(5), 386–398.

Chang, J. (2002). A study of the bond degradation of rebar due to cathodic protection current. *Cement and Concrete Research*, *32*(4), 657–663.

Chilamkuri, K., & Kone, V. (2020). Monitoring of varadhi road bridge using accelerometer sensor. *Materials Today: Proceedings*, *33*, 367–371.

Christodoulou, C., Glass, G., Webb, J., Austin, S., & Goodier, C. (2010). Assessing the long term benefits of impressed current cathodic protection. *Corrosion Science*, *52*(8), 2671–2679.

Claisse, P. A. (2014). *Transport properties of concrete: Measurements and applications*.

Elsevier.

Clark, G. M. (2013). Post-tensioned structures—improved standards. *Proceedings of the Institution of Civil Engineers-Forensic Engineering*, *166*(4), 171–179.

Corven, J., & Moreton, A. (2013). *Post-tensioning tendon installation and grouting manual* (Tech. Rep.). United States: Federal Highway Administration.

Das, P., Samantaray, S., & Rout, G. (1997). Studies on cadmium toxicity in plants: a review. *Environmental pollution*, *98*(1), 29–36.

Díaz, B., Freire, L., Nóvoa, X., & Pérez, M. (2009). Electrochemical behaviour of high strength steel wires in the presence of chlorides. *Electrochimica Acta*, *54*(22), 5190–5198.

Dini, J. W. (1993). *Electrodeposition*. Noyes Publications.

Dolin, P., & Ershler, B. (1940). Kinetics of processes on the platinum electrode. *Acta Physicochim. URSS*.

Donaldson, B. (2005). *Newcastle broken bridge.* `https://2010.igem.org/File:Newcastle_brokenbridge.jpg`. (Accessed: 2005-12-28)

Durairajan, A., White, R. E., & Popov, B. N. (2000). Studies on the hydrogen permeation through corrosion resistant zinc–nickel–cadmium coatings. In *Hydrogen at surface and interfaces: Proceedings of the international symposium* (Vol. 2000, p. 72).

Ebeling, R. M., White, B. C., Evans, J. A., Haskins, R. W., & Miller, E. L. (2016). *Corrosion induced loss of capacity of post tensioned seven wire strand cable used in multistrand anchor systems installed at corps projects* (Tech. Rep.). ARMY ENGINEER WATERWAYS EXPERIMENT STATION VICKSBURG MS VICKSBURG United States.

Elices, M., Caballero, L., Valiente, A., Ruiz, J., & Martin, A. (2008). Hydrogen embrittlement of steels for prestressing concrete: The FIP and DIBt tests. *Corrosion*, *64*(2), 164–174.

Enos, D., Williams Jr, A., Clemena, G., & Scully, J. (1998). Impressed-current cathodic protection of steel-reinforced concrete pilings: protection criteria and the threshold for hydrogen embrittlement. *Corrosion*, *54*(5), 389–402.

Enos, D., Williams Jr, A., & Scully, J. (1997). Long-term effects of cathodic protection on prestressed concrete structures: Hydrogen embrittlement of prestressing steel. *Corrosion*, *53*(11), 891–908.

Ganesan, P., Kumaraguru, S. P., & Popov, B. N. (2007). Development of compositionally modulated multilayer Zn–Ni deposits as replacement for cadmium. *Surface and Coatings Technology*, *201*(18), 7896–7904.

Golodnitsky, D., Rosenberg, Y., & Ulus, A. (2002). The role of anion additives in the electrodeposition of nickel–cobalt alloys from sulfamate electrolyte. *Electrochimica Acta*, *47*(17), 2707–2714.

Graham, A. K. (1971). *Electroplating engineering handbook*.

Griess, J. (1978). *Corrosion of steel tendons in concrete pressure vessels: review of recent literature and experimental investigations* (Tech. Rep.). Oak Ridge, TN, United States: Oak Ridge National Lab.

Hagarova, M., Jakubéczyová, D., & Cervová, J. (2015). Microstructure and properties of electroplated Ni–Co alloy coatings. *Int. J. Electrochem. Sci*, *10*, 9968–9974.

Hillier, E., & Robinson, M. (2004). Hydrogen embrittlement of high strength steel electroplated with zinc–cobalt alloys. *Corrosion science*, *46*(3), 715–727.

Hope, B. B., & Ip, A. K. (1993). Problems associated with cathodic protection of prestressed concrete structures. *Corrosion science*, *35*(5-8), 1641–1647.

Hurlebaus, S., Hueste, M. B. D., Karthik, M. M., & Terzioglu, T. (2016). *NCHRP Report 14-28, condition assessment of bridge post-tensioning and stay cable systems using NDE methods*. Transportation Research Board.

Hurlebaus, S., Niethammer, M., Jacobs, L. J., & Valle, C. (2001). Automated methodology to locate notches with lamb waves. *Acoustics Research Letters Online*, *2*(4), 97–102.

Ihekwaba, N., Hope, B., & Hansson, C. (1996). Pull-out and bond degradation of steel rebars in ECE concrete. *Cement and concrete research*, *26*(2), 267–282.

Janney, J. R. (1954). Nature of bond in pre-tensioned prestressed concrete. In *Journal*

proceedings (Vol. 50, pp. 717–736).

Johnson, W. H. (1875). II. on some remarkable changes produced in iron and steel by the action of hydrogen and acids. *Proceedings of the Royal Society of London*, *23*(156-163), 168–179.

Jovanović, D., Janković, P., Radovanović, M., & Đurić, S. (2018). The replacement of cadmium coating on parts of the weapon with tungsten-disulphide coating. *Advanced Technologies*, *7*(1), 64–68.

Kane, R., & Berkowitz, B. (1980). Effect of heat treatment and impurities on the hydrogen embrittlement of a nickel cobalt base alloy. *Corrosion*, *36*(1), 29–36.

Korzeniewski, C., & Conway, B. E. (1997). Proceedings of the symposium on the electrochemical double layer..

Kuttig, H., Niethammer, M., Hurlebaus, S., & Jacobs, L. J. (2006). Model-based analysis of dispersion curves using chirplets. *The Journal of the Acoustical Society of America*, *119*(4), 2122–2130.

Laco, J. (2018). Primary bond mechanism behavior of posttensioned 7-wire strand during load exposition. *Journal of Bridge Engineering*, *23*(5), 04018024-1–04018024-9.

Landolt, D., & Mischler, S. (2011). *Tribocorrosion of passive metals and coatings*. Elsevier.

Lim, S., Lee, H.-S., & Kawashima, S. (2018). Pore structure refinement of cement paste incorporating nanosilica: Study with dual beam scanning electron microscopy/focused ion beam (SEM/FIB). *Materials Characterization*, *145*, 323–328.

Little, B., & Staehle, R. (2001). Fungal influenced corrosion in post-tension structures. *Interface-Electrochemical Society*, *10*(4), 44–50.

Matzdorf, C., Lei, C., & Stanley, M. (2017). *Stress corrosion-cracking and corrosion fatigue impact of IZ-C17+ Zinc Nickel on 4340 steel* (Tech. Rep.). Patuxent River, MD, United States: NAWCAD.

Mindess, S., Young, F., & Darwin, D. (2003). *Concrete 2nd Edition*. Upper Saddle River, NJ: Pearson Education, Inc.

Mohamed, K., Abu-Hejleh, N. M., & Balice, J. (2018). Investigation, design, and repair of a major bridge foundation failure: I-43 Leo Frigo Memorial Bridge. In *Transportation research board 97th annual meeting.*

Mohammed, T. U., Hamada, H., & Yamaji, T. (2004). Performance of seawater-mixed concrete in the tidal environment. *Cement and concrete research*, *34*(4), 593–601.

Mondal, K. (2014). *Environmental degradation of materials.* National Programme on Technology Enhanced Learning (NPTEL).

Moore, D. G., Klodt, D. T., & Hensen, R. D. (1970). *NCHRP report - protection of steel in prestressed concrete bridges.* Transportation Research Board.

Moser, R., Holland, R. B., Kahn, L., Singh, P., & Kurtis, K. (2011). *Durability of precast prestressed concrete piles in marine environment: Reinforcement corrosion and mitigation—part 1, No. FHWA-GA-12-1026* (Tech. Rep.). Atlanta, GA, United States: Georgia Department of Transportation. Office of Research.

Myung, N. V., Park, D. Y., Yoo, B. Y., & Sumodjo, P. T. (2003). Development of electroplated magnetic materials for MEMS. *Journal of Magnetism and Magnetic Materials*, *265*(2), 189–198.

Naito, C., Sause, R., Hodgson, I., Pessiki, S., & Macioce, T. (2010). Forensic examination of a noncomposite adjacent precast prestressed concrete box beam bridge. *Journal of Bridge Engineering*, *15*(4), 408–418.

Naus, D. (1979). *Evaluation of the effectiveness of selected corrosion inhibitors for protection of prestressing steels in PCPVs* (Tech. Rep.). Oak Ridge, TN, United States: Oak Ridge National Lab.

Nawy, E. G. (1996). *Prestressed concrete. A fundamental approach* (No. Second Edition).

Novokshchenov, V. (1994). Brittle fractures of prestressed bridge steel exposed to chloride-bearing environments caused by corrosion-generated hydrogen. *Corrosion*, *50*(6), 477–485.

Nürnberger, U. (1997). Einflüsse von Werkstoff und Verarbeitung auf die Spannungsrisskor-

rosion von Spannstählen. *Materials and Corrosion*, *48*(9), 602–612.

Oliveira, R., Gonçalves, J., Ueda, M., Oswald, S., & Baldissera, S. (2010). Improved corrosion resistance of tool steel H13 by means of cadmium ion implantation and deposition. *Surface and Coatings Technology*, *204*(18-19), 2981–2985.

Papé, T. M., & Melchers, R. E. (2008). Investigating the effects of corrosion on 45-year-old prestressed concrete bridge beams. In *Life-cycle civil engineering* (pp. 441–446).

Parajuli, B. (2016). *Study of hidden corrosion on prestressing strands* (Unpublished doctoral dissertation). University of Toledo.

Pedeferri, P. (1996). Cathodic protection and cathodic prevention. *Construction and building materials*, *10*(5), 391–402.

Pillai, R. G., Trejo, D., Gardoni, P., Hueste, M. B. D., & Reinschmidt, K. (2014). Time-variant flexural reliability of posttensioned, segmental concrete bridges exposed to corrosive environments. *Journal of Structural Engineering*, *140*(8), A4014018.

Popov, B. N. (2015). *Corrosion engineering: principles and solved problems*. Elsevier.

Presuel-Moreno, F., Sagues, A., & Kranc, S. (2005). Steel activation in concrete following interruption of long-term cathodic polarization. *Corrosion*, *61*(5), 428–436.

Proverbio, E., & Bonaccorsi, L. (2002). Failure of prestressing steel induced by crevice corrosion in prestressed concrete structures. In *Proeedings of 9th international conference on durability of materials and components (9DBCM), brisbane.*

Puls, E. M. (2013). *A framework for historic bridge preservation* (Unpublished master's thesis). Texas A&M University.

Randles, J., & Somerton, K. (1952). Kinetics of rapid electrode reactions. part 4.—metal ion exchange reaction at amalgam electrodes. *Transactions of the Faraday Society*, *48*, 951–955.

Rashmi, S., Elias, L., & Hegde, A. C. (2017). Multilayered Zn–Ni alloy coatings for better corrosion protection of mild steel. *Engineering science and technology, an international journal*, *20*(3), 1227–1232.

Rehm, G., Nürnberger, U., & Frey, R. (1981). Zur korrosion und spannungsrißkorrosion von spannstählen bei bauwerken mit nachträglichem verbund. *Bauingenieur*, *56*(7).

Reis, R. A. (2007). Corrosion evaluation and tensile results of selected post-tensioning strands at the SFOBB skyway seismic replacement project. *California Department of Transportation: Sacramento, CA, USA*.

Roberge, P. R. (2012). *Handbook of corrosion engineering*. McGraw-Hill Education.

Roberts, M. (1962). Effect of calcium chloride on the durability of pre-tensioned wire in prestressed concrete. *Magazine of Concrete Research*, *14*(42), 143–154.

Rogers, R., Wotherspoon, L., Scott, A., & Ingham, J. M. (2012). Residual strength assessment and destructive testing of decommissioned concrete bridge beams with corroded pretensioned reinforcement.

Rosas, O., Hernandez, J., Garcia, O., & Girault, C. (2018). Ni–Co electroplating as corrosion protection for carbon steel fasteners used in oil and gas. In *Corrosion 2018*.

Ryan, T. W., Mann, J. E., Chill, Z. M., & Ott, B. T. (2012). *Bridge inspector's reference manual: Volume 1 and volume 2* (Tech. Rep.). United States: Federal Highway Administration.

Shifler, D. A. (2005). Understanding material interactions in marine environments to promote extended structural life. *Corrosion Science*, *47*(10), 2335–2352.

Singh, S. K. (2000). *Corrosion studies on prestressing steel wires* (Unpublished doctoral dissertation). Imperial College London (University of London).

Sly, C. (2001). An initial look at the lowe's motor speedway pedestrian bridge collapse. *Practical Failure Analysis*, *1*(2), 7–9.

Song, Lu, B., Gao, M., & Elboujdaini, M. (2011). *Development of a commercial model to predict stress corrosion cracking growth rates in operating pipelines* (Tech. Rep.). Austin, TX, United States: Southwest Research Institute.

Song, Y., Han, Z., Chai, M., Yang, B., Liu, Y., Cheng, G., & Li, Y. (2018). Effect of cementite on the hydrogen diffusion/trap characteristics of 2.25 Cr-1Mo-0.25 V steel

with and without annealing. *Materials*, *11*(5), 788.

Souza, R., Pereira, L., Starling, L., Pereira, J., Simões, T., Gomes, J., & Bueno, A. (2017). Effect of microstructure on hydrogen diffusion in weld and API X52 pipeline steel base metals under cathodic protection. *International Journal of Corrosion*.

Srivastava, M., Selvi, V. E., Grips, V. W., & Rajam, K. (2006). Corrosion resistance and microstructure of electrodeposited nickel–cobalt alloy coatings. *Surface and Coatings Technology*, *201*(6), 3051–3060.

Tektronix. (n.d.). TDS3000, TDS3000B, and TDS3000C Series Digital Phosphor Oscilloscopes programmer manual [Computer software manual].

Tepfers, R. (2000). *Bond of reinforcement in concrete, state of the art report prepared by fib task group bond models, former CEB Task Group 5.2.* External organization.

Treadaway, K. (1971). Corrosion of prestressed steel wire in concrete. *British Corrosion Journal*, *6*(2), 66–72.

Trejo, D., Hueste, M. B. D., & Gardoni, P. (2009). *Effect of voids in grouted, post-tensioned concrete bridge construction: volume 1—electrochemical testing and reliability assessment* (Tech. Rep.). College Station, TX, United States: Texas Transportation Institute.

Vacek, V., Kolisko, J., Pokornỳ, P., & Kostelecká, M. (2020). Steel reinforcement corrosion-its impact on features of steel PSC strand. In *Key engineering materials* (Vol. 868, pp. 57–64).

Winkler, J., Georgakis, C. T., & Fischer, G. (2015). Fretting fatigue behavior of high-strength steel monostrands under bending load. *International Journal of Fatigue*, *70*, 13–23.

Woodward, R. (1989). Collapse of a segmental post-tensioned concrete bridge. *Transportation research record*(1211).

Wu, S. T., & Clifton, J. R. (1981). *Analysis and modeling of corrosion of steel in prestressed concrete*. US Department of Commerce, National Bureau of Standards.

Wykpis, K., Popczyk, M., & Budniok, A. (2011). Electrolytic deposition and corrosion

resistance of Zn–Ni coatings obtained from sulphate-chloride bath. *Bulletin of Materials Science*, *34*(4), 997.

Zeng, Z., Chan, M. K., Zhao, Z.-J., Kubal, J., Fan, D., & Greeley, J. (2015). Towards first principles-based prediction of highly accurate electrochemical pourbaix diagrams. *The Journal of Physical Chemistry C*, *119*(32), 18177–18187.

APPENDIX A

SUPPLEMENTARY DOCUMENTATION

A.1 Case Studies

Table A.1 represents all the cases of failure of prestressed systems due to corrosion and material degradation between 1965 and 2018. Over time, pretensioned and post-tensioned structures were developed to be more durable. For example, the water to cementitious materials ratio has been limited in concrete mixed design, and the use of less permeable concrete such as ultra-high-performance concrete has become more prevalent. However, it seems that the failure of the prestressed structures as a result of corrosion problems has been an existing issue for these systems over the last 60 years.

The structural failures listed in Table A.1 range from minor damage causing loss of operability for necessary rehabilitation to full-scale collapse during the service life of the structure. That said, the reader has to consider that not all the failures in the past are reported in the literature. For example, corrosion related problems that cause degradation of prestressed strands in a small parking garage, or a concrete slab in a residential building, are not usually documented. Moreover, corrosion related problems as the result of the chemical and nuclear waste are not listed in Table A.1, and the focus is on the failure of highway overpasses, foot-bridges, parking garages, and building slabs.

A point highlighted in Table A.1 is that corrosion problems in concrete were more significant in West Europe in the early 80s. However, this became more noticeable in the U.S. in the late 90s to early 2000s because the prestressed bridges were constructed later in North America compared to Europe. In recent years, tragic failures have been reported from South Europe. Therefore, It is speculated that the bridge owners did not pay enough attention to concrete repair and rehabilitation of the systems in that particular region.

Table A.1: Previous failures of non-building prestressed structures.

No.	Name	Date of Event	Location	Design	Application	Condition
1	Polcevera Viaduct (Bazzucchi et al., 2018)	2018	Genoa, Italy	Cable-Stayed Bridge	Highway Bridge	Collapsed
2	Majerhat Bridge (Chilamkuri & Kone, 2020)	2018	Kolkata, India	Prestressed Concrete	Highway Bridge	Collapsed
3	Fossano (Cuneo) Bypass (Bazzucchi et al., 2018)	2017	Fossano, Italy	Multiple-box Post-tensioned	Highway Bridge	Collapsed
4	Troja (Vacek et al., 2020)	2017	Prague, Check	Prestressed Concrete	Footbridge	Collapsed
5	Annone Overpass (Bazzucchi et al., 2018)	2016	Lecco, Italy	Precast Concrete	Highway Bridge	Collapsed
6	Parking Garage (Parajuli, 2016)	2016	University of Toledo, Canada	Prestressed Spandrel	Slab	Closed for Rehabilitation
7	Petrulla Viaduct (Bazzucchi et al., 2018)	2014	Sicily, Italy	Precast Concrete	Highway Bridge	Collapsed
8	Leo Frigo Memorial (Mohamed et al., 2018)	2013	Green Bay, Wisconsin	Post-tensioned Foundation	Highway Bridge	Closed for Rehabilitation

9	Turtle River Bridge (Moser et al., 2011)	2010	Brunswick, Georgia	Prestressed Member Piles	Highway Bridge	Replaced
10	Tiwai Point Bridge (Rogers et al., 2012)	2009	South Island of New Zealand	Prestressed Concrete	Highway Bridge	Replaced
11	John Day Lock and Dam (Ebeling et al., 2016)	2008	Columbia River, Oregon	Prestressed Member	Multi-strand Anchorage Systems	Rehabilitation
12	San Francisco Bay Bridge (Reis, 2007)	2006	Oakland, California	Concrete Segmental Structures	Highway Bridge	Closed for Rehabilitation
13	Varina-Enon Bridge (Hurlebaus et al., 2016)	2006	Richmond, Virginia	Post-tensioned	Highway Bridge	Closed for Rehabilitation
14	Lake View Drive Bridge (Naito et al., 2010)	2005	Bryson City, Pennsylvania	Post-tensioned Box Beams	Highway Bridge	Collapsed
15	St. George Island Bridge (Cannon et al., 2006)	2004	Franklin County, Florida	Precast Concrete Piles	Highway Bridge	Closed for Rehabilitation
16	Sorell Causeway Bridge (Papé & Melchers, 2008)	2002	Causeway, Tasmania	Prestressed, Precast Bridge	Highway Bridge	Closed for Rehabilitation
17	Sunshine Skyway Bridge (Hurlebaus et al., 2016)	2000	Tampa, Florida	Segmental Post-tensioned	Highway Bridge	Closed for Rehabilitation

18	Lowe's Motor Speedway (Sly, 2001)	2000	North Carolina	Pretensioned	Footbridge	Collapsed
19	Niles Channel Bridge (Hurlebaus et al., 2016)	1999	Florida Keys, Florida	External Post-tensioned Tendon	Highway Bridge	Closed for Rehabilitation
20	Mid-Bay Bridge (Hurlebaus et al., 2016)	1999	Destine, Florida	Segmental Post-tensioned	Highway Bridge	Closed for Rehabilitation
21	Mandovi River Bridge (Clark, 2013)	1998	Nagercoil, India	Segmental Prestressed Concrete	Highway Bridge	Collapsed
22	Melle Bridge (Proverbio & Bonaccorsi, 2002)	1992	Schelde, Belgium	Post-tensioned	Highway Bridge	Collapsed
23	Highway Bridges (ACI cmte. 222, 2014)	1989	Gulf of Mexico	Pretensioned and Post-tensioned Girders	Highway Bridge	Rehabilitation
24	Ynys-y-Gwas (Woodward, 1989)	1985	Wales, UK	Segmental Post-tensioned	Highway Bridge	Collapsed
25	Southern Roof of the Berlin Congress Hall (Rehm et al., 1981)	1980	Berlin, Germany	Prestressed Concrete Roof	Slab	Closed for Rehabilitation

26	Taf Fawr Bridge (Proverbio & Bonaccorsi, 2002)	1980	Wales, UK	Prestressed Concrete Bridge	Highway Bridge	Minor Damage
27	Angel Road Bridge (Proverbio & Bonaccorsi, 2002)	1980	London, UK	Prestressed Concrete Bridge	Railway	Minor Damage
28	Cleddau Bridge (Broomfield, 2003)	1972	Milford Haven, Wales, UK	Post-tensioned	Highway Bridge	Collapsed
29	Bickton Meadows (Pillai et al., 2014)	1965	Hampshire, UK	Post-tensioned	Precast segmental Footbridge	Collapsed

A.2 Transfer Bond in Prestressed Concrete

The transfer bond between cementitious material and prestressed strands is not uniformly distributed along tendon length. As an example, interaction between concrete and strands becomes weaker at segments closer to the beam-end. This is the area that is known as the anchorage zone or the development length and is usually divided in two extents: transfer length, which is the depth that prestress develops along the tendon, and embedment length over which prestress increases linearly throughout the concrete cross section (Figure A.1).

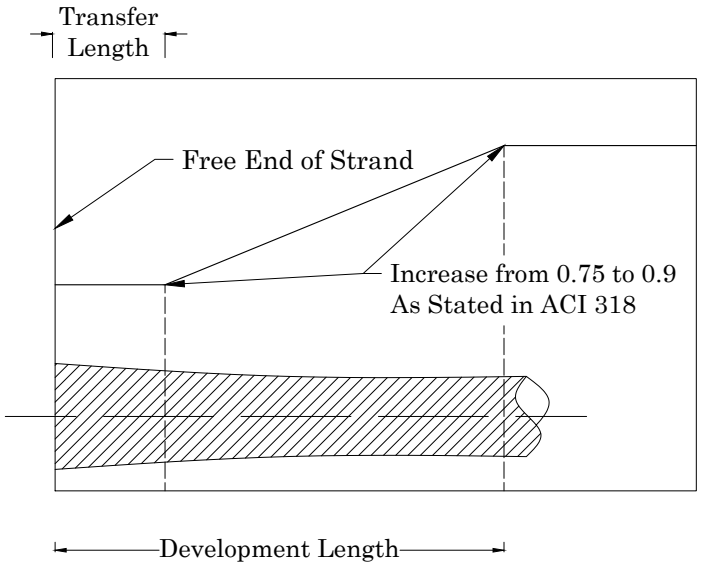

Figure A.1: Increase in strength reduction factor (ϕ) over development length, adapted from ACI 318 (2019) with permission.

Transfer bond plays an important role to transfer the tendon force to the concrete. Four mechanisms including adhesion, mechanical interlock, friction, and confinement occur in order to develop a transfer bond between concrete and tendons.

A.2.1 Adhesion:

A primary bond forms mainly due to chemical interactions between cementitious materials and steel. Note, the chemical bonds will disappear when slips occur between a metal surface and concrete, thus adhesion loss in prestressed structures happens upon the release of strands.

A.2.2 Mechanical Interlock:

Mechanical interlock refers to interaction between concrete and strands due to the helical shape of seven steel wires (Figure A.2).

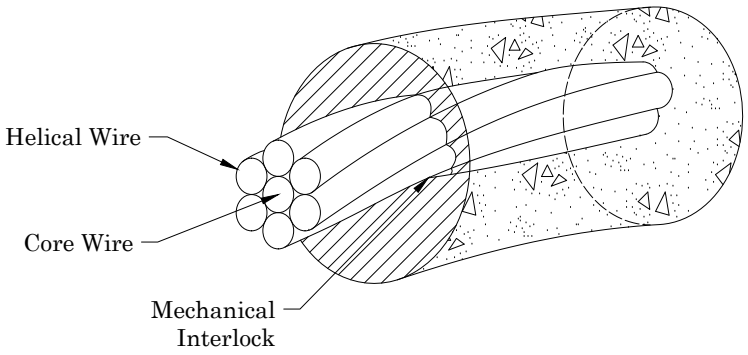

Figure A.2: Prestressing strand and mechanical interlock.

A.2.3 Friction:

This is a contact force between steel and concrete developed to resist the slip of strands. A bond due to friction in prestressed concrete depends on many aspects; e.g., eccentricity due to curve shape of wires in concrete, Poisson's ratio and modulus of elasticity of both concrete and strands, wear resistance of steel, concrete cover, section properties, quality of cement and cement hydration, and ambient temperature and pH.

A.2.4 Confinement (Hoyer Effect):

According Briere et al. (2013), Hoyer, who designed the pretensioned systems, recognized that tendons re-anchor themselves through the development length after strands are slowly released (Figure A.3). Hoyer called this phenomenon "stahlsaiten beton" or "steel string" which refers to confinement of strands in the surrounding concrete as a result of friction and mechanical wedge. When strands are stretched between abutments, the size of wires reduces mainly because of the Poisson's effect, but wires tend to return to their initial size as stress is relieved causing a radial compression in addition to prestress force that tightens tendons to the concrete.

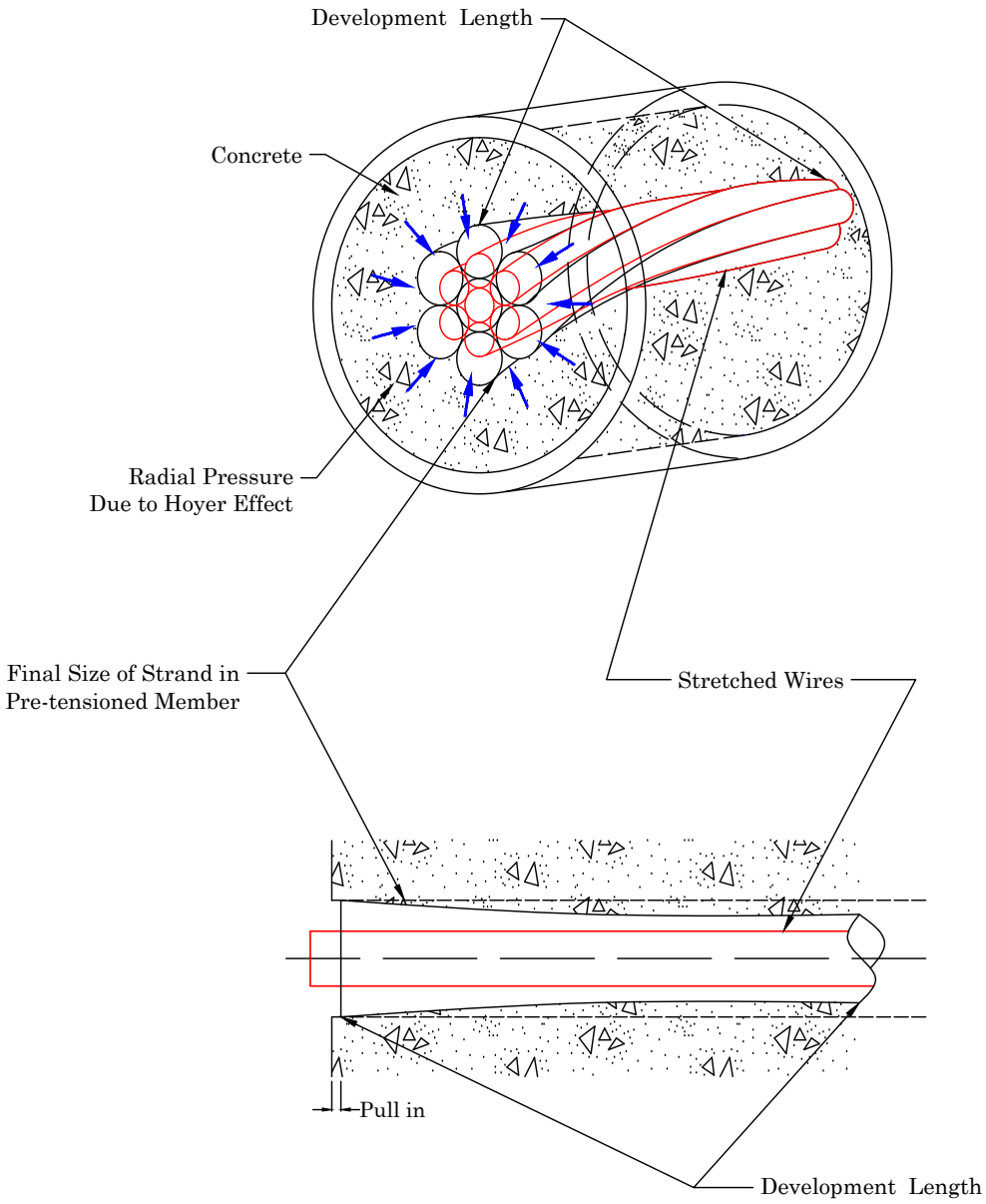

Figure A.3: Hoyer effect, modified from Briere et al. (2013).

A.3 Python Scripts

The Python script below automates the process of measuring and recording the cell potential and the electric current in the corrosion cell where a Solartron Analytical 1287A Potentiostat is used to control the system. The reader is referred to a complete list of SI1287A commands in the device's user's manual Chapter 4 / Section 6 (Ameteksi, n.d.).

```
import pyvisa as vp
import pandas as pd
import numpy as np
from sklearn.linear_model import LinearRegression
from matplotlib import pyplot as plt
from matplotlib.animation import FuncAnimation
import threading as th
import time
import datetime

# Connect Solartron Analytical 1287A Potentiostat to computer. This can be done
    by pyvisa library and a GPIB cable.

rm=vp.ResourceManager()
print(rm.list_resources())

inst=rm.open_resource("GPIB0::4::INSTR", write_termination="\n",
    read_termination="\n")

print(inst)

# Now that the connection is good, we need to initialize the Potentiostat. See
    the SI 1287A user manual Chapter 4/Section 6 for a complete list of commands.
```

```
inst.write('BK4')

# set cont. measurements
command='TR1';inst.write(command)
command='GP1';inst.write(command)

# set output parameters
# command='PX9';inst.write(command)
command='PX3';inst.write(command)

# set sweep RAMP VOLTAGE
command='DL1';inst.write(command) # initial delay
command='SM4';inst.write(command) # Segments
command='VA-1.1';inst.write(command) # Min Voltage
command='TA120';inst.write(command) # Time
command='VB1.1';inst.write(command) # Max Voltage
command='TB60';inst.write(command) # Time
command='VC1.1';inst.write(command) # Max Voltage
command='TC120';inst.write(command) # Time
command='VD0-1.1';inst.write(command) # Min Voltage
command='TD60';inst.write(command) # Time

# set sweep STEP
command='SA-1.0';inst.write(command) # Min Voltage
command='SB2';inst.write(command)
command='SC2';inst.write(command)
command='SD1.0';inst.write(command) # Max Voltage
command='TE10';inst.write(command)
```

```
command='VS.05';inst.write(command)

# set the device in Potentiostat/Galvanostat mode
command='PO0';inst.write(command) #Potentiostat
#command='PO1';inst.write(command) #Galvanostat

# set default values for voltage and current
command='PV-0.9';inst.write(command)
#command='PC0.000000001';inst.write(command)

# set the digital voltmeter on
command='RU1';inst.write(command);

# Add signal to default
command='PB9';inst.write(command); # bandwidth
command='FI1';inst.write(command); # Low Pass Filter On
command='VX1';inst.write(command); # Voltage amplifier
command='IX1';inst.write(command); # Current amplifier
command='DG0';inst.write(command); # AC signal

print(datetime.datetime.now().time())

print('v-t  v-I')
cycle=2
df=[]
func=[]
x,y,t=[],[],[]

key_interrupter=True
```

```
def keys():
    global key_interrupter
    input()
    key_interrupter=False

def loop():
    th.Thread(target=keys, args=(), name='keys', daemon=True).start()

    %matplotlib notebook
    fig=plt.figure()
    ax1=fig.add_subplot(121)
    ax2=fig.add_subplot(122)
    plt.ion()

    fig.show()
    fig.canvas.draw()
    fig.gca().relim()
    fig.gca().autoscale_view()

    ii=0
    while key_interrupter:
        df.append(inst.read('\n'))
        func.append(df[len(df)-1][:-1].split(','))

        x.append(float(func[len(df)-1][1]))
        y.append(float(func[len(df)-1][0]))
        s=float(func[len(df)-1][4])*3600+float(func[len(df)-1][5])*60
            +float(func[len(df)-1][6])+float(func[len(df)-1][7])*.01
        t.append(s)
```

```
        ax1.clear()
        ax2.clear()
        ax1.plot(t,y)
        ax2.plot(x,y)
        fig.canvas.draw()
        fig.gca().relim()
        fig.gca().autoscale_view()
        time.sleep(0)

for i in range(1,cycle):
    command='PW1';inst.write(command) # set the device on polarization ON.
        (assumes ON mode.)
    command='SW1';inst.write(command) # set the device on sweep ramp
#    command='SW2';inst.write(command) # set the device on sweep step
    loop()
    results=pd.DataFrame(list(zip(x, y)), columns=['i', 'V'])
    results.to_excel('final_results.xlsx', index=False)

print('DONE.')
print(datetime.datetime.now().time())
```

The Python script below reads the output measurements of TDS3000, TDS3000B, and TDS3000C Series oscilloscopes. The reader is referred to Tektronix Oscilloscopes user guide (Tektronix, n.d.) for a complete list of syntax and commands to communicate with the device. After recording the time-domain voltages, the code calculates the impedance of the system and converts the results to the frequency domain. Finally, the impedance spectroscopy data is produced and will be recorded in a CSV file.

```
import pyvisa as vp
import pandas as pd
import numpy as np
from sklearn.linear_model import LinearRegression
from scipy.fft import fft,ifft
from scipy import signal
import threading as th
from matplotlib import pyplot as plt
from matplotlib.animation import FuncAnimation
import struct
import time
import datetime



# Communicate with, or remotely control, TDS3000, TDS3000B, and TDS3000C Series
    oscilloscopes. This, indeed, can be done by pyvisa library and a GPIB cable.

rm=vp.ResourceManager()
print(rm.list_resources())

scope=rm.open_resource("GPIB0::1::INSTR", write_termination="\n",
    read_termination="\n")
```

```
print(scope)
print(scope.query('*IDN?'))

# See the Tektronix TDS3000, TDS3000B, and TDS3000C Series Digital Phosphor
    Oscilloscopes 071-0381-03 programmer manual for a complete list of syntax and
    commands.

X=[]; Y=[]; f=[]
Rs=10000 # Rs=10 kohms dummy load resistor

#decay/step
wi= 100000
wf= 5
decay =10

_p = np.log(wi/wf)*decay
f = np.logspace(np.log10(wf), np.log10(wi), int(_p))

print(freq)

x1,y1,x2,y2=[],[],[],[]
t1,t2,V1,V2=[],[],[],[]

key_interrupter=True
def keys():
    global key_interrupter
    input()
    key_interrupter=False
```

```
def loop():
    th.Thread(target=keys, args=(), name='keys', daemon=True).start()

    ii1=0; ii2=0
    while key_interrupter:
        scope.write('DATa:SOUrce CH1')
        scope.write('DATa:WIDth 1')
        scope.write('DATa:ENCdg RPB')
        scope.write('WFMPRe?')
        scope.write('CURVe?')
        data=scope.read_raw()

        Yzero=float(scope.query('WFMPre:YZEro?'))
        Ymul=float(scope.query('WFMPre:YMUlt?'))
        Yoff=float(scope.query('WFMPre:YOFf?'))
        Xinc=float(scope.query('WFMPre:XINcr?'))

        header_length=0+int(data[1])
        header=data[:header_length]
        wave=data[header_length:-1]
        op1=np.array(struct.unpack('%sB' % len(wave),wave))

        v1=(op1 -Yoff) *Ymul +Yzero

        Time1=np.arange(0, Xinc*len(v1), Xinc) +ii1

        scope.write('DATa:SOUrce CH2')
        scope.write('DATa:WIDth 1')
        scope.write('DATa:ENCdg RPB')
```

```
scope.write('WFMPRe?')

scope.write('CURVe?')

data=scope.read_raw()


Yzero=float(scope.query('WFMPre:YZEro?'))

Ymul=float(scope.query('WFMPre:YMUlt?'))

Yoff=float(scope.query('WFMPre:YOFf?'))

Xinc=float(scope.query('WFMPre:XINcr?'))


header_length=2+int(data[1])

header=data[:header_length]

wave=data[header_length:-1]

op2=np.array(struct.unpack('%sB' % len(wave),wave))


v2=(op2 -Yoff) *Ymul +Yzero


Time2=np.arange(0, Xinc*len(v2), Xinc) +ii2


x1=Time1.tolist()

y1=v1.tolist()

x2=Time2.tolist()

y2=v2.tolist()


t1.append(x1);t2.append(x2)

V1.append(y1);V2.append(y2)


ii1=Time1[len(Time1)-1]

ii2=Time2[len(Time2)-1]
```

```
loop()


Ch1=V1 ; Ch2=V2
Vs=np.array(Ch2) ; VL=np.array(Ch1)


V=Vs ; I=VL / Rs
vf=fft(V)


N=2*vf.shape[0]
T=1 / N / 2
Y1=2/N *np.abs(vf[0:N//2])


A1=[] ; phi1=[]


for n in range(0,len(Y1)):
    A1.append(max(Y1[n]))
    index=Y1[n].argmax()
    phi1.append(np.angle(vf[n][index]))


If=fft(I)
Y2=2/N *np.abs(If[0:N//2])


A2=[] ; phi2=[]


for n in range(0,len(Y2)):
    A2.append(max(Y2[n]))
    index=Y2[n].argmax()
    phi2.append(np.angle(If[n][index]))
```

```
Z=[]
for n in range(0,len(A1)):
    Z.append(A1[n]/A2[n] *np.exp((-1)**(.5)*(phi1[n]-phi2[n])))

Zre=[] ; Zim=[]
for i in Z:
    Zre.append(i.real)
    Zim.append(i.imag)

Zre=np.around(Zre, 15)
Zim=np.around(Zim, 15)

X.append(np.mean(Zre))
Y.append(np.mean(Zim))



Xf=[];[Xf.append(i-Rs) for i in X]
Yf=[];[Yf.append(i*-1) for i in Y]

Xf=[];[Xf.append(i-Rs) for i in X]
Yf=[];[Yf.append(i*-1) for i in Y]

f=np.array(f)

final_results=pd.DataFrame(list(zip(f,Xf,Yf)), columns=['freq. Hz','Zre','Zim'])
final_results.to_excel('Impedance.xlsx', index=False)
```